

# Lattice disorders of TiO<sub>2</sub> and their significance in the photocatalytic conversion of CO<sub>2</sub>

Karishma Piler<sup>a</sup>, Cristian Bahrim<sup>b</sup>, Sylvestre Twagirayezu<sup>c</sup>,  
and Tracy J. Benson<sup>a,d,\*</sup>

<sup>a</sup>Dan F. Smith Department of Chemical and Biomolecular Engineering, Lamar University, Beaumont, TX, United States

<sup>b</sup>Department of Physics, Lamar University, Beaumont, TX, United States

<sup>c</sup>Department of Chemistry and Biochemistry, Lamar University, TX, United States of America

<sup>d</sup>Center for Midstream Management and Science, Lamar University, Beaumont, TX, United States

\*Corresponding author: e-mail address: tracy.benson@lamar.edu

## Contents

1. Introduction	3
2. Background of TiO <sub>2</sub>	4
2.1 Crystallography of TiO <sub>2</sub>	5
2.2 Polymorphs of TiO <sub>2</sub>	6
2.3 Significance of crystal facets of TiO <sub>2</sub> in photocatalysis applications—CO <sub>2</sub> conversion	8
3. The role of lattice defects and their respective crystal facets in CO <sub>2</sub> photocatalysis	10
4. Defects in the TiO <sub>2</sub> crystalline structure	17
4.1 Point defects	17
4.2 Planar defects	20
5. Methods to synthesize lattice disorder engineered TiO <sub>2</sub>	21
5.1 Annealing in vacuum at high temperature	21
5.2 Titanium dioxide precursor with reducing agents at high temperatures	22
5.3 Ion or electron bombardment	23
5.4 UV irradiation	24
6. Origin of intrinsic lattice defects in anatase, rutile, and brookite phases	24
7. Recently developed methods for characterizing the lattice defects of TiO <sub>2</sub>	27
7.1 Experimental techniques	27
8. Theoretical techniques: Density functional theory (DFT)	33
8.1 Brief overview of DFT as applied to TiO <sub>2</sub>	33
8.2 DFT of TiO <sub>2</sub> without dopants	37
8.3 DFT for surface modifications to TiO <sub>2</sub>	42
8.4 Interactions (adsorption/reaction) with TiO <sub>2</sub> and organic and inorganic molecules	53
8.5 Summary of theoretical investigations	60

9. TiO <sub>2</sub> defect synthesis techniques for photocatalytic purposes	62
9.1 Synthesis methods for black TiO <sub>2</sub>	62
9.2 Controlling Ti <sup>3+</sup> sites	67
9.3 Synthesis of doped TiO <sub>2</sub> photocatalysts	70
9.4 Microwave, ionic liquid, and combined microwave/ionic liquid methodologies	82
9.5 TiO <sub>2</sub> (B): The fourth polymorph of TiO <sub>2</sub>	88
9.6 Hybrid photocatalysts constituting of TiO <sub>2</sub> and their respective defects	90
9.7 Summary of defect synthesis methods	93
10. CO <sub>2</sub> Photocatalytic conversions using TiO <sub>2</sub>	93
10.1 Conversion of CO <sub>2</sub> on unsupported TiO <sub>2</sub>	94
10.2 Conversion of CO <sub>2</sub> on supported TiO <sub>2</sub> catalysts	102
11. Oxygen vacancy recovery during photocatalytic reaction	114
12. Concluding remarks	115
13. Future challenges	117
Acknowledgments	118
References	118
About the authors	123

## Abstract

Developing economic strategies for the conversion of carbon dioxide, given its potential impact on global climate change, has become necessary for the long-term sustainability of the planet Earth. From traditional thermochemical routes, CO<sub>2</sub> conversion requires a substantial amount of costly energy, which in itself produces CO<sub>2</sub>. Utilizing solar energy, particularly radiation in the visible spectrum, can be the most efficient method for supplying the energy requirement. This review explores TiO<sub>2</sub>, and its various polymorphs, as a catalyst component in CO<sub>2</sub> photoconversion. Titania is an abundant resource that would make for a low-cost catalytic material. As shown in this work, crystal lattice defects in TiO<sub>2</sub> can be systematically tailored to yield a photocatalyst that provides optimum adsorption and activation of CO<sub>2</sub> on the TiO<sub>2</sub> surface and allows sufficient electron–hole separation times. These separation times are necessary for efficient surface site chemistries to occur. In addition to synthesis techniques, this review also describes the latest characterization tools used to investigate lattice defects, including oxygen vacancies, as well as corresponding Density Functional Theory (DFT) studies. Two key features of this work will be (1) defining the relationship between the lattice defects and (2) the Fermi Energies that are paramount for activating the catalyst in the visible region. The catalyst is thereby optimized by controlling these defects. Furthermore, TiO<sub>2</sub>-based hybrid photocatalysts and their corresponding lattice defects in photoconversion of CO<sub>2</sub> to useful products are discussed.



## 1. Introduction

The rise in atmospheric carbon dioxide (CO<sub>2</sub>) has caused concerns toward its effects on global climate change. Climate scientists suggest that a 50% reduction in CO<sub>2</sub> emissions is necessary to limit the rise in the average global temperature and to reduce mankind's carbon footprint. Therefore, proper utilization of CO<sub>2</sub>, specifically power plant and industry generated large point sources, becomes immensely essential. Utilization of CO<sub>2</sub>, in other words, converting CO<sub>2</sub> to useful and carbon neutral products can be performed through various techniques, including thermochemical, chemical, biological, electrochemical, and photocatalytic conversions. In recent years, there has been increased interest in the photocatalytic conversion of CO<sub>2</sub> primarily into carbon monoxide, formaldehyde, formic acid, acetic acid, methane, light hydrocarbons, and methanol (1,2).

Titanium dioxide (TiO<sub>2</sub>) nanoparticles can provide the fundamental building blocks of photocatalysis, a significant area of solar energy utilization (3). TiO<sub>2</sub> is an abundantly available n-type semiconductor with high chemical stability, simple composition, and is environmentally nontoxic (4). Furthermore, TiO<sub>2</sub> manufacturing processes are easily scalable (5). Recent studies have revealed that surface-disorder-engineered TiO<sub>2</sub> (or defect rich TiO<sub>2</sub>) has excellent photocatalytic activity due to good charge carrier separation and enhanced quantum efficiency (6). Chen *et al.* mentioned that the visible and infrared absorption and carrier trappings can be optimized with the introduction of a large number of surface or lattice disorders within TiO<sub>2</sub> (7).

These lattice disorders give origin to point (or lattice) defects on the TiO<sub>2</sub> surfaces, which play a vital role in photocatalytic applications, including the photoreduction of CO<sub>2</sub> by acting as active sites for chemisorption and molecular dissociation of CO<sub>2</sub> (8). In other words, the adsorption and activation of CO<sub>2</sub> in the presence of point defects have been shown to be enhanced. Liu *et al.* inferred that the point defects such as Ti<sup>3+</sup> and oxygen vacancies helped in allowing the efficient charge or hole transfer between CO<sub>2</sub>/H<sub>2</sub>O and reduced TiO<sub>2</sub> (TiO<sub>2-x</sub>) under photo-illumination (9). These defects lead to more favorable formation of bridged CO<sub>2</sub><sup>-</sup>, HCO<sub>3</sub><sup>-</sup>, and HCOOH. Proper utilization of point defects aids in product selectivity from CO<sub>2</sub> photoreduction (9). Realizing the significance of point or lattice defects in the enhancement of a photocatalytic reaction, further

development and examination of  $\text{TiO}_2$  at the atomic level could lead to more improvements in the field of  $\text{CO}_2$  photoconversion to useful chemicals.

This review covers the most recent research on lattice defects of  $\text{TiO}_2$  including their origin, synthesis, recovery, and characterization techniques as well as their role in the photocatalytic reduction of  $\text{CO}_2$ .  $\text{CO}_2$  conversion was chosen as the benchmark reaction due to its high degree of thermodynamic stability and a societal need for its removal from the atmosphere. Of particular interest, for economic reasons, is the  $\text{CO}_2$  reduction using  $\text{H}_2\text{O}$  as the reducing agent. As will be shown, adsorption and surface reactions of both  $\text{CO}_2$  and  $\text{H}_2\text{O}$  are competing reactions. There are surface interactions that can lead to limited electron flows and rate limiting redox reactions. Finally, this work attempts to provide fresh perspectives in reference to the development of novel photocatalysts for  $\text{CO}_2$  conversion.



## 2. Background of $\text{TiO}_2$

$\text{TiO}_2$  is intrinsically an n-type semiconductor belonging to the group of transition metal oxides (10,11).  $\text{TiO}_2$  has a general chemical composition of 59.9 wt% titania and 40.1 wt% oxygen and a molecular weight of 79.9 g/mol.  $\text{TiO}_2$  exhibits polymorphism, the capability of a solid material to exist in more than one crystalline structure. There are four naturally occurring polymorphs of  $\text{TiO}_2$ —anatase, rutile, brookite, and  $\text{TiO}_2$  (B) monoclinic. Anatase, rutile, and brookite (Fig. 1) are the most studied polymorphs (12–14). Two other polymorphs that can be synthesized from rutile are  $\text{TiO}_2$  (II) and  $\text{TiO}_2$  (H) (hollandite) (15–18). Catalytically speaking, catalysts with high surface to volume ratios (i.e., spherical) are of greatest interest for their number of active sites per unit mass. However, for  $\text{TiO}_2$ ,



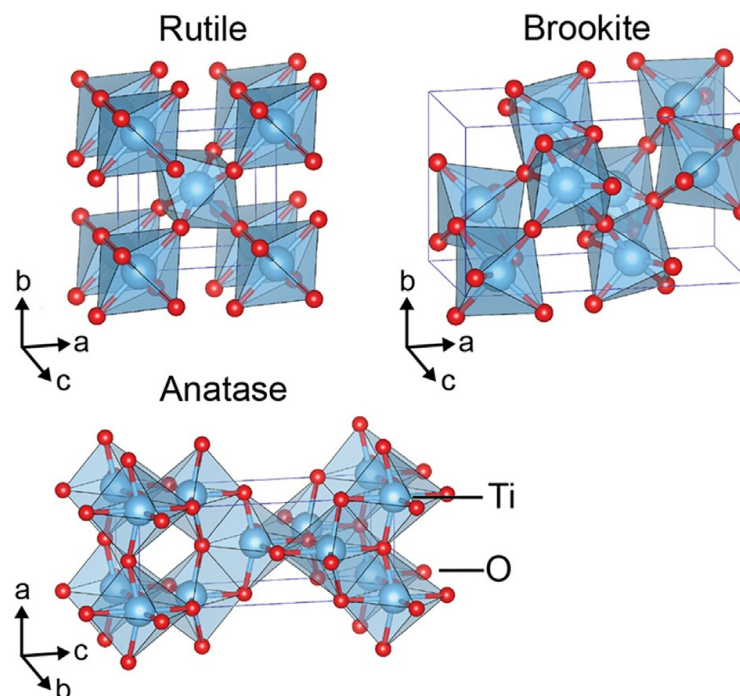
**Fig. 1** Crystal forms of  $\text{TiO}_2$  as found in nature (A) Anatase, (B) Brookite, and (C) Rutile.



spherical geometry leads to electron–hole recombinations that hinder efficient electron transfers necessary for reactions. Therefore, a balance must be sought.

## 2.1 Crystallography of $\text{TiO}_2$

Metal oxides such as titanium dioxide have their crystal structure built with  $\text{MO}_n$  polyhedral building blocks. For example,  $\text{TiO}_2$  is made up of repeating fundamental  $\text{TiO}_6$  polyhedral unit cells (or more specifically  $\text{TiO}_6$  octahedral units). Each of the polymorphs of  $\text{TiO}_2$  have differing arrangements of these octahedral units, leading to different crystal structures. The rutile unit cell is made up of two Ti atoms and four oxygen atoms, whereas the anatase unit cell is made up of four Ti atoms and eight oxygen atoms, forming the  $\text{TiO}_6$  octahedrons. The ball and stick representation of the bulk unit cells of rutile, anatase, and brookite are shown in Fig. 2 with oxygen atoms colored red and titania in blue. The bulk crystal structure of anatase has a greater distorted  $\text{TiO}_6$  octahedra than rutile. The arrangement of  $\text{TiO}_6$  octahedral units can be controlled by tuning the pH of the reaction solution, introducing interfering ions, or changing reaction parameters in the synthesis of  $\text{TiO}_2$ . The local environment of  $\text{TiO}_6$  octahedra can be distorted by adding interfering or blocking ions such as  $\text{Fe}^{3+}$ ,  $\text{Sc}^{3+}$ , and  $\text{Sm}^{3+}$ . Such interfering ions introduce local chemical defects and change the chemical



**Fig. 2** Crystal structures of  $\text{TiO}_2$  (A) Rutile, (B) Anatase, and (C) Brookite (14).

potential energy of the octahedral units altering the arrangement of the octahedral units of  $\text{TiO}_2$ . Precise control over the arrangement of these polyhedral units will make it easy to tailor the photovoltaic, catalytic, and electrochemical properties of the metal oxides as needed (19).

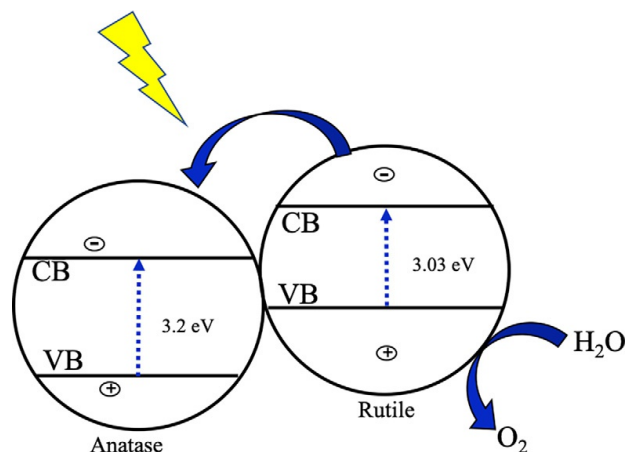
## 2.2 Polymorphs of $\text{TiO}_2$

### 2.2.1 Anatase and rutile

Anatase, rutile, and mixtures of anatase and rutile are the most commonly studied phases of  $\text{TiO}_2$ . The crystallographic details and band gap energies are given in Table 1. Anatase is most stable at low particle sizes ( $<14$  nm), while rutile phase is more stable in its bulk form. Because of its stability in the nanometer range, anatase is considered more suitable for catalytic applications (21). Anatase also shows superior photocatalytic activity over rutile even though anatase has a wider band gap energy. However, reasons for this phenomenon is still in debate. Zhang *et al.* states that anatase has an indirect band gap while rutile and brookite have direct band gaps. The indirect band gap helps in delaying the recombination of photoexcited electron–hole pairs (22). Also, the photogenerated charge carriers or excitons in anatase can easily diffuse to the surface to take part in photoreduction and photooxidation reactions as they have the lightest average effective mass when compared to rutile and brookite (23). The most commonly used photocatalyst is Degussa P-25, which is a mixture of both rutile ( $\sim 20\%$ ) and anatase ( $\sim 80\%$ ) phases. This mixture ratio has been observed to aid in synergistic effects giving increased photocatalytic activity including  $\text{CO}_2$  reduction (24). The increased photocatalytic activity is due to the formation of a heterojunction, as shown in Fig. 3, that aid in charge carriers being separated and stored in different locations, thereby increasing the time of electron–hole separation. In the case of defective anatase with surface oxygen vacancies and titanium defects ( $\text{Ti}^{3+}$ ),

**Table 1** Crystallography of the three crystal forms of  $\text{TiO}_2$  (19,20).

Crystal form	Crystallography	Space group	Formula units per elementary cell	Band Gap (eV)	Stability at high temperatures
Anatase	Bipyramid Tetragonal	$I4_1/amd$	4	3.2	Stable
Rutile	Tetragonal	$P4_2/mnm$	2	3.0	Metastable
Brookite	Orthorhombic	$Pbca$	8	3.1–3.4	Metastable
$\text{TiO}_2$ (B)	Monoclinic	$C2/m$	8	3.1–4.1	Metastable



**Fig. 3** Heterojunction formed in mixtures of anatase and rutile TiO<sub>2</sub>. CB and VB represent the conduction band and valence band, respectively, while the energy in eV represents the value of the band gap between CB and VB from Table 1.

Liu *et al.* have shown to have a 10-fold higher conversion of CO<sub>2</sub> to CO and CH<sub>4</sub> than the defect free anatase (9). It is also possible with defect rich anatase for an electron to become attached to CO<sub>2</sub> (forming Ti<sup>4+</sup>-CO<sub>2</sub><sup>-</sup>) even in a dark environment (9).

### 2.2.2 Brookite

Brookite is the third naturally occurring polymorph of TiO<sub>2</sub>. Brookite has received little attention as a possible catalyst over the years since it is metastable (13,14). However, a renewed interest on brookite can be seen in the most recent literature. Combinations of anatase and brookite are possible catalysts for CO<sub>2</sub> photoreduction and were tested through charge analysis calculations. It was discovered that the CO<sub>2</sub> radical anion, CO<sub>2</sub><sup>-</sup>, which is the first intermediate in CO<sub>2</sub> conversion, was formed on anatase surfaces and not on the brookite, suggesting brookite as an unsuitable catalyst for this reaction. However, synthesizing brookite (210) with oxygen vacancies enhanced the charge transfer to the CO<sub>2</sub>, promoting the formation of the CO<sub>2</sub><sup>-</sup>. Therefore, brookite with induced oxygen vacancies may be a promising catalyst for the photoreduction of CO<sub>2</sub>. Brookite nanorods with induced oxygen vacancies were also synthesized by Park *et al.* and showed visible light response due to the oxygen vacancies (25). Furthermore, brookite nanocrystals with oxygen vacancies showed higher photocatalytic activity in CO<sub>2</sub> conversion to CO and CH<sub>4</sub> (CO production of 17.25 μmol/g) in comparison with oxygen deficient anatase (CO production of 10 μmol/g) and rutile (CO production ~4 μmol/g) nanocrystals (9).

Anatase-rich/brookite (75:25) mixture was studied to be more active for the photoreduction of  $\text{CO}_2$  than Degussa P-25 or anatase-rich/rutile in similar ratios (14). These results suggest the possibility of adequate electron transfer taking place in brookite-based  $\text{TiO}_2$  composites. However, there is no analytical evidence for the electron transfer (10).

### 2.3 Significance of crystal facets of $\text{TiO}_2$ in photocatalysis applications— $\text{CO}_2$ conversion

The photocatalytic activity depends on the external surface (or the crystal facet) of the catalyst being exposed to the reaction. In other words, crystal facets of  $\text{TiO}_2$  play a significant role in photocatalysis because each crystal facet of  $\text{TiO}_2$  is unique in terms of surface and stereochemistry due to the differing arrangement of the surface atoms on the facets and due to the preferential flow of photogenerated charge carriers (26,27). Each facet has its own contribution in catalysis applications. For example, while the (001) facet of rutile and anatase provide the sites for oxidation, rutile (110) and anatase (101) facets provide the sites for reduction (27). In brookite, the (201) facet is oxidative, while (210) is reductive (13). The most studied facets of anatase are (101), (001), and (011) and for rutile (110), (100), (001), and (011). Different facets have different electronic states. Exposing two different crystal facets to UV illumination in an optimum ratio can lead to a preferential flow of photoexcited electrons and holes in the facets, enhancing the quantum yield. The (001) facet of anatase is a high-surface energy facet with high oxidative abilities, whereas the (101) facet of anatase is a low surface energy facet with high reductive abilities. The surface energies for various crystal facets of anatase are given in Table 2. The high surface energy of (001) facet is because of the 100% presence of fivefold-coordinated titanium atoms ( $\text{Ti}_{5c}$ ) on the surface of the crystal, while the (101) phase only has 50%  $\text{Ti}_{5c}$  (26). D'Arienzo *et al.* quantitated the (001) surface energy using electron spin resonance (ESR) where the recombination of photogenerated electrons and holes are greatly reduced (27).

Approximately 90% of anatase's surface is composed of the thermodynamically stable (101) facet. In a truncated octahedral anatase, eight sides of it are made up of (101) crystal facet with two of (001) facets on top

**Table 2** Average surface energies of the crystal facets of anatase  $\text{TiO}_2$  nanocrystals (26).

Crystal facet of anatase $\text{TiO}_2$ nanocrystals	$\gamma$ (001)	$\gamma$ (100)	$\gamma$ (101)
Average surface energies ( $\text{J/m}^2$ )	0.90	0.53	0.44

and bottom. Therefore, most of the photocatalytic reactions occur as per the performance of the exposed (101) facet. There are interesting unusual physiochemical properties of (001) facet when exposed. It was mentioned in the literature that the photocatalytic activity of the (001) facet-exposed-anatase was higher than the (101) facet-exposed-anatase. The reason being is that the anatase (001) has a high density of active unsaturated Ti atoms and active surface oxygen atoms helping in enhancing the photoactivity (28). Yu *et al.* reported on the photoreduction of CO<sub>2</sub> with coexposed (001) and (101) facets of anatase and the effects of change in the ratio of the mentioned facets in the CO<sub>2</sub> photoreduction to methane process (28). Hydrofluoric acid (HF), a morphology controlling agent (29), was used to create anatase TiO<sub>2</sub> with increased (001) crystal facets along with (101) facet. Increases in the concentration of HF increased the (001) facets on anatase. The CO<sub>2</sub> reduction to methane increased with an increase in (001) facets.

However, a greater increase in (001) facets leads to a decrease in the methane formation. This is because, increase in (001) facet created an electron-overflow effect. With (001) and (101) facets, the electrons need to flow from (001), leaving behind holes into (101) facet for efficient electron-hole separation. As the (101) facets are reduced with increases in surface exposed (001) facets, the migration of electrons to (101) becomes difficult leading to easy recombination of electrons with holes left behind in the (001) facet. Therefore, an optimum amount of (001) and (101) facets must be created on the anatase for efficient photoreduction of CO<sub>2</sub> to methane. The optimum ratio of (101)/(001) facets given by Yu *et al.* was 45:55. An optimum amount of these facets will allow the (101) facet to provide effective reduction and the (001) facet for effective oxidation situations (28). Roy *et al.* has stated that the equal ratios of (101) and (001) and/or (100)/(010) facets provide the best photocatalytic activity. The facets (001) and (101) of anatase also greatly influence the photoconversion of CO<sub>2</sub> (26). It was inferred by Yu *et al.* that the photoreduction of CO<sub>2</sub> to methane was highest (increasing from 0.15 to 1.35  $\mu\text{mol/g h}$ ) with 58% of (001) facet on anatase TiO<sub>2</sub> (28). Synchronous illumination X-ray photoelectron spectroscopy (SIXPS) was used to determine the movement of photoexcited charge carriers. The intact-TiO<sub>2</sub> (intact (001) and (101) facets) had fast recombination of charge carriers, meanwhile optimizing TiO<sub>2</sub> with selectively etching (001) facets showed delayed electron-hole recombination. This delayed recombination of charge carriers was shown to have a sevenfold higher production of hydrogen as compared to the intact-TiO<sub>2</sub> microcrystals (30). The photocatalytic performance also depends on the

crystal size along with the type of crystal facet of  $\text{TiO}_2$ . Tong *et al.* reported that the photodegradation of methylene blue was highest for crystal size of  $1.3\ \mu\text{m}$  with 45% of the surface being (001) crystal facet (29).

The greater influence of (001) facet on the adsorption and reaction of  $\text{CO}_2$  than (101) facet was studied with the help of FTIR and DFT. It was determined that the Ti sites on (001) facet had lower Lewis acidity than (101) facet of  $\text{TiO}_2$  anatase. In addition to this, the surface oxygen sites on anatase  $\text{TiO}_2$  show higher Lewis basicity on (001) facet than the (101) facet. The high basicity of (001) facet of  $\text{TiO}_2$  is the reason behind greater adsorption of  $\text{CO}_2$ , leading to high reactivity and increased conversion.



### 3. The role of lattice defects and their respective crystal facets in $\text{CO}_2$ photocatalysis

$\text{TiO}_2$  has always been an active photocatalyst, showing a higher photoactivity in its reduced form ( $\text{TiO}_{2-x}$ ) constituting of point or lattice defects. Some of the significant and most commonly known point defects of  $\text{TiO}_2$  are oxygen vacancies and titanium defects. The point defects of  $\text{TiO}_2$  have been discussed in detail in later parts of this review. Zhang *et al.* showed an enhanced photoactivity in converting  $\text{CO}_2$  with the presence of  $\text{Ti}^{3+}$  (titanium defect) and oxygen vacancy defects on facets (001) and (111) of  $\text{TiO}_2$  producing CO and  $\text{CH}_4$  under visible light and UV light. The  $\text{TiO}_2$  with defects showed 10-fold greater photoactivity than P25 under visible light and three times greater photoactivity under UV (31).

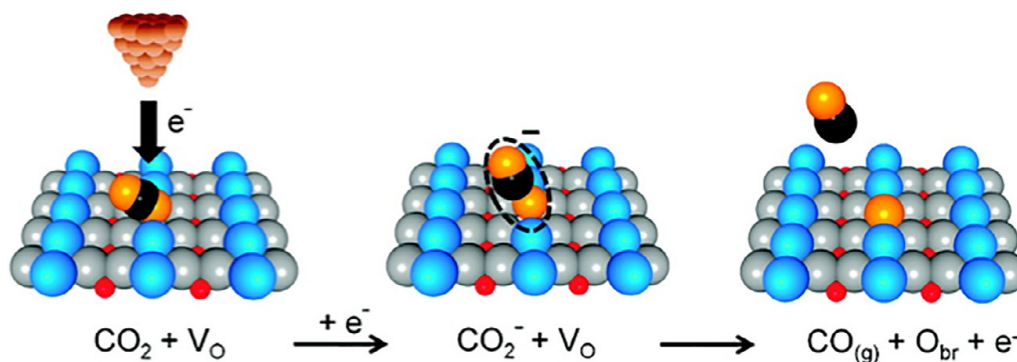
These lattice defects, namely oxygen vacancies and titanium defects, play a significant role in the enhancement of the photoactivity. This is because of two main reasons. First, oxygen vacancies have shown to increase the adsorption of radicals derived from  $\text{H}_2\text{O}$ ,  $\text{O}_2$ , and  $\text{CH}_4$ . In a similar way, oxygen vacancies have also shown to increase the adsorption of  $\text{CO}_2$  on both anatase and rutile surfaces. New adsorption configurations arise for  $\text{CO}_2$  in the presence of oxygen vacancies on (001)  $\text{TiO}_2$  surface providing significant charge transfer to  $\text{CO}_2$  shown by large vibrational red shifts and weakening of product C—O bonds from elongation. Secondly, point defects in reduced  $\text{TiO}_2$  provide more active sites for reactions to take place. These point defects act as initiators and activators in heterogeneous catalytic process (32). Ji and Luo have shown that oxygen vacancies are the real active sites for many reactions on  $\text{TiO}_2$ . In the case of  $\text{CO}_2$  photoreduction, DFT calculations have indicated that the electron transfer to  $\text{CO}_2$  for its reduction is mediated by the surface defects such as oxygen vacancies along with them



playing a key role in water-photocatalyst (TiO<sub>2</sub>) interactions (33). Oxygen vacancies take part in the dissociation of CO<sub>2</sub> on the surface as the first segment of the pathway that eventually converts CO<sub>2</sub> to value added chemicals.

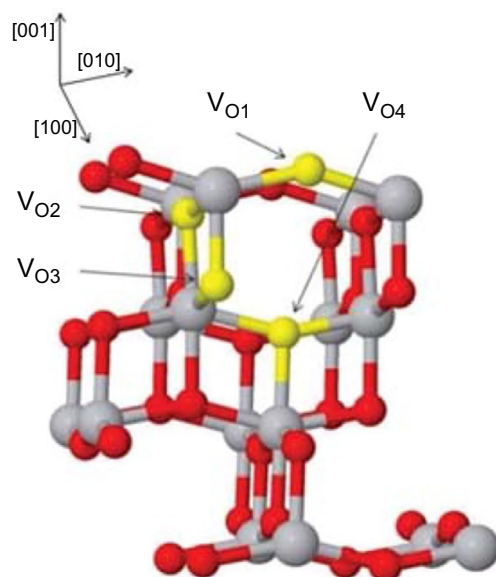
CO<sub>2</sub> activation and dissociation in the presence of an oxygen vacancy was explained by Lee *et al.* The first step of CO<sub>2</sub> activation on the surface of a photocatalyst is electron dissociation of the CO<sub>2</sub> molecule. Scanning Tunneling Microscopy (STM) analysis showed that photo-excited electrons transfer to the conduction band and quickly relax to the bottom of the conduction band. However, CO<sub>2</sub> dissociation lies  $\sim 1.4$  eV above the conduction band minimum of TiO<sub>2</sub>. There is a need, therefore, for a solvent, such as H<sub>2</sub>O or an alcohol, that coadsorbs with CO<sub>2</sub> and facilitates the electron transfer process (34). The role of oxygen vacancies in CO<sub>2</sub> dissociation is shown in Fig. 4.

The Ti<sup>3+</sup> defects formed as a result of oxygen vacancies have also shown to facilitate the photoreduction of CO<sub>2</sub> (32). CO<sub>2</sub> dissociation on a TiO<sub>2</sub> surface is an electron-induced process. The holes cannot dissociate CO<sub>2</sub>. The process of photo reducing CO<sub>2</sub> is a multistep process. The first step is the adsorption of CO<sub>2</sub> onto the TiO<sub>2</sub> surface. CO<sub>2</sub> adsorbs more strongly at the oxygen vacancy sites compared to the defect-free TiO<sub>2</sub> (110) surface. The second step is the activation of CO<sub>2</sub> through transfer of photogenerated electrons from the photocatalyst forming negatively charged molecule CO<sub>2</sub><sup>-</sup> as shown in Fig. 4. The third and final step is the dissociation of CO<sub>2</sub> to form CO. The CO moves away from the reaction site probably because of the excited energy state it is in (i.e., the energy gained from the dissociation process). This process is known as dissociative electron attachment (DEA). DEA appears to occur easily in cases when there is weak interaction



**Fig. 4** Dissociative electron attachment (DEA) schematics of CO<sub>2</sub> conversion to CO in the presence of an oxygen vacancy (V<sub>o</sub>). Removal of oxygen atoms from the bulk or surface a V<sub>o</sub> is formed (34).





**Fig. 5** Different oxygen vacancies and their positions in an anatase (001)  $\text{TiO}_2$  surface. (Ti = gray, O = red, Oxygen vacancy = Yellow) (32).

of  $\text{CO}_2$  with  $\text{TiO}_2$  (i.e., (110)). In the presence of an oxygen vacancy site, the dissociation of  $\text{CO}_2$  is quick as the dissociation of  $\text{CO}_2$  supplies an oxygen atom that heals the oxygen vacancy site, stabilizing the structure.

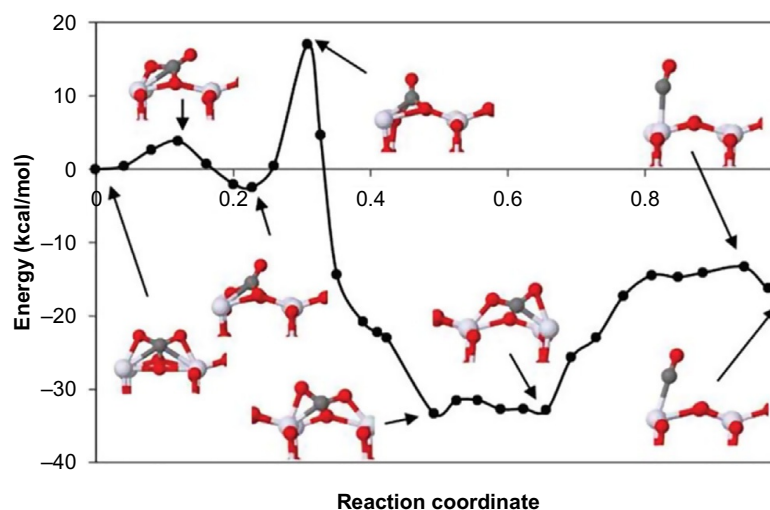
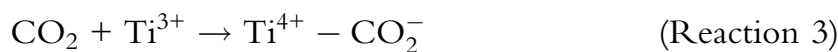
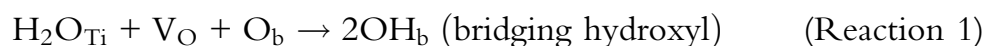
The role of oxygen vacancies in  $\text{CO}_2$  dissociation on  $\text{TiO}_2$  anatase (001) was described by Huygh *et al.* (32). The oxygen vacancies formed in  $\text{TiO}_2$  are given different notations with respect to their positions on the  $\text{TiO}_2$  structure as shown in Fig. 5. Each of them has shown to have a differing role in  $\text{CO}_2$  adsorption and photoconversion. According to the DFT calculations, a strong influence of the defects was observed only when the oxygen vacancy ( $\text{V}_{\text{O}1}$ ) is present in the same row (010) as the  $\text{CO}_2$  adsorbed site on  $\text{TiO}_2$  (adsorbed in the form of B(I) configuration).

The B(I) configuration is the monodentate carbonate structure. In this configuration, the oxygen atoms of  $\text{CO}_2$  bind to fivefold coordinated  $\text{Ti}_{5f}$  centers in the same row (010) and carbon atoms bind to twofold coordinated oxygen atom. The strong destabilization of  $\text{CO}_2$  on  $\text{TiO}_2$  in this case occurs due to both electronic and structural causes. For the electronic causes, the oxygen atoms are the Lewis bases of  $\text{CO}_2$  and bind directly to the Lewis base centers of the surface, which are the  $\text{Ti}^{3+}$  defects generated as a result of oxygen vacancy, causing destabilization and eventual dissociation. For the structural causes,  $\text{TiO}_2$  in the B(I) configuration has an angle of  $145.6^\circ$  whereas the reduced  $\text{TiO}_2$  has an angle of  $102.8^\circ$ . On the adsorption of  $\text{CO}_2$ , the angle increases to  $167.1^\circ$  and introduces stress, causing

destabilization and eventual dissociation. Lower reactions barriers are found in the presence of oxygen vacancies on TiO<sub>2-x</sub>, as one of the oxygen atoms from the CO<sub>2</sub> is used to heal the oxygen vacancy forming CO as the product stabilizing the TiO<sub>2</sub> structure as mentioned earlier (32).

When considering water splitting as an analogy toward CO<sub>2</sub> reduction in the presence of water, a pathway was suggested by Petrik and Kimmel (35). Initially, water adsorbs onto the TiO<sub>2</sub> surface through a precursor-mediated mechanism. Subsequent adsorption of water molecules occurs on Ti<sub>5c</sub> sites and bridging oxygen sites. As the water diffuses along a Ti row and approaches an oxygen vacancy, it is adsorbed onto the vacancy where it then dissociates, creating a pair of bridging hydroxyls (Fig. 6) (35).

A similar pathway can be assumed when considering photoreduction of CO<sub>2</sub> using water as the reductant that provides the necessary hydroxyl radicals. These hydroxyl radicals play a significant role in the photoconversion of CO<sub>2</sub> to CO, CH<sub>4</sub>, etc. A few of the possible reaction pathways (Reactions 1–Reaction 7) for the formation of CO from CO<sub>2</sub> photoreduction with water vapor on oxygen deficient TiO<sub>2</sub> anatase and brookite phases were given by Liu *et al.* (9) (Fig. 7).



**Fig. 6** Minimum energy pathway for CO<sub>2</sub> dissociation starting from B(l) on reduced Anatase (001) surface with no V<sub>O2</sub> and with no zero-point energy corrections (34).

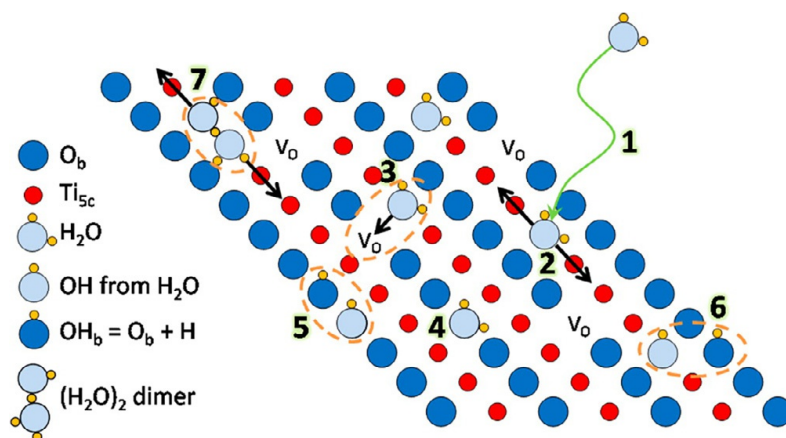
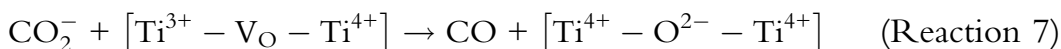
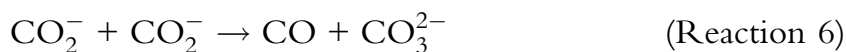


Fig. 7 Reaction schematics of H<sub>2</sub>O on reduced TiO<sub>2</sub> (110) (35).

**Table 3** Photocatalytic conversion of CO<sub>2</sub> to CO and CH<sub>4</sub> from defect rich polymorphs of TiO<sub>2</sub> (9).

Defect rich TiO <sub>2</sub> polymorph	CO Production (μmol/g)	CH <sub>4</sub> Production (μmol/g)
Anatase	10	12.8
Rutile	4	4.1
Brookite	17	18.9



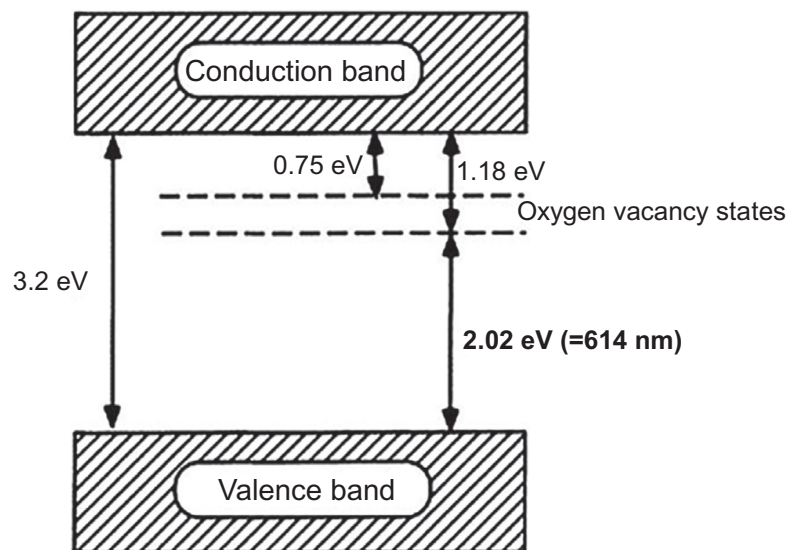
As discussed earlier, brookite may be a promising photocatalyst for CO<sub>2</sub> conversion. Liu *et al.* compared the photoreduction of CO<sub>2</sub> in the presence of water using different polymorphs of defect rich TiO<sub>2</sub>. Brookite, with surface engineered defect sites, showed the highest yield when compared to anatase and rutile for CO and CH<sub>4</sub> production from CO<sub>2</sub> as shown in Table 3. The reasons discussed were easier formation of oxygen vacancies due to low formation energy of oxygen vacancy on brookite and/or a quicker reaction of CO<sub>2</sub><sup>-</sup> with adsorbed H<sub>2</sub>O or surface OH groups (9).

In addition, these point defects provide the solutions for the two major limitations of a photocatalytic process: (1) the low quantum yield or restricted harvesting of low energy light and, (2) the easy recombination of charge carriers. The most important objective pursued while developing efficient TiO<sub>2</sub>-based photocatalysts is to obtain at least the same, if not

better, visible light absorption, possibly from solar energy with increased electron–hole pair separation.

Absorption of visible light has been accomplished either by narrowing the band gap or by nanoengineering the surface structure with defects. The optical absorption can be enhanced by implanting structural defects. Implanted defects create energy states in the band gap between the conduction band (CB) and the valence band (VB) which leads to a new set of absorption transitions of lower energy within this band gap (36). The energy states created due to defects leading to enhanced photoactivity even in visible light in TiO<sub>2</sub> is explained in detail in the following paragraph.

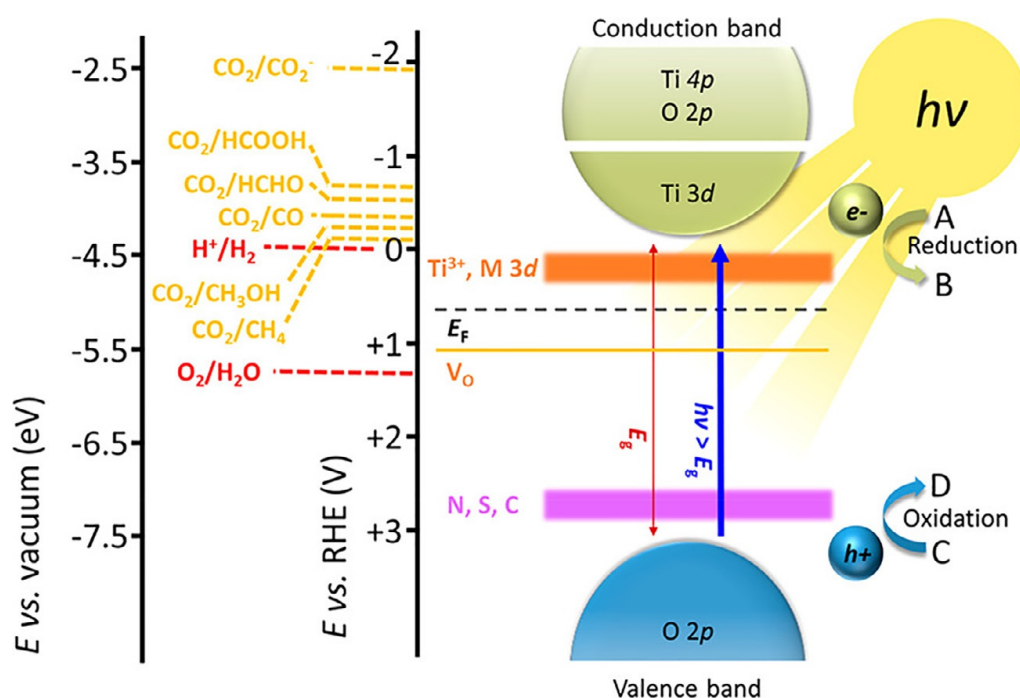
The formation of point defects in TiO<sub>2</sub> brings changes in the electronic interactions in the bulk TiO<sub>2</sub> including the Fermi energy value (which in turn affects the photocatalytic performance of TiO<sub>2</sub>). In semiconductors the Fermi level is an energy level located between upper energy of the valence band and the lower energy of the conduction band. The position of the Fermi level depends upon the defect disorder and the density of electrons. The placement of the Fermi level is also one of the parameters in determining the enhancements in the photocatalytic activity of TiO<sub>2</sub>. For example, an increase in electron density along with the presence of point defects such as, oxygen vacancies V<sub>O</sub> and titanium defects Ti<sup>3+</sup> in black TiO<sub>2</sub> NT leads to modification in the built-in local electric dipoles causing upward shift of the Fermi level. The localization of one or two electrons in the lattice of TiO<sub>2</sub> takes place with removing oxygen atoms from bulk or



**Fig. 8** The donor electronic states emerging below the conduction band of anatase are due to a missing oxygen atom due to removing the oxygen from the lattice of TiO<sub>2</sub> (37).

surface thus forming oxygen vacancies. The driving intersection for explaining such localization to occur in a highly ionic crystal is the long-range Madelung potential. These electrons form donor levels below the conduction band of  $\text{TiO}_2$  located at 0.75–1.18 eV below the conduction band of  $\text{TiO}_2$  crystal as shown in Fig. 8 (37).

For example, in black  $\text{TiO}_2$ , the surface disorders such as the oxygen vacancy defects introduce localized states at 0.7–1.0 eV below the CB minimum. As a result, electronic transitions can take place from VB to these localized states and next from these states to CB under lower energy light such as visible and NIR light (7). The energy of these donor states increases with the increasing number of oxygen vacancies, and eventually leads to higher energy shift of the Fermi level through a larger electron mobility. This higher energy shift of the Fermi level corresponds to faster movement of electrons and thus increased photocatalytic activity (37,38). The general positioning of the Fermi level in the reduced  $\text{TiO}_2$  with defects in photocatalysis for  $\text{CO}_2$  reduction to CO, HCOOH,  $\text{CH}_4$  and water splitting to oxygen and hydrogen is shown in Fig. 9 (38).



**Fig. 9** Schematic representation of photocatalytic reduction of  $\text{CO}_2$  and water splitting taking place in  $\text{TiO}_2$  and the corresponding Fermi level positioning  $E_F$ . The energy states represented in orange color is due to the defect states such as oxygen vacancy and  $\text{Ti}^{3+}$  defects between Fermi level and the conduction band minimum (38).

Furthermore, introducing large amounts of Ti<sup>3+</sup> defects into brookite nanoparticles has shown increased solar energy absorption with enhanced photocatalytic reduction of CO<sub>2</sub> (13). The enhanced photoreduction is likely due to the increased charge carrier separation whose pathway can be explained by:

Oxygen vacancies → excess electrons trapped by Ti<sup>4+</sup> → Ti<sup>4+</sup> to Ti<sup>3+</sup> → high conductivity + increased electron–hole separation (13).

The longer the charge carriers are separated, the more time that is available for the oxidation and reduction reactions to take place in a photocatalyst. This leads to higher photoactivity in organic pollutant degradation, hydrogen production, and CO<sub>2</sub> reduction.



## 4. Defects in the TiO<sub>2</sub> crystalline structure

Different forms of structural imperfections exist in crystalline solids. These imperfections have a significant effect on specific crystal properties such as the transport of charge carriers, reactivity, and photo-reactivity (39,40). Defect engineering on TiO<sub>2</sub> nanocrystalline materials leads to the creation of highly disordered TiO<sub>2</sub> surfaces with a large number of oxygen vacancies providing not only efficient visible and near infrared light absorption but also high photocatalytic activity in organic compound degradation and hydrogen production. These developments were implemented into CO<sub>2</sub> photoreduction. The point defects were stated to help in CO<sub>2</sub> activation along with enhanced CO<sub>2</sub> photoreduction due to the increased electron donor density promoting efficient charge transport (41). The different types of structural imperfections (or defects) are point defects, planar defects, and spatial defects. Point defects are thermodynamically reversible. The formation of these defects, as well as their concentration, depends on the surrounding gas partial pressure and the temperature of the system. Planar and spatial defects are thermodynamically irreversible defects and are independent of temperature and chemical composition of the surrounding gas (40).

### 4.1 Point defects

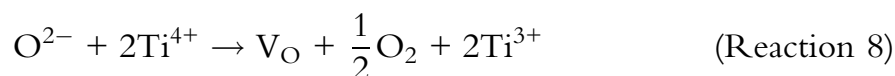
TiO<sub>2</sub>, a nonstoichiometric solid, can be oxidized or reduced within a single phase leading to the formation of defects in the crystal lattice. These defects are known as point defects (42). Point defects can be intrinsic or extrinsic. This review will largely concentrate on the intrinsic point defects of TiO<sub>2</sub>. Until recently, the known intrinsic point defects (also known as Wadsley



defects) of  $\text{TiO}_2$  have been oxygen vacancies, titanium vacancies, titanium interstitials, and reduced forms of  $\text{TiO}_{(2-x)}$  (2,43,44). Point defects play a very significant role in most of the surface reactions including photocatalytic reactions as they are efficient reactive agents for many adsorbates (45).

#### 4.1.1 Intrinsic point defects of $\text{TiO}_2$

Intrinsic defects are n-type defects (45). These defects are named by two different types of notations known as traditional notation and Kröger–Vink notations Table 4. The most important one in discussing this work is the Oxygen Vacancy Defect ( $V_O$ ). The Oxygen vacancy defect refers to the missing of an oxygen ion from its lattice site (46,47).  $\text{TiO}_2$  can undergo a loss of oxygen forming surface or bulk vacancies. These oxygen vacancies bring changes to electronic and chemical properties of  $\text{TiO}_2$ . They not only help in enhancing the performance of  $\text{TiO}_2$  but also in enhancing the photocatalytic performance when being used as an anchor or catalyst support for metals like gold and copper nanoparticles (48). These vacancies also aid in the formation of  $\text{Ti}^{3+}$  point defects (Reaction 8) which also takes part in the charge transfer process (49).



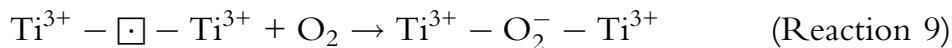
These oxygen vacancies also tend to disappear in the presence of oxygen atmosphere. The possible pathway for such a situation is given in by

**Table 4** Notations for the point defects (46).

Description	Traditional notation	Kröger–Vink notation
Oxygen vacancy	$V_O$	$V_{\ddot{O}}$
Titanium vacancy	$V_{Ti}$	$V_{Ti}'''$
$Ti_{Ti}^{4+}$ ion in the titanium lattice site	$Ti_{Ti}^{4+}$	$Ti_{Ti}^x$
$Ti_i^{4+}$ ion in the interstitial site	$Ti_i^{4+}$	$e^-$
$Ti_{Ti}^{3+}$ ion in the titanium lattice site (quasi free electrons)	$Ti_i^{3+}$	$Ti_i^{\cdot\cdot}$
$Ti_i^{3+}$ ion in the interstitial site	$Ti_i^{3+}$	$Ti_i^{\cdot\cdot}$
$O_O^{2-}$ ion in the oxygen lattice site	$O_O^{2-}$	$O_O^x$
$O_O^-$ ion in the oxygen lattice site	$O_O^-$	$h^\bullet$



Reaction (Reaction 9) (48). Oxygen vacancy defects are also important because they increase the Lewis basicity of the TiO<sub>2</sub> surface which help in increasing the adsorption of CO<sub>2</sub> on the anatase and TiO<sub>2</sub> rutile surfaces.



As pointed out by Nowotny and coworkers, titanium vacancies also contribute to intrinsic TiO<sub>2</sub> defects. During calcination, titanium vacancies are formed when oxygen is adsorbed and participates in the subsequent building of new lattice elements. Under reducing conditions (i.e., calcination using H<sub>2</sub> or inert atmosphere), titanium ion may “jump” from its lattice site into an interstitial site (47).

#### 4.1.2 Extrinsic point defects of TiO<sub>2</sub>

Point defects in TiO<sub>2</sub> arising from doping with external elements, metals or nonmetals, (such as C, V, W, Fe, S, N, Ba, and Sn) are termed as extrinsic point defects of TiO<sub>2</sub> (50). For example, oxygen vacancies in TiO<sub>2</sub> can be created by doping TiO<sub>2</sub> with metal ions such as Ba<sup>2+</sup>, and lattice distortion can be created by Sn<sup>2+</sup> doping. Sn<sup>2+</sup> (metal ion) induced lattice distortion was studied by Yang *et al.* (51). The Sn<sup>2+</sup> ionic radius is larger than the ionic radius of Ti<sup>4+</sup>. The Sn<sup>2+</sup> ions occupy only the interstitial sites of TiO<sub>2</sub> resulting in severe lattice disorder. Changing the concentrations of the metal ion changes the surface to bulk defects ratio. An appropriate surface to bulk defect ratio can increase the electron–hole separation efficiency. Doping with Ag creates Ti<sup>3+</sup> defects as reported by Saravana *et al.* X-ray Photoelectron Spectroscopy (XPS) characterization reveals that the incorporation of Ag leads to the reduction in Ti binding energy, showing the partial reduction of Ti<sup>4+</sup> to Ti<sup>3+</sup> (52).

Xing *et al.* showed increase in CH<sub>4</sub> yield from CO<sub>2</sub> by 13 times from 0.125 to 1.63 μmol/g<sub>cat</sub> h under solar light with methane selectivity improved from 25.7% to 85.8% by fluorination of TiO<sub>2-x</sub> (53). The F atoms aid in improving the reduction potential of TiO<sub>2-x</sub> by being substituted into the oxygen vacancies of reduced TiO<sub>2</sub>. From Fluorine’s strong electron-withdrawing property, electrons are withdrawn from Ti<sup>3+</sup> defects and converts them to Ti<sup>4+</sup>. The CH<sub>4</sub> selectivity and yield under photocatalytic condition is a result of an electric field that upsweeps the Ti<sup>3+</sup> impurity level enhancing the reduction potential. This strategy is yet to be readily implemented as it entails major photocatalytic disadvantages

such as, increased charge carrier combination, heterogeneity, and low thermal stability (54). Additionally, solvents such as ethylene glycol, ethanol, polyethylene glycol can also induce surface disorder in  $\text{TiO}_2$  nanoparticles. The solvent molecules bind to the  $\text{TiO}_2$  nanocrystal surface forming C—H and C—O—Ti bonds eventually resulting in a thick disordered surface layer. The solvent acts as a reducing agent, partially reducing  $\text{TiO}_2$  to an oxygen vacant  $\text{TiO}_{2-x}$ .

## 4.2 Planar defects

Some of the planar defects are shear planes and grain boundaries (40). Initial oxygen deficiency in  $\text{TiO}_2$  leads to the formation of point defects. Additional increases in oxygen vacancies lead to the formation of shear planes (43). Subsequently, a phase transition occurs in shear planes to form oxygen deficient phases known as Magneli phases. Magneli phases are formed by heat-treating  $\text{TiO}_2$  in a reducing atmosphere. These Magneli phases have a chemical formula  $\text{Ti}_n\text{O}_{2n-1}$  ( $n=4-9$ ) (55). In  $\text{Ti}_n\text{O}_{2n-1}$ , every  $n$ th layer has an oxygen deficiency. Shear planes rearrange themselves to accommodate the oxygen vacancies forming Magneli phases. These Magneli phases have been investigated to have exceptional electrical conductivity and chemical stability in aggressive acidic and alkaline mediums and have promising applications in photocatalysis (12).

Grain boundaries, on the other hand, are responsible for the movement of electrons and trapping of electrons in polycrystalline  $\text{TiO}_2$ . The transport of electrons in  $\text{TiO}_2$  is determined by the chemical potential of electrons at the interfaces such as grain boundaries (46). The transport of electrons between the grain boundaries can be hampered by creating disturbances in the electrostatic potential of polycrystalline  $\text{TiO}_2$ , creating a large number of trapping sites for electrons. Electron trappings are highly significant in photocatalytic processes as they increase the time of electron–hole separation making grain boundaries an essential research area in photocatalysis. Electron trappings can be calculated theoretically using DFT calculations. Wallace and McKenna provided an insight into the interaction of electrons with the grain boundaries using kinetic Monte Carlo simulations (56). One of the other types of defects formed in  $\text{TiO}_2$  are spatial defects. These defects are three-dimensional defects and are formed by heterogeneous doping by dispersing small particles of one phase of  $\text{TiO}_2$  into a host phase of  $\text{TiO}_2$  (40).

## 5. Methods to synthesize lattice disorder engineered TiO<sub>2</sub>

Synthesis of oxygen vacancies ultimately leads to lower bandgap energies (i.e., energy required to move an electron from the valence band to the conduction band). Oxygen vacancies promote structural relaxations, leading to a decrease in bandgap energy from 3.2 to 2.4 eV (47). There are generally four methods used to induce intrinsic point defects in TiO<sub>2</sub>.

1. Annealing in vacuum at high temperatures
2. Reaction of the TiO<sub>2</sub> precursor with reducing agents at high temperatures
3. Ion bombardment, electron bombardment, and plasma engraving.
4. UV radiation

### 5.1 Annealing in vacuum at high temperature

Annealing TiO<sub>2</sub> in a vacuum at  $\sim 900$  K creates bridging oxygen vacancies  $\sim 5\%$ – $10\%$  of the total concentration on TiO<sub>2</sub> (110) surface (58). Fig. 10 shows an illustration of the bridging oxygen vacancy in TiO<sub>2</sub> (110) (57). Surface oxygen vacancies and Ti<sup>3+</sup> defects are the result of annealing, whereby sub energy levels below the CB are created. The band gap of the TiO<sub>2</sub> is now lowered causing a red-shift of the reaction. The photoreduction of CO<sub>2</sub> to CH<sub>4</sub> (450–620 nm wavelength) have been shown using annealed TiO<sub>2</sub> (24).

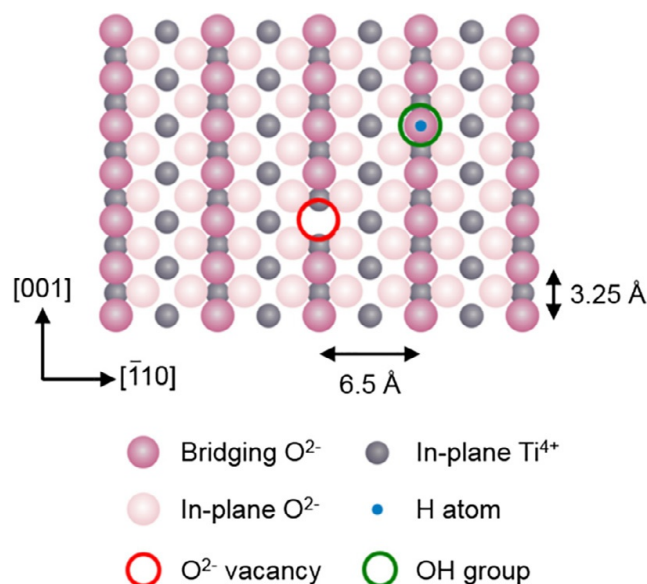
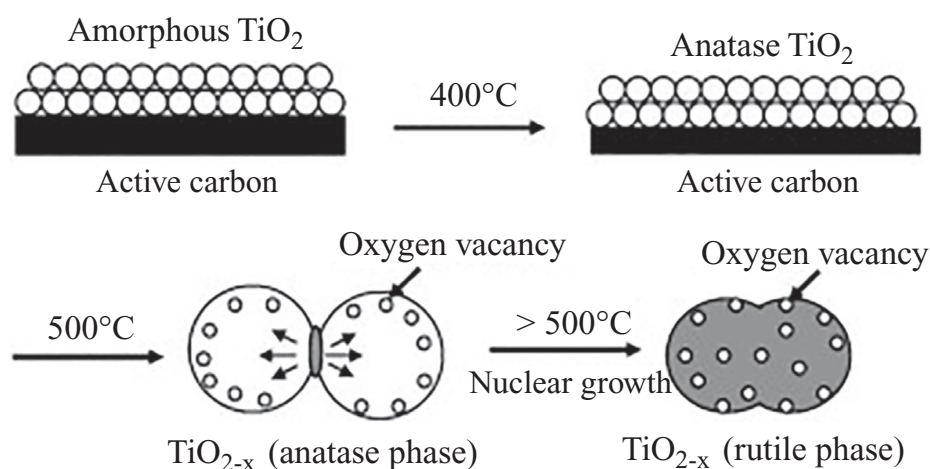


Fig. 10 Depiction of oxygen vacancy in rutile TiO<sub>2</sub> (110) (57).

## 5.2 Titanium dioxide precursor with reducing agents at high temperatures

Some of the reducing agents currently used in creating defect rich  $\text{TiO}_2$  by reacting with a  $\text{TiO}_2$  precursor at high temperatures are hydrogen, carbon, and aluminum. Yang *et al.* reduced titanium (IV) tetra isopropoxide, a titanium dioxide precursor, with active carbon at high desirable temperatures in the presence of air (59). The synthesis procedure, as shown in Fig. 10, creates  $\text{Ti}^{3+}$  defects by reducing  $\text{Ti}^{4+}$  ions to  $\text{Ti}^{3+}$  ions and forming oxygen vacancies  $\text{TiO}_{(2-x)}$  in the process. Oxygen vacancies in anatase phase were obtained at 500 °C and rutile phase with oxygen vacancies above 500 °C (59). The indication of oxygen vacancy in  $\text{TiO}_2$  can be seen from the change of its color from white to yellow or blue. The reduced state of Ti in  $\text{TiO}_2$  can be confirmed from electrical conductivity measurements as the  $\text{Ti}^{3+}$  reduced state has higher electrical conductivity than  $\text{Ti}^{4+}$  state. Hydrogen treatment of fine rutile phase at temperatures around 600–800 °C can also be used to create oxygen vacancies. However, using carbon instead of hydrogen is a low-cost method with simple operation (Fig. 11) (59).

Hydrogenation techniques to create black anatase with lattice disorders for enhanced solar absorption was introduced by Chen. Chen synthesized black  $\text{TiO}_2$  nanoparticles with surface disorders by placing the synthesized  $\text{TiO}_2$  nanocrystals in a hydrogen atmosphere for 5 days at 200 °C and 20 bar (7). Introducing dopants into these disordered surfaces induces mid-gap



Formation of oxygen vacancy  $\text{TiO}_{2-x}$  by active carbon reduction

Fig. 11 Formation of oxygen vacancy  $\text{TiO}_{2-x}$  by active carbon reduction (59).

states resulting in shifting the light absorption from blue to infrared or visible light region. These mid gap states are also named as band tail states overlapping with the conduction band edge. Naldoni *et al.* synthesized black TiO<sub>2</sub> under hydrogen atmosphere at 500 °C for 1 h followed by fast cooling in inert atmosphere. This black TiO<sub>2</sub> was stable for more than 10 months in air which was believed to be due to the presence of Ti<sup>3+</sup> in the bulk rather than on the surface (60).

Maintaining a hydrogenation environment is difficult and other methods to produce black defect-rich TiO<sub>2</sub> was investigated. Zhu developed successful reduction of graphene oxide using aluminum with low a C/O ratio (61). In addition, brookite with high photocatalytic activity was synthesized using aluminum. Aluminum, acting as a reductant, reduced the oxygen partial pressure providing the kinetic driving force needed to form lattice disorders and oxygen vacancies on the surface. Creating defects such as Ti<sup>3+</sup> and oxygen vacancies in brookite by reducing brookite TiO<sub>2</sub> to TiO<sub>2</sub>@TiO<sub>2-x</sub> with aluminum in a two-zone furnace has shown to enhance both visible light and near infrared light absorption (61).

### 5.3 Ion or electron bombardment

Bombarding clean and flat surfaces of TiO<sub>2</sub> (110) with Ar<sup>+</sup> (3 keV,  $8 \times 10^{16}$  ions/cm<sup>2</sup>) at room temperature leads to the formation of TiO (001) thin film on TiO<sub>2</sub> (110) surface. This ion bombardment generates interstitial Ti cations which have been hypothesized to migrate to the interface and transformed into a TiO thin film (62). Electron bombardment produces oxygen vacancies while keeping the interstitial Ti defects in the subsurface unaffected (or at least constant), which is not the case with the annealing technique. Oxygen atoms can be removed from the anatase surface (101) similar to rutile through electron bombardment producing oxygen vacancies (62). Payne *et al.* bombarded TiO<sub>2</sub> anatase (101) (1 × 1) single crystal with cycles of Ar<sup>+</sup> sputtering for 30 min followed by thermal annealing up to ~950 K for 10 min. The created oxygen vacancies travel to the sub-surface of the TiO<sub>2</sub>. Additional surface oxygen vacancies were created by bombarding the sample with electrons emitted from an electron gun (500–550 eV, 13 μA/mm<sup>2</sup>). These oxygen vacancies induce Ti 3d band gap states ~1 eV below the Fermi level and also lead to the formation of a small polaron at the surface of the anatase (101) crystal facet (63).

Kong *et al.* created defects such as oxygen vacancies and Ti<sup>3+</sup> on TiO<sub>2</sub> through plasma engraving of TiO<sub>2</sub> (B) nanosheets in argon atmosphere.

The plasma source used was Harrick Plasma (13.56 MHz/18 W RF). The chamber pressure was 40 Pa and engraving time was 2 h (64).

## 5.4 UV irradiation

Exposing  $\text{TiO}_2$  (110)–( $1 \times 2$ ) surface to UV irradiation creates line defects along the (001) direction of  $\text{TiO}_2$  (58). Charge trapping centers such as  $\text{Ti}^{3+}$ ,  $\text{O}^-$ , and  $\text{O}_2^-$  can be introduced by exposing the  $\text{TiO}_2$  catalyst nanoparticles to the UV irradiation of 150 W Xe UV lamp. The setup has  $\text{TiO}_2$  catalyst nanoparticles placed in a high vacuum quartz tubes (similar to those used in electron spin resonance spectroscopy) (27). In the photo-assisted preparation of titania colloids, exposure to 290 nm UV irradiation with a 500 W high pressure Hg lamp for 8 h during the sol–gel process has been shown to induce oxygen vacancy defects (65).

One of the other methods through which point defects can be introduced include the oxidation of titanium foils. Either complete or partial oxidation of Ti foils is known to produce a rich diversity of morphologies. Pan *et al.* was able to synthesize brookite-rich  $\text{TiO}_2$  through the partial oxidation of Ti foils with a high density of defects (66). Oxidation of Ti foils at temperatures below 700 °C produces dominant phase of brookite, whereas >700 °C produces rutile as the dominant phase. The formation of Ti interstitials and Ti vacancies depends on the temperature in Ti foil oxidation which affects the rate of oxidation. At comparatively lower temperatures (500–600 °C) there is a slower rate of oxidation that result in an increased supply of Ti (Ti foil) forming Ti interstitials within small  $\text{TiO}_2$  particles. At mid temperatures (600–800 °C), the fast rate of oxidation results in a lower supply of oxygen (i.e., oxygen vacancies), and Ti vacancies are formed 1000 °C (66). Liu *et al.* generated  $\text{Ti}^{3+}$  defects in  $\text{TiO}_2$  through a unique method, without any reductants, by rapid ice water quenching of pre annealed  $\text{TiO}_2$  (annealed at temperature range 800–1200 °C for 2 h). This method also resulted in surface lattice distortions, which increased by increasing the pre annealed temperature (54).



## 6. Origin of intrinsic lattice defects in anatase, rutile, and brookite phases

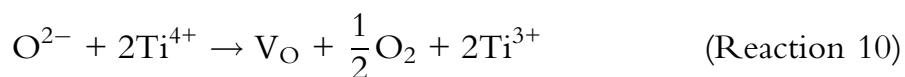
The ability to control and construct oxygen vacancies and other point defects on the required regions of the photocatalyst surface is of great importance. Appropriately controlled oxygen vacancies or defects can be used as efficient charge carrier separation centers rather than charge carrier



recombination centers. The challenge is to control the amount of point defects and construct it as required. Therefore, fundamental understanding of the origin of the defect states or point defects/lattice defects is of great importance. Additionally, it is also necessary to understand the origin of the defects to improve and develop the scope of TiO<sub>2</sub>-based systems for applications involving heterogeneous catalysis, photocatalysis, and waste remediation (67).

DFT calculations have shown that the formation of point defects such as oxygen vacancies and titanium interstitials follow the order brookite < anatase < rutile at energies 5.52, 5.58, and 5.82 eV, respectively. These results demonstrate that it is easier for surface defects to originate on brookite than on rutile. Schneider *et al.* studied lattice changes in TiO<sub>2</sub> upon intense laser pulse illumination. Laser (355 nm) illumination of the TiO<sub>2</sub> samples led to the removal of oxygen, leaving behind four additional electrons that either stay in the vacancy forming *F*-centers (oxygen vacancy with trapped electron) or they reduce Ti<sup>4+</sup> to Ti<sup>3+</sup> (68).

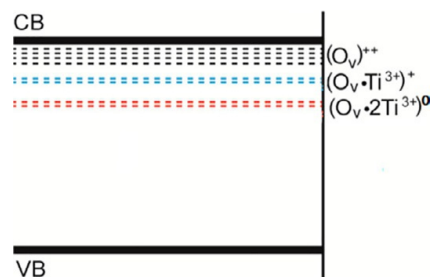
The photo-desorption of oxygen atoms upon laser excitation from the metal oxide surface has been described to follow two mechanisms: (1) photo-thermic and (2) photoelectronic processes. Photothermic is the excitation of the vibrational mode of the surface atom bond followed by the breaking of the bond releasing oxygen with excitation energy transferred to form phonon energy. Photoelectronic is the change of potential energy of the surface atoms to kinetic energy due to the absorption of excitation energy from the laser leading to oxygen desorption from lattice forming oxygen vacancies which eventually lead to the formation of Ti<sup>3+</sup> centers (Reaction 10) (68).



Xu *et al.* used lattice distortions to introduce Ti<sup>3+</sup> defects into TiO<sub>2</sub> microspheres. These lattice distortions were synthesized by modifying the hydro-thermal synthetic procedure of TiO<sub>2</sub> preparation using the precursor Ti(SO<sub>4</sub>)<sub>2</sub> with the addition of NaCl. Distortions in the lattice were produced by introducing chlorine ions that caused surface stresses on the TiO<sub>2</sub> crystals. These distortions produced Ti<sup>3+</sup> defects from the reduction of Ti<sup>4+</sup> to Ti<sup>3+</sup> ions. XPS analysis was used to detect the presence of Ti<sup>3+</sup> defects (39).

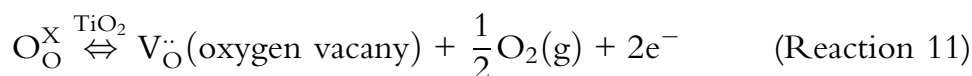
Oxygen vacancies can be formed on anatase by annealing pure TiO<sub>2</sub> at high temperatures in an oxygen poor environment (i.e., He, N<sub>2</sub>, or Ar atmosphere). The formation of oxygen vacancies through this procedure can be governed by Reaction (Reaction 11). This reaction is reversible,





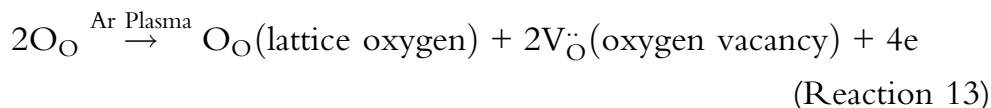
**Fig. 12** Proposed energy level structure inside the band structure of  $\text{Ti}^{3+}$  self-doped quenched  $\text{TiO}_2$  with oxygen vacancies (54).

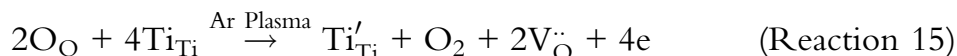
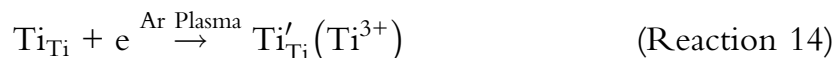
and the vacancies can disappear in the presence of air even at room temperature. One of the methods suggested by Wu *et al.* to make this reaction irreversible was through introducing acceptor-type dopants, such as  $\text{Fe}^{3+}$ , for ion-charge compensation that would stabilize the oxygen vacancies (Reaction 12). This reaction is irreversible due to the stabilization of oxygen vacancies (69).



Liu *et al.* studied  $\text{TiO}_2$  lattice distortion,  $\text{Ti}^{3+}$ , and oxygen vacancy defects formed by rapid quenching pre-annealed  $\text{TiO}_2$  in 4 °C water. The rapid quenching was said to shrink the surface layer of  $\text{TiO}_2$  allowing for lattice distortions and poly-crystallization of the  $\text{TiO}_2$  surface. The oxygen vacancies formed from pre-annealing could be partially frozen when quenched at low temperatures. The free electrons associated with these frozen oxygen vacancies are transferred to  $\text{Ti}^{4+}$  sites leading to  $\text{Ti}^{3+}$  defects. The proposed energy level inside the band gap structure is shown in Fig. 12 (54).

The pathway for the formation of oxygen vacancies and titanium defects is given by Kong *et al.* (Reaction 13–Reaction 15). In the process of synthesizing defect rich  $\text{TiO}_2$  using hydrogen as the reductant, oxygen vacancies originate by overcoming the activation energy of  $\text{TiO}_2$  lattice arrangement when  $\text{TiO}_2$  host matrix interacts with the hot hydrogen molecule. In rutile, creating disturbances in the electrostatic potential near grain boundaries induces Ti sites as electron traps (46).



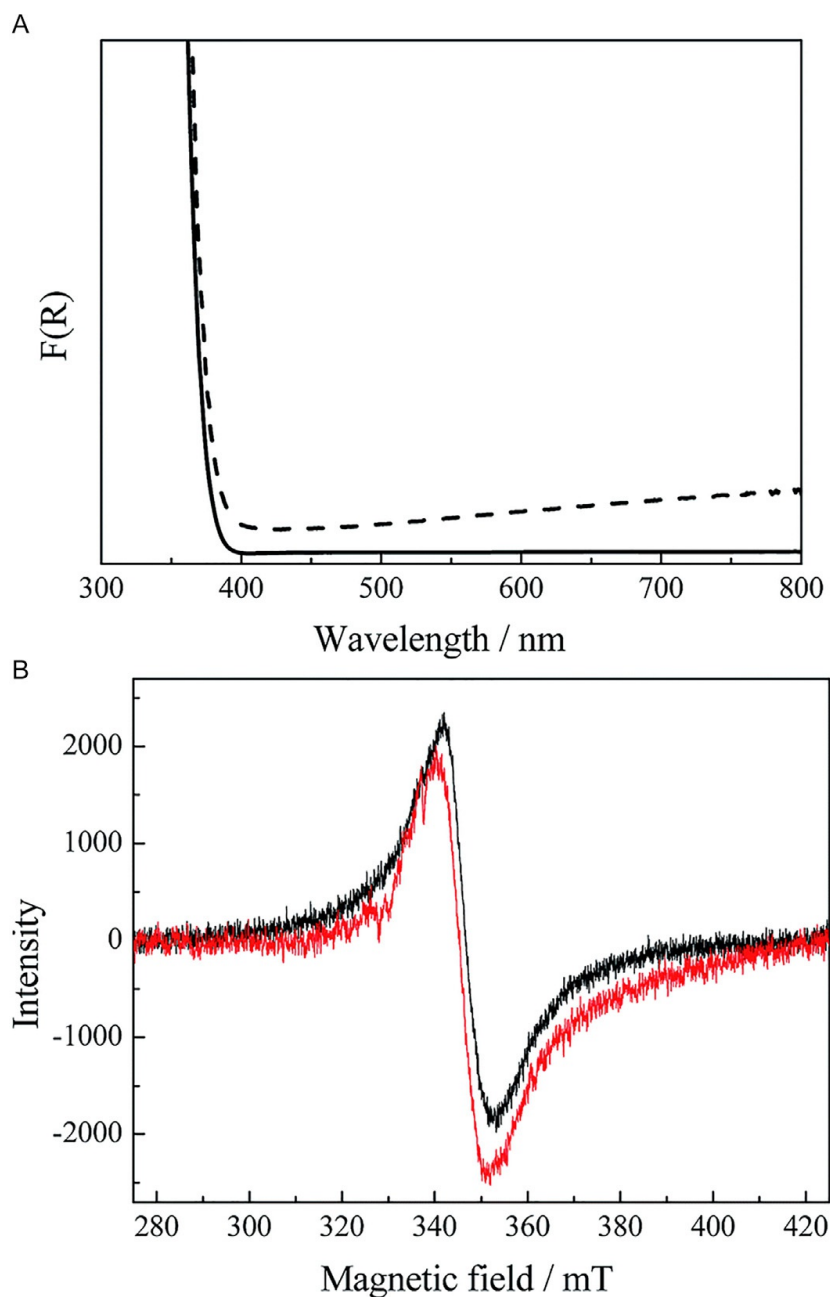


## 7. Recently developed methods for characterizing the lattice defects of TiO<sub>2</sub>

To understand the structure of defects, their role in surface chemistry, and their respective charge transport properties which play a significant role in photocatalytic applications as discussed earlier, well developed real space characterization techniques must be established. Also, an atomic scale study of the structural and electronic properties of the catalyst surface allows for the understanding of the role of point defects in a catalytic process and ways to control the chemical activity associated. Experimental and theoretical techniques have been developed over the years to study lattice or point defects. Experimentally techniques include analytical methods, such as scanning tunneling microscopy (STM), time resolved photo luminescence spectroscopy (PL), and electron paramagnetic resonance spectroscopy (61). Theoretical techniques, including first principle calculations and density functional theories, have been used (70).

### 7.1 Experimental techniques

Initial characterization of defects can be performed through examination of color change in the material when treated to induce defects. The variation in color of TiO<sub>2</sub> parallels to the different types of defects (71). The existence of oxygen vacancies was seen through change in colors in treated and untreated TiO<sub>2</sub>. Liu *et al.* observed that the color changed to brownish gray for anatase and gray for brookite, representing the formation of oxygen vacancies. These results were later confirmed with the help of diffuse reflectance infrared Fourier transform spectroscopy (DRIFTS) characterization. After doping TiO<sub>2</sub> with niobium, Kong *et al.* noticed the change in color of TiO<sub>2</sub> from colorless to yellow (64). The yellow color increased with increased niobium content. The yellow color is believed to be due to the presence of peroxo species and due to the creation of bulk Ti<sup>3+</sup> defect states that arise from charge compensation with niobium. Such type of defects can be studied using various spectroscopic techniques, including electron paramagnetic resonance (EPR), positron annihilation lifetime spectroscopy (PALS), 3D-AFM, and STM-AFM combination (71). Using EPR,



**Fig. 13** EPR spectra of UV-VIS illuminated  $\text{TiO}_2$  polymorphs at 77 K of  $\text{TiO}_2$  anatase (black) and  $\text{TiO}_2$  rutile (red) (68).

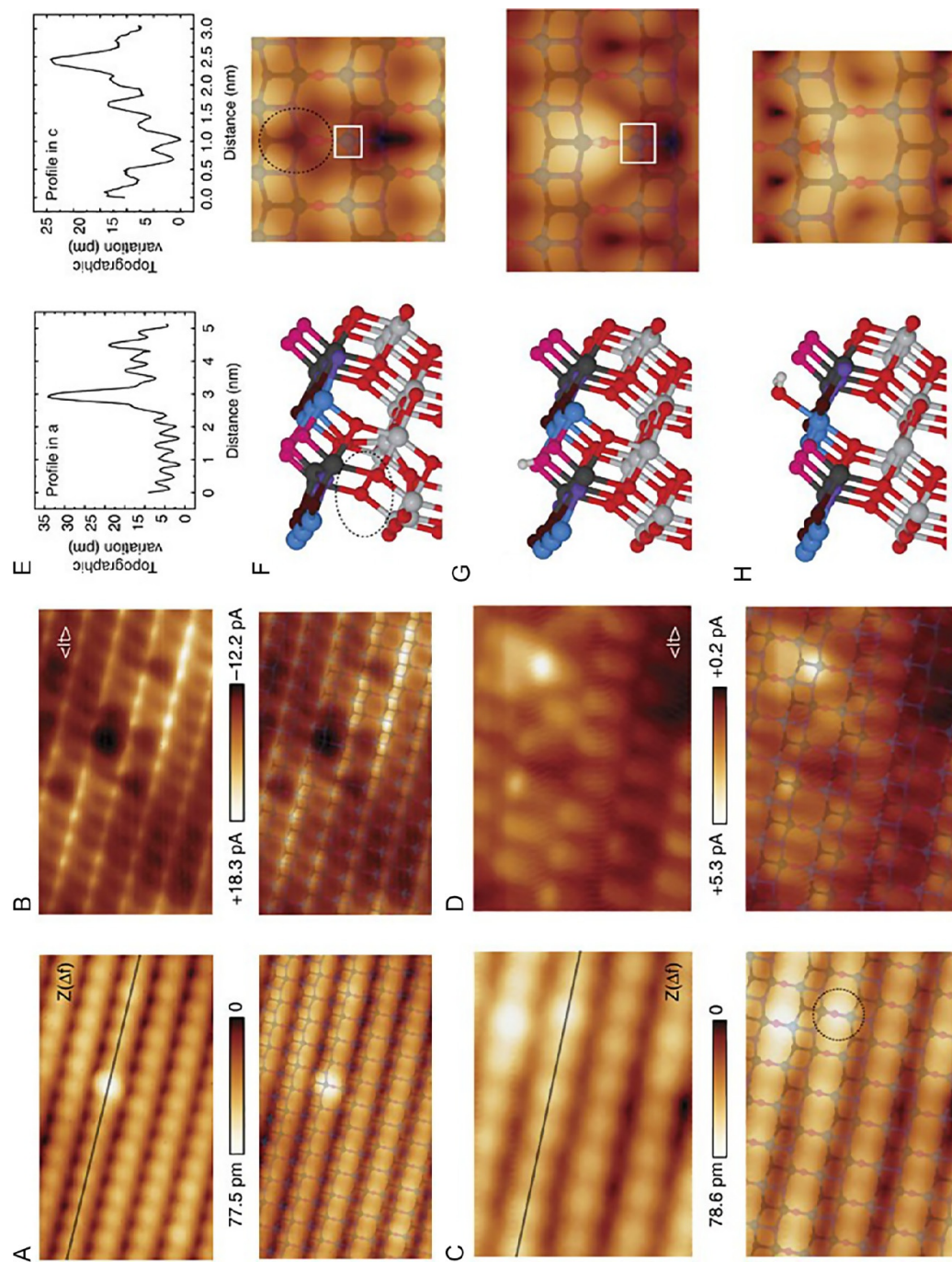
Schneider *et al.* found that  $\text{Ti}^{3+}$  centers show specific signals consistent to their anisotropic nature. For example, while performing EPR on the  $\text{TiO}_2$  having  $\text{Ti}^{3+}$  defects, the EPR showed an intense signal giving the isotropic value of ( $g_{iso}$ ) as 1.95 with slight asymmetry attributed to the presence of  $\text{Ti}^{3+}$  as shown in Fig. 13 (68).

Similarly, Ou *et al.* reported the detection of Ti<sup>3+</sup> defects using EPR. The *g*-values at 1.973 indicated Ti<sup>3+</sup> and 2.002 indicated oxygen vacancies in the lattice for lithium-reduced TiO<sub>2</sub>. EPR has become the chosen technique for characterization since XPS was insensitive in detecting Ti<sup>3+</sup> defects (36).

Baykara *et al.* studied the surface of rutile TiO<sub>2</sub> (110) using 3D-AFM coupled with STM to provide information on how individual defects of rutile TiO<sub>2</sub> (110) crystal facet affects the local density of electronic states (LDOS) and the work function with respect to tunneling current (57).

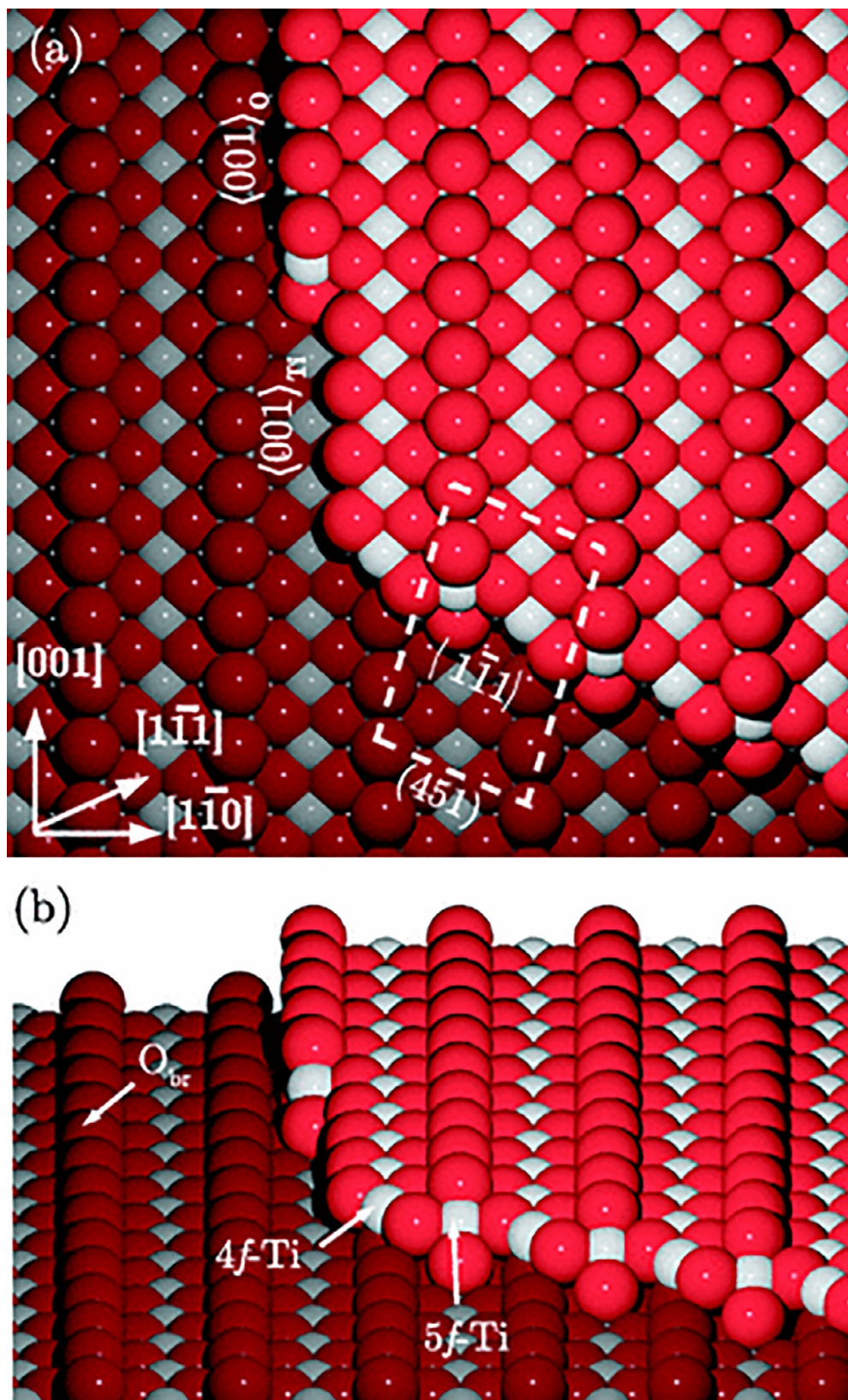
Stetsovych *et al.* also applied dynamic AFM coupled with STM to study anatase (101) along with characterization of defects (72). On the one hand, AFM was used in producing images of topmost oxygen atoms whereas on the other, the average tunneling current information provided by STM gives images of titanium atoms in the third atomic layer. These identifications were confirmed by the first principle simulation of the tip-surface interaction. Dominant characteristics of subsurface oxygen vacancy defects were extracted from extensive collection of AFM-STM images acquired over multiple measurement sessions to get extensive knowledge of oxygen vacancy defects in anatase (101) polymorph of TiO<sub>2</sub>. It was observed from the AFM-STM experiments that, subsurface oxygen vacancy sites bring changes to surface geometry by inducing structural deformations through subsurface bond distortions. This results in O<sub>2C</sub> site above the vacancy to get lifted by 28 pm while other surface atoms move downwards, an ideal characteristic of the presence of subsurface oxygen vacancy, thus supporting the AFM-STM image from Fig. 14A, which shows a bright wide feature in the topographic image located at a O<sub>2C</sub> site protruding ~28 pm from other O<sub>2C</sub> sites in defect free regions of the surface indicating a potential candidate for subsurface oxygen vacancy defect. This is further supported by the STM tunneling current <I<sub>t</sub>> signal which reduces under the protrusion seen in the AFM image (72).

Atomic step edges are the extended defects present on reduced TiO<sub>2</sub> surfaces. Atomic step edges play an important role in the reactivity of TiO<sub>2</sub> rutile surfaces. These constitute extremely stable oxygen vacancies. Martinez *et al.* states that even if the surface point defects of rutile become polluted (i.e., from environmental factors), point defects on the steps may take part in the catalytic cycle. Fig. 15. shows an image of atomic step edges on rutile TiO<sub>2</sub> (110) (73). However, atomic step edges and its related structural information is still a challenge, but with the help of AFM, some of these structural edges may be illuminated (73). Wen *et al.* studied step edges on



**Fig. 14** (A) Simultaneous AFM topographic, (B) averaged tunneling current images illustrating candidate for subsurface oxygen vacancy defect, (C and D) images of a defect candidate representing a surface hydroxyl group, (E) topographical signal along the line profiles in (A and C), (F) subsurface oxygen vacancy (0.8 V) (subsurface oxygen vacancy shown inside dotted circle), (G) surface hydroxyl group (0.6 V), (H) water molecule attached to surface (0.4 V). Dark areas in (F and G) appear near reduced  $Ti_{3+}^{3+}$  surface sites (white squares).





**Fig. 15** (A) Top and (B) tilted side view of rutile  $\text{TiO}_2$  (110) surface with bulk truncated (001) and (111) step edges (73).

rutile (110)–(1 × 1) and related oxygen vacancies along the step edges using AFM. Furthermore, a real-time measurement by combining AFM and STM were performed to show the presence of oxygen vacancies along the  $\langle 1-11 \rangle$  step edges (74).

A novel method, positron annihilation lifetime spectroscopy (PALS), for characterizing the oxygen vacancy produced in hydrogen modified TiO<sub>2</sub> was used by Jiang *et al.* Using the ORTEC-265 instrument with the PATFIT software, a fast-fast coincident phenomenon was measured at room temperature by analyzing the positron lifetime spectrum. This method proved to be quite sensitive and can be used in studying the size, type, and concentration of the intrinsic defects in semiconductors by determining the lifetime of the positrons. Positrons are preferential to low electron density areas, such as vacancy defects. Injecting positrons into the bulk materials of semiconductors leads to their annihilation in the presence of electrons releasing gamma rays which gives evidence about the lifetime of positrons (75). The shorter the lifetime of the positron means defect-free crystal with free annihilation of positron. On the other hand, longer positron lifetime means lower electron densities, and therefore, defects of larger sizes. The presence of defects (i.e., oxygen vacancies or monovacancies) in disordered systems results in elongated lifetimes due to difficult access for being annihilated. Usually, the positrons in the PALS method are annihilated due to thermalization as they enter the solid anatase particles. Whereas, in the method used by Jiang *et al.*, the positron could diffuse through the lattice reaching the grain boundaries, indicating a large number of boundary defects, before being annihilated. However, the drawback of this technique has been that it could not differentiate between bulk vs interfacial defects. It only confirmed the existence of interfacial defects by showing longer lifetimes of positron for the TiO<sub>2</sub> nanocrystal samples from TiO<sub>2</sub> (P25) (64, 75).

Chen *et al.* implemented a nondestructive approach in probing the spatial distribution of oxygen defects in and across the interfaces in transition metal oxide heterostructures. Gaining information not only on the concentration but also on the spatial distribution of defects near extended defects, such as grain boundaries, is important in indicating the level of catalytic activity. The combination of hard X-ray photoelectron spectroscopy and high resolution XRD was the nondestructive technique used by Chen *et al.* The photon energy and the photoelectron emission angles were varied to obtain information on the oxygen defect content buried in different depths across the interfaces. The change in the photon energy from the photoelectron spectroscopy gave information on the defects by analyzing the transition



metal valence state and the cation composition. Complementing hard X-ray photoelectron spectroscopy, XRD provided information on the lattice parameters which shows the changes in the oxygen defect concentration. Unique interface induced properties because of oxygen defects can be identified in layers of metal oxides through this technique (76).

The other kind of experimental characterization implemented in differentiating between defective and nondefective TiO<sub>2</sub> is photoelectrochemical characterization. Usually, the increase in photocurrent values generated from the photoelectrochemical characterization is the indication of the defective TiO<sub>2</sub>. Xu *et al.* successfully introduced Ti<sup>3+</sup> defects on the lattice distortions in anatase TiO<sub>2</sub> microspheres. The following were the observations made: (1) an increase in the photocurrent value from 1.78 for pristine TiO<sub>2</sub> anatase to 15.56  $\mu\text{A cm}^{-2}$  for lattice distorted TiO<sub>2</sub>, (2) an increase of photocurrent value from 1.78 to 53.78  $\mu\text{A cm}^{-2}$  with introduction of just Ti<sup>3+</sup> defects, and (3) in the presence of both, lattice distortions and Ti<sup>3+</sup> defects, the photocurrent value increased to 80  $\mu\text{A cm}^{-2}$ . The reason mentioned behind such an upsurge in the photocurrent value is because of the increase in separation of the charge carriers with increase in the defects in TiO<sub>2</sub> (39).

Fluorescence profiling can also be used in differentiating between defective and pristine TiO<sub>2</sub>, the lower the fluorescence emission intensity for excited electron-hole pair, the less severe the recombination rate and the indication of the presence of the defects. After implanting TiO<sub>2</sub> with defects by reducing TiO<sub>2</sub> with lithium, Ou *et al.* observed fluorescence decay profiles for both pristine and defective TiO<sub>2</sub>. The lifetime of charge carrier separation calculated for defective TiO<sub>2</sub> was 280 ps more than the pristine TiO<sub>2</sub>, which was 230 ps, indicating a longer separation of charge carriers due to the presence of defects (36). Typically, the fluorescence decay profile is used to tell the lifetime of photogenerated carriers. Additionally, the transportation and recombination kinetics of photogenerated electrons and holes can also be studied qualitatively through the fluorescence profile in solid steady state conditions.



## 8. Theoretical techniques: Density functional theory (DFT)

### 8.1 Brief overview of DFT as applied to TiO<sub>2</sub>

The most reliable computational quantum mechanical method implemented for explaining and predicting the properties of a molecular

system and extended materials, which has emerged over the past two decades, is Density Functional Theory (DFT) (70). The reliability of this computational method derives from the use of improved functional density approximations to predict several sets of molecular properties with better accuracy. Such strength makes DFT a valuable tool for the studies of molecular dynamics including those of metal oxides. As an example, the electronic structures of different polymorphs of  $\text{TiO}_2$  including the defect formation dynamics can be studied in detail using DFT with implementation of an appropriate density functional. The three main types of established DFT methods are (1) Local density approximation (LDA), (2) Gradient corrected (GC) or generalized gradient approximation (GGA), and (3) hybrid functionals. The selection of an appropriate density functional is of course tasks-dependent but one often finds both accuracy and computational efficiency to be the inevitable criteria. For example, hybrid density functionals, which are used in studying the electronic structure of semiconductor oxides, are popular due to its ability to treat the exchange-correlation interactions. Some of the hybrid functionals used are B3LYP, the Heyd, Scuseria, Erzerhof (HSE) functional or screened exchange functional (sX) (21,77). The codes implemented in these DFT computational studies are available in various software packages such as QUANTUM-EXPRESSO package, Vienne ab-initio simulation package or VASP.

These computational codes are applied to create  $\text{TiO}_2$  surfaces. The layers are termed as slabs constituting a finite number of atoms making a supercell of size (x, y, z). For example, Li *et al.* used slabs of 4  $\text{TiO}_2$  layers containing 144 atoms for the anatase (101) surface making a  $(2 \times 3)$  surface supercell (21). The formation energies of oxygen vacancies and the localized state associated with the oxygen vacancy is said to be sensitive to the supercell size. A smaller size of the supercell can yield an incorrect order of the formation energy of the oxygen vacancy. The screened exchange (SX) hybrid functional method using CASTEP plane wave pseudopotential code was used in determining the formation energies of oxygen vacancies at surface and subsurface sites of anatase (101), anatase (001), and rutile (110) surfaces. The anatase had the same oxygen vacancy formation energy in the bulk and on the surface. On the other hand, the rutile oxygen vacancy formation was found to be thermodynamically more preferred on the surface than in the bulk. The formation energy of an oxygen vacancy in  $\text{TiO}_2$  polymorphs is negative near the valence band minimum, indicating a spontaneous formation of an oxygen vacancy at a low Fermi level. In all the three  $\text{TiO}_2$  models, oxygen vacancies introduced mid-gap states near the conduction band lower limit (21).

A comprehensive computational description of oxygen vacancies in anatase (101) was provided by Ha and Alexandrova (78). The set of parameters considered were the spin polarization, localization of two electrons due to oxygen vacancies, and long-range interaction values such as van der Waal or London dispersion forces. The dependence of the formation of oxygen vacancies in anatase on these set of parameters was studied. Eq. (1) was used to calculate the oxygen formation energies.

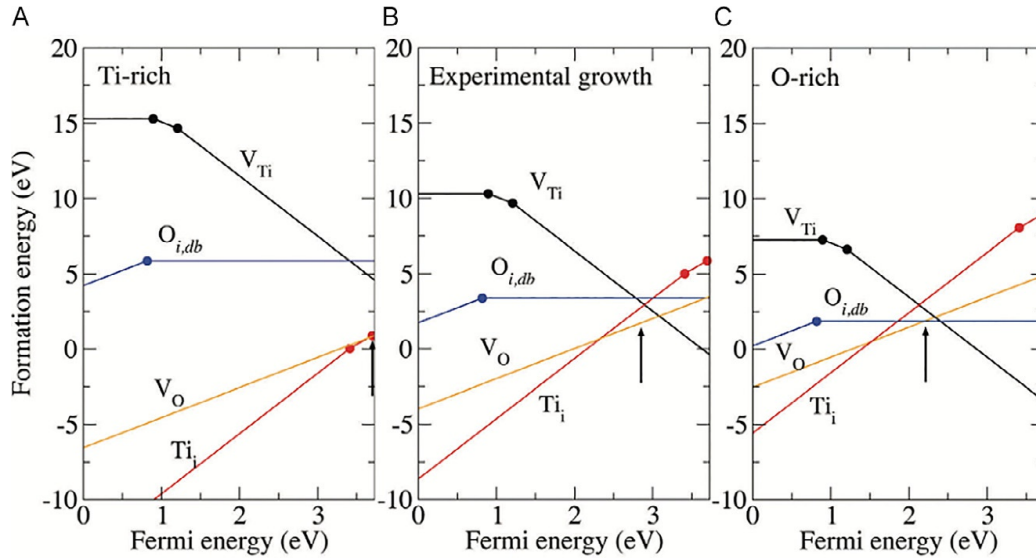
$$E_{\text{form}}(\text{V}_\text{o}) = E_{\text{tot}}(\text{def}) - E_{\text{tot}}(\text{no def}) + \frac{1}{2}\mu(\text{O}_2) \quad (1)$$

where,  $E_{\text{form}}(\text{V}_\text{o})$  represents formation energy of an oxygen vacancy,  $E_{\text{tot}}(\text{def})$  represents total energy of defective anatase,  $E_{\text{tot}}(\text{no def})$  represents stoichiometric anatase and the  $\mu(\text{O}_2)$  is the total energy of an oxygen molecule.

The anatase (101) surface, the most stable and dominant facet (>94%) of the anatase, was modeled. The subsurface oxygen vacancies were favored over the surface oxygen vacancies (using the PBE method) when magnetic properties of the anatase (101) were neglected. When magnetic properties (i.e., spin polarization) were considered, the calculations were performed using the methods DFT + PBE + D, DFT + PBE + U. Where, U is known as the Hubbard value input to account for the localization of two electrons due to an oxygen vacancy. The DFT + D is known as the Grimme's method accounting for dispersion forces. The Hubbard U corrections and dispersion forces are usually neglected as more preference is given to the sub-surface or bulk vacancies. However, when photocatalysis with electrochemical cells are considered, requiring information on the potential gradient, the corrections should be taken into account, considering surface oxygen vacancies as well. Two distinct oxygen vacancies related to their component reduced Ti<sup>3+</sup> states on the nonequivalent sites were identified using DFT + PBE + U (78).

Boochun *et al.* studied the energetics and electronic structures of the native defects such as oxygen and titanium vacancies and oxygen and titanium interstitials in anatase using Heyd-Scuseria-Ernzerhof (HSE06) hybrid functionals (79). Their DFT calculations were performed in a Vienne ab-initio simulation package (VASP) with the projector-augmented plane wave method. In this work, the electronic properties of native defects and their possibilities of formation in various conditions including titanium rich conditions, oxygen rich conditions, and experimental growth were examined. The defect formation energies were computed as:

$$E_f(D^q) = E_{\text{tot}}(D^q) - E_{\text{tot}}(\text{TiO}_2) - n_i\mu_i + q(\epsilon_f + E_V) \quad (2)$$



**Fig. 16** Defect formation energy as a function of Fermi energy in (A) Ti-rich condition, (B) experimental growth, and (C) Oxygen-rich. The up-pointing arrow is the Fermi level determined by charge neutrality condition at 550 °C (79).

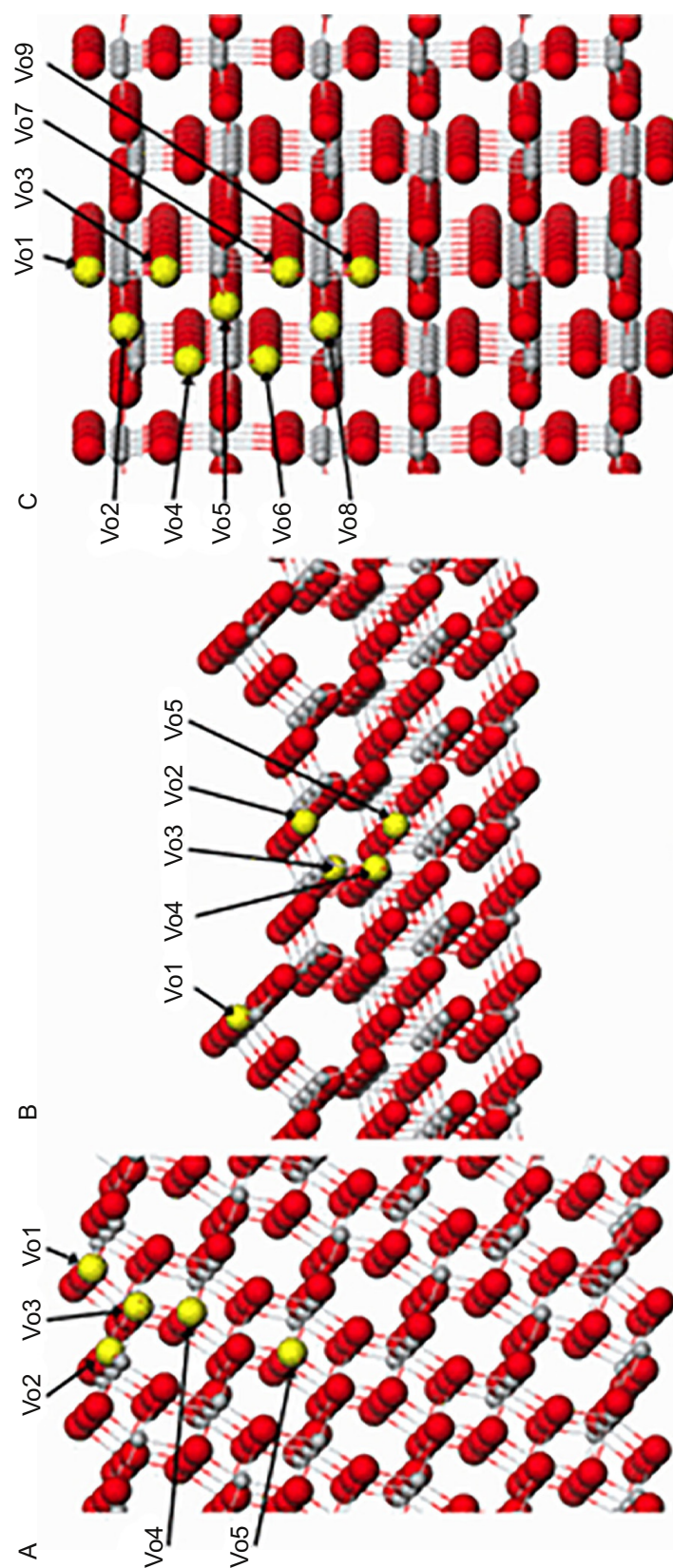
where  $E_{tot}(D^q)$  is the total energy of the supercell with defect,  $D$ , in the charge state,  $q$ .  $E_{tot}(\text{TiO}_2)$  is the total energy of the cell without defects, and  $n_i$  is the number of atoms of Ti or O named  $i$ .  $\epsilon_f$  is the Fermi energy and is the energy of the electron reservoir with respect to the valence band minimum (VBM). Fig. 16 displays some key findings about the dominant defects obtained by evaluating the formation energies as function of Fermi energy. As can be seen in titanium rich conditions, the  $\text{Ti}^{4+}$  has the lowest formation energies across a range of Fermi energies. At very high Fermi energies (near the conduction band minimum), the formation energy of oxygen vacancy is lower than the  $\text{Ti}^{4+}$ . On the other hand, Titanium vacancies ( $\text{V}_{\text{Ti}}^{4-}$ ) have formation energies much higher than other defects across the range of Fermi energies in Ti-rich conditions, whereas in oxygen rich conditions, the formation energy is lower. Their work concluded that the oxygen vacancy is the most dominant donor type defect, and therefore, a major source of electron carriers under any growth conditions. Also, titanium interstitials are stable in their quadruple charged state,  $\text{Ti}_i^{4+}$ . However, for the oxygen vacancy, the stability occurs in its doubly charged state. These results revealed that the oxygen vacancies and titanium interstitials act as donors and the titanium vacancies act as deep acceptors or donor compensating defects (79).

Despite decades of research progress, the modeling of TiO<sub>2</sub> using DFT methods have some difficulties: (1) The treatment of intermolecular interactions, including hydrogen-bonding, van der Waals interactions (dispersion) and other competing interactions, is yet to be completed. Such treatment is critical in understanding the electronic dynamics of TiO<sub>2</sub> whether it be on the surface or the subsurface. The newly refined DFT hybrid functionals, such as DFT-U-vdW (80), has attempted to overcome some of the above issues by including the Hubbard U term and van der Waals interactions as additive parameters. The success of this treatment, however, requires the use of unphysical parameters (i.e., Hubbard U) to find a match between DFT calculations and experiments. An advanced DFT hybrid functionals capable of fully describing all possible interactions is therefore needed to accurately model the dynamics TiO<sub>2</sub>. (2) The calculation of band-gap energy remains a challenge. The majority of DFT hybrid functionals can converge to the bandgap value of  $\sim 2.0$  eV (81), but this value is not close to the experimental values of 3.2 eV. Such a large discrepancy between DFT calculations and experiments suggests that the exact fundamental nature that governs the physical and chemical processes in TiO<sub>2</sub> polymorphs must be re-examined in great details.

## 8.2 DFT of TiO<sub>2</sub> without dopants

Surface and subsurface calculations were performed by Cheng and Selloni to determine oxygen vacancy energies of anatase and rutile phases (Fig. 17). Overall, results showed that oxygen vacancies are more likely to form within the subsurface than at the surface for anatase (Table 5). An interesting observation for the anatase (101) phase was that the oxygen vacancy at the site just below the surface was found to be unstable, and a surface oxygen, O<sub>2c</sub>, would spontaneously move to fill the vacancy, thus creating a V<sub>O1</sub> vacancy. In addition, a subsurface vacancy at V<sub>O4</sub> had a lower formation energy than V<sub>O1</sub>, a feature that held true no matter whether the slab contained 108 or 216 atoms. An analysis of the bond distances and bond angles indicated that there is more structural relaxation within the subsurface when an oxygen vacancy is formed compared to the surface, which is much more rigid. In comparison of the anatase planes, oxygen vacancies for (001) are larger than (101), and the surface region is thicker for (001) than (101). Meanwhile, surface bridging and subsurface bridging vacancies are most likely to form for rutile, which has characteristically lower oxygen vacancy formations than anatase (81).





**Fig. 17** Slab models (A) anatase (101) with six TiO<sub>2</sub> layers, (B) anatase (001) with a (1 × 4) slab, and (C) rutile (110) with six TiO<sub>2</sub> layers (gray = Ti, red = oxygen, and yellow = oxygen vacancy positions) [\(81\)](#).



**Table 5** Oxygen vacancy,  $V_O$ , formation energies (in eV) for surface and subsurface sites determined using slab sizes containing 216 (108), 153 (102), and 144 (96) atoms, respectively, for anatase (101), anatase (001), and rutile (110) (81).

Defect site	Anatase (101)	Anatase (001) (1 × 4)	Rutile (110)
$V_{O1}$	4.15 (4.25)	4.57 (4.72)	<b>3.68<sup>a</sup></b> (4.01)
$V_{O2}$	(5.40)	5.17 (5.52)	4.50 (4.56)
$V_{O3}$	(4.73)	4.29 (5.05)	<b>3.99</b> (4.23)
$V_{O4}$	<b>3.69</b> (4.03)	4.78 (5.08)	5.23 (5.22)
$V_{O5}$	<b>3.65</b>	<b>4.10</b> (4.34)	4.73 (4.83)
$V_{O6}$			5.28 (5.29)
$V_{O7}$			4.46
$V_{O8}$			4.67
$V_{O9}$			4.38

<sup>a</sup>For each surface, the defects with the lowest formation energies are in bold.

Portillo-Vélez *et al.* performed a DFT study, including the Density of States (DOS) using the Hubbard, U, correction, on the influence of oxygen vacancies for anatase (101) surface (82). The (101) plane was the focus of this study since it is the most thermodynamically stable plane, even though (100) and (010), and some (001), planes are also found within synthesized anatase. The oxygen formation energy,  $E_f^{\frac{1}{2}O_2}$ , was determined using Eq. (3).

$$E_f^{\frac{1}{2}O_2} = \frac{1}{N_{def}} \left[ E_{def} - E_{free} + \frac{1}{2} E_{O_2} \right] \quad (3)$$

Using the reaction:

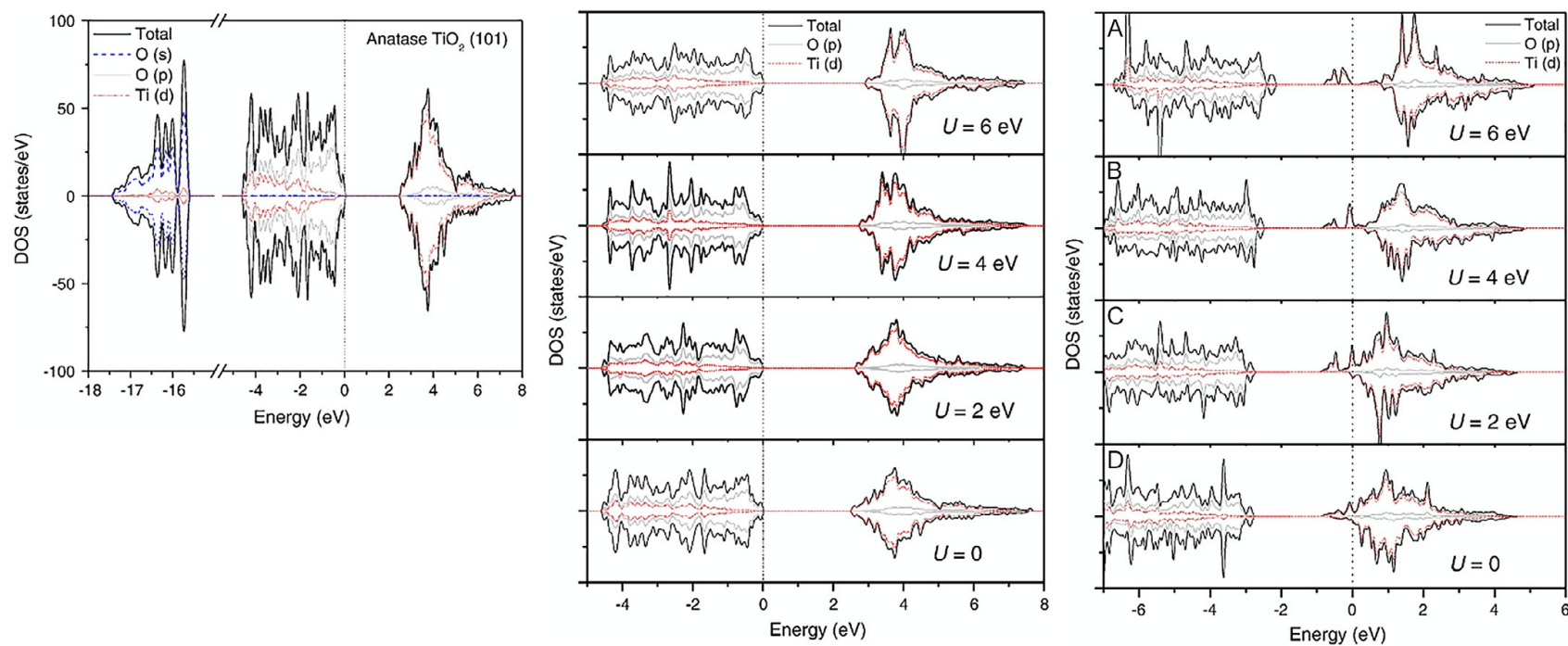


And, the energy of formation for the oxygen molecule was determined using Reaction (16) and Eq. (4).

$$2O \rightarrow O_2$$

$$E_{O_2} = E_{molecule} - 2E_{atom} \quad (4)$$

The effort by this team was to establish how the electronic structure of anatase is changed by oxygen vacancies and how these vacancies change the photocatalytic behavior of the material. As can be seen from Fig. 18 (left), there are three band regions ( $U=0$ ). The band around  $-17.5$  eV is mainly



**Fig. 18** DOS for anatase (101) (left) with no oxygen vacancies using the PBE approach, (center) with one oxygen vacancy using GGA+U, and (right) with four oxygen vacancies using GGA+U (82).

from O 2s orbitals. The valence band (−4.5 eV) derives mainly from O 2p orbitals, with some via hybridization from Ti d orbitals. The conduction band (+8 eV) is chiefly from Ti 3d orbital states. This evaluation leads to a bandgap of 2.59 eV, which is less than the experimentally measured value. To “nudge” the calculation toward the experimental value, the authors increased  $U$  ( $U=0, 2, 4$ , and  $6$ ). While  $U=6$  provides a bandgap energy more consistent with the experimentally determined value, it is not physically justified since the Ti d orbital states would be positioned in a false manner in the conduction band. Nonetheless, a value of  $U=6$  was used in evaluating the DOS when oxygen vacancies were included in the material.

By incorporating an oxygen vacancy (Fig. 18 (center)), localized  $\text{Ti}^{3+}$  states were found within the energy gap (located 2.08 eV above the valence band and 0.73 eV below the conduction band). These  $\text{Ti}^{3+}$  species are coordinated with four oxygen atoms, thus modifying the conduction property of the anatase (101) material. If a Hubbard value of 0 is used, the  $\text{Ti}^{3+}$  sites have delocalized states and are fused to the conduction band minimum. However, using  $U=6$ , the  $\text{Ti}^{3+}$  states are localized in the bandgap where the electron spin is polarized. The calculation then provides a physically meaningful solution. As the number of oxygen vacancies increase (Fig. 18 (right)), there is an increase in the number of reduced sites, and a shoulder appears at the conduction band minimum. These oxygen vacancies shift the Fermi level to the conduction band. The formation energy for the oxygen vacancies is presented in Table 6. With  $U=6$ , the formation energy is 5.26 eV, which is in close agreement to the experimental value. The positive value indicates an endothermic process; whereby, either an oxygen limited environment or heat treatment is needed to produce oxygen vacancies. These vacancies increase the density of electrons, which are chiefly on Ti atoms adjacent to the vacancies (82).

**Table 6** Oxygen vacancy formation energies for anatase (101) using GGA+ $U$  calculation method (82).

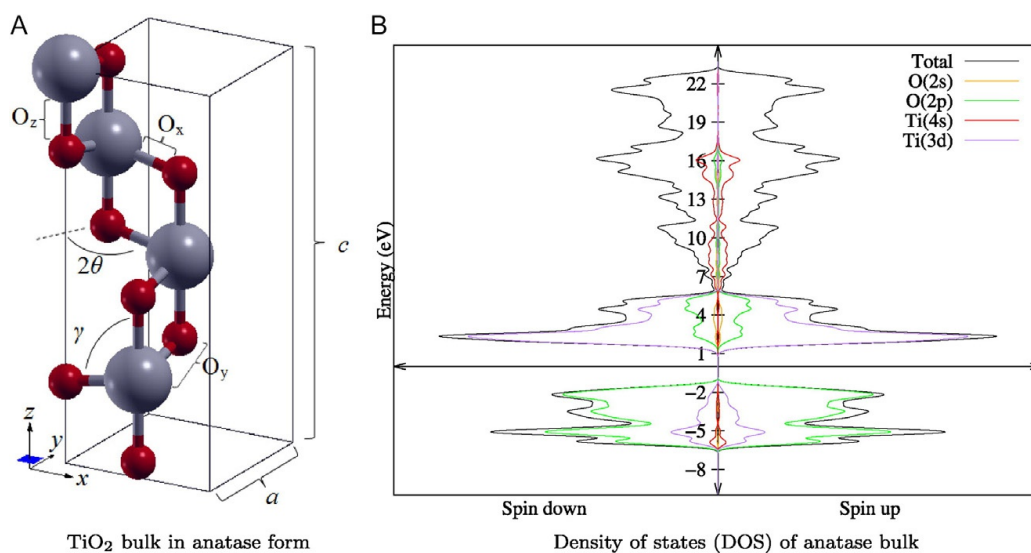
Oxygen vacancies	Formation energy of vacancies (eV)			
	$U=0$	$U=2$	$U=4$	$U=6$
1	6.49	6.65	6.04	5.26
2	6.58	6.60	5.95	5.14
3	6.83	6.68	6.06	5.28
4	6.52	6.63	5.92	5.06

The Hubbard and van der Waals contributions for anatase (001) surface were studied by Araujo-Lopez *et al.* (80). The authors performed the calculations using the Quantum ESPRESSO software package where the generalized-gradient approximation (GGA) and the Perdew, Burke, and Ernzerhof (PBE) correlations were used. The electronic wave was represented by a plane wave expansion, and the valence electrons were represented using the Vanderbilt ultra-soft pseudopotential. A value of  $U = 4.2$  eV was used as a suitable compromise between (1) the agreement of experimental and calculated bandgap energies and (2) the physical nature of the (001) surface when bond angles and interatomic distances are considered.

As shown in Fig. 19, the oxygen 2p orbitals for the bulk anatase were chiefly responsible for the greater contribution on the valence band. The Ti 3d orbitals also contributed, although to a lesser extent. The Ti 3d orbitals had a greater contribution to the conduction band compared to the O 2p orbitals.

### 8.3 DFT for surface modifications to $\text{TiO}_2$

To reduce the bandgap energy of  $\text{TiO}_2$ , surface modifications (i.e., doping with elements or synthesis of composition materials) have been tested with a wide array of elemental dopants and composite materials. Reducing the bandgap is believed to enhance the absorption of light, particularly in the visible spectrum, for increased photocatalytic activity. However, there



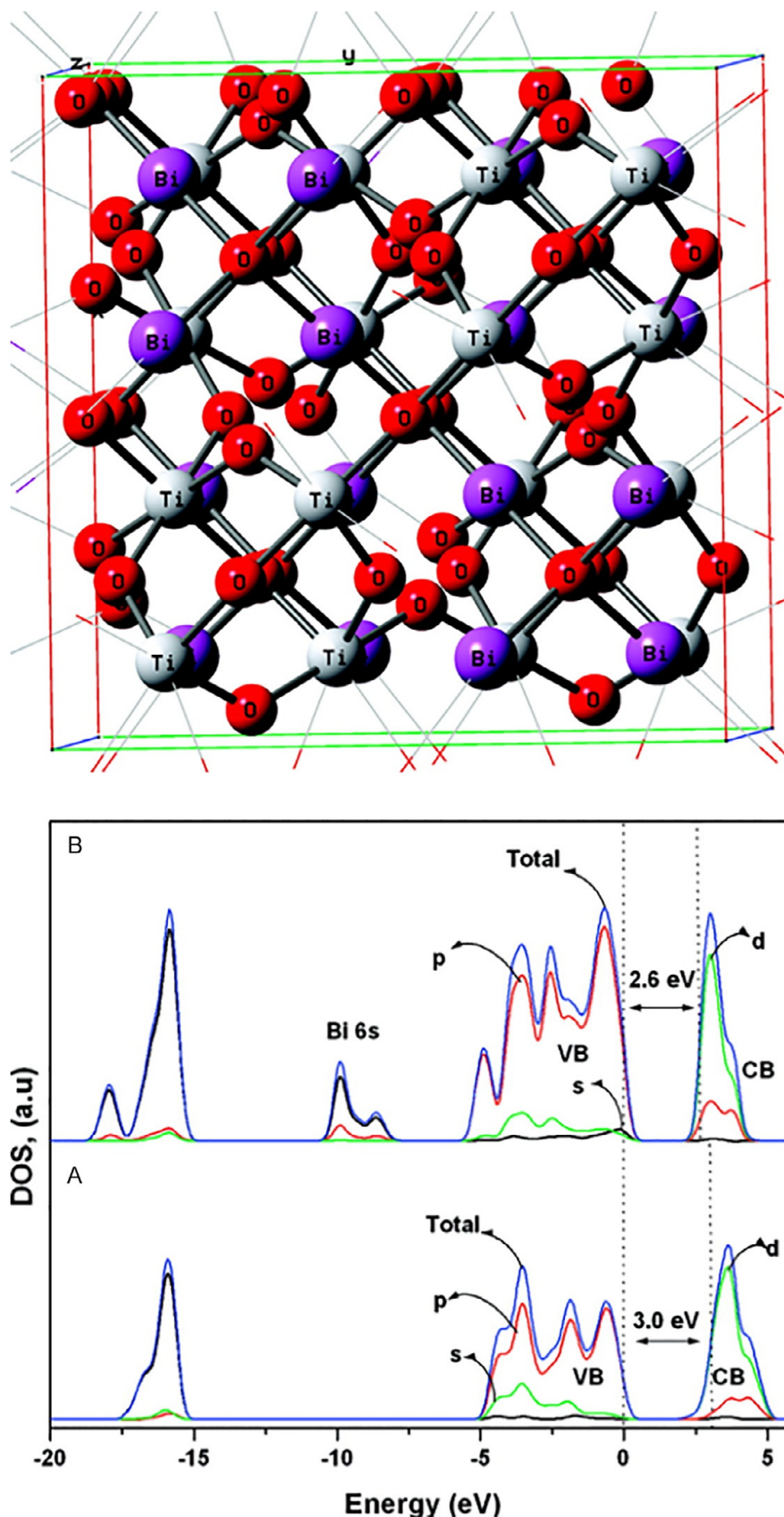
**Fig. 19** (A) Unit cell of anatase containing 12 atoms (gray = titania and red = oxygen). (B) Density of states for relaxed bulk anatase determined using DFT+ $U$ =vdW approach (80).

are sizable tradeoffs to consider. For instance, the recombination of holes with electrons as well as structural changes that occur when adding a dopant during the TiO<sub>2</sub> synthesis process. Addition of dopants can affect the stability of one plane (i.e., (001)) and destabilize another (i.e., (001)). The most relevant surface modifications toward the understanding of TiO<sub>2</sub> photocatalysis are examined here.

The pyrochlore geometry for bismuth titanate (Bi<sub>2</sub>Ti<sub>2</sub>O<sub>7</sub>) was studied using DFT techniques (83). Pyrochlore geometry offers manipulation of the electron/hole mobility when different elements are inserted into the structure. The DFT evaluation was performed using CASTEP (Materials Studio by Accelrys) with an ultrasoft pseudopotential plane wave (300 eV kinetic energy cutoff). The partial DOS (Fig. 20) shows a 0.4 eV reduction in the bandgap for bismuth titanate compared to TiO<sub>2</sub>. This reduced bandgap is believed to be a combination from the 6 s bismuth orbital and the oxygen 2p orbital. There is an interband caused by the Bi 6 s that shifts the valence band toward the conduction band, leading to activation by visible light. Substitution experiments were performed using transition metal (Fe, Cr, Mn, and Ni) and nonmetals (N, S, and C), using the general formula Bi<sub>2</sub>Ti<sub>1-x</sub>M<sub>x</sub>O<sub>7</sub> (where M = substituted element) to determine effect on catalytic activity. Substitution of the transition metals indicated an increase in photocatalytic activity. These 3d elements, when substituted at the Ti sites, permit tuning for visible light activation and interband state locations since these elements form octahedral crystal structures. The d-orbitals form split states (*t*<sub>2g</sub> and *e*<sub>g</sub>). By increasing the number 3d electrons, *t*<sub>2g</sub> and *e*<sub>g</sub> state shift to lower energy, making the chemical potential of the d-electrons lower and closer to the p-orbital. 3d elements also offer an advantage over larger radii elements (i.e., rare earth elements) that tend to increase the bandgap energy (i.e., decreasing photocatalytic activity).

A thorough DFT study was conducted by Li, *et al.* for the adsorption of Au nanoparticles onto anatase (101) and brookite (210) surfaces (84). Few studies have been performed using brookite due to its thermodynamic instability. With the discovery of better processing methods, however, thermodynamically stable brookite can be synthesized, giving way for more fundamental studies. Li and coworkers examined the mechanisms and changes in the two TiO<sub>2</sub> polymorphs when 1–8 gold atoms were adsorbed. On a stoichiometric surface (i.e., no oxygen vacancies), a single Au atom adsorbed to the brookite (210) surface via mainly to the Ti<sub>5c</sub> with weak interactions with the O<sub>2c</sub> that is nearby. For anatase (101), the binding mechanism is bridged between the O<sub>2c</sub> and Ti<sub>5c</sub> atoms. When oxygen vacancies were





**Fig. 20** (top) Crystal structure of simulated bismuth titanate ( $\text{Bi}_2\text{Ti}_2\text{O}_7$ ) (bottom) Total density of States of (A)  $\text{TiO}_2$  and (B) BTO pyrochlore. BTO displays contribution from 6 s orbital of Bi in valence band (83).



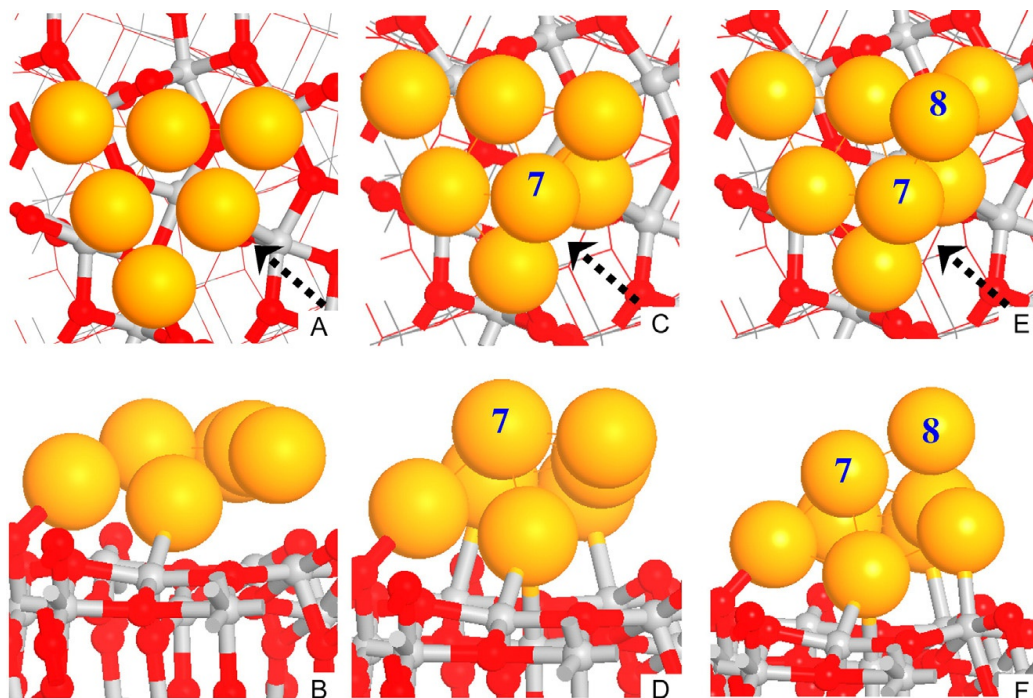
**Table 7** Adsorption energies and bond lengths for gold nanoparticles on anatase and brookite surfaces (84).

	Adsorption energy (eV)	Ti <sub>5c</sub> bond length (Å)	Ti <sub>4c</sub> bond length (Å)	O <sub>2c</sub> bond length (Å)
<i>Anatase (101)</i>				
Stoichiometric	0.45	2.795	–	2.221
Reduced	3.22	2.838	2.558	–
<i>Brookite (210)</i>				
Stoichiometric	0.62	2.707	–	–
Reduced	2.98	2.899	2.558	–

considered (i.e., removal of the O<sub>2c</sub> atom), there is a structural relaxation of the Ti<sub>6c</sub> and the Ti<sub>5c</sub> atoms on both the anatase (101) and brookite (210) surfaces. For both materials, the adsorption of a single Au atom takes place on the Ti<sub>5c</sub> and Ti<sub>4c</sub> atoms (i.e., taking the place of the missing oxygen). The differences mainly being adsorption energies and relative bond lengths (Table 7). The adsorption energies are considerable higher for the reduced (i.e., oxygen vacancy) surfaces. In addition, anatase, compared to brookite, has a higher adsorption energy, which the authors attributed to the structural relaxation of the brookite.

Gold nanoclusters were studied in more detail on the brookite (210) surface with oxygen vacancy. The second Au atom attaches to the first and a neighboring Ti<sub>5c</sub> atom. For a third Au atom, a “standing” triangular structure emerges. Addition of 4, 5, and 6 Au atoms forms an inclined quadrilateral structure, a trapezoidal structure, and a “lying” triangular structure, respectively. The addition of 7 and 8 gold atoms results in a true 3D configuration (Fig. 21). Overall, gold nanostructures appeared as extended structures on anatase, while dispersion of the clusters were favored for brookite.

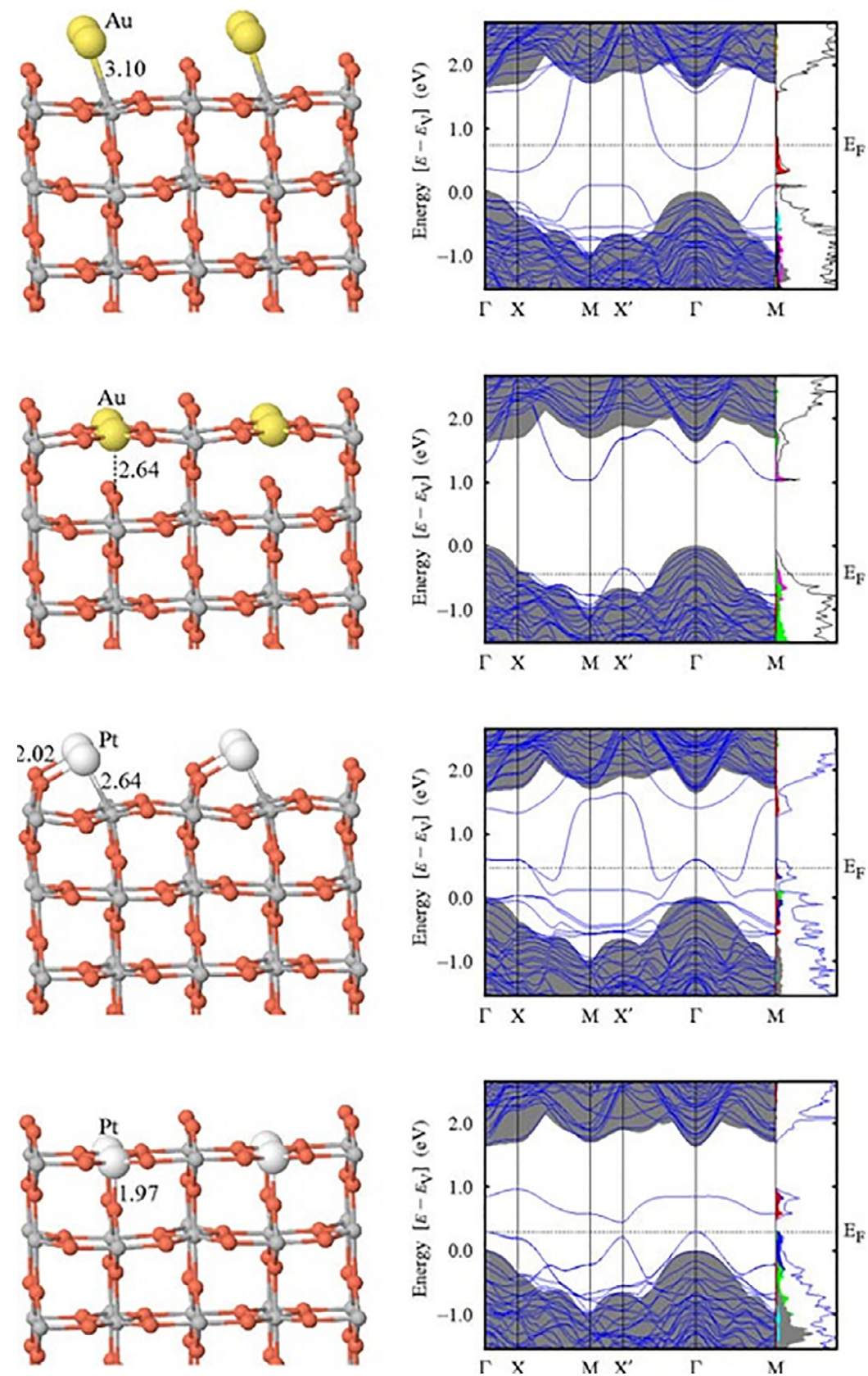
The reduced brookite (210) surface containing gold nanoclusters (Au<sub>6–8</sub>) was also studied for its ability to catalyze the CO oxidation reaction. The adsorption of molecular oxygen easily adsorbs to Au<sub>8</sub> cluster (0.64 eV) and to a slightly lesser extent on Au<sub>6</sub> and Au<sub>7</sub> sites (0.4 eV for both). These findings imply that O<sub>2</sub> adsorption favors low coordination sites. CO, on the other hand, favors a protruding Au site, so much so that Au atoms can move from a flat, 2D-like structure into a 3D structure. These key findings illustrate the importance of the specific TiO<sub>2</sub> surface for catalytic and photocatalytic reactions (84).



**Fig. 21** Calculated structures for  $\text{Au}_{6-8}$  nanostructures on brookite (210) surface. Top view (A, C, and E) and side view (B, D, and F) (84).

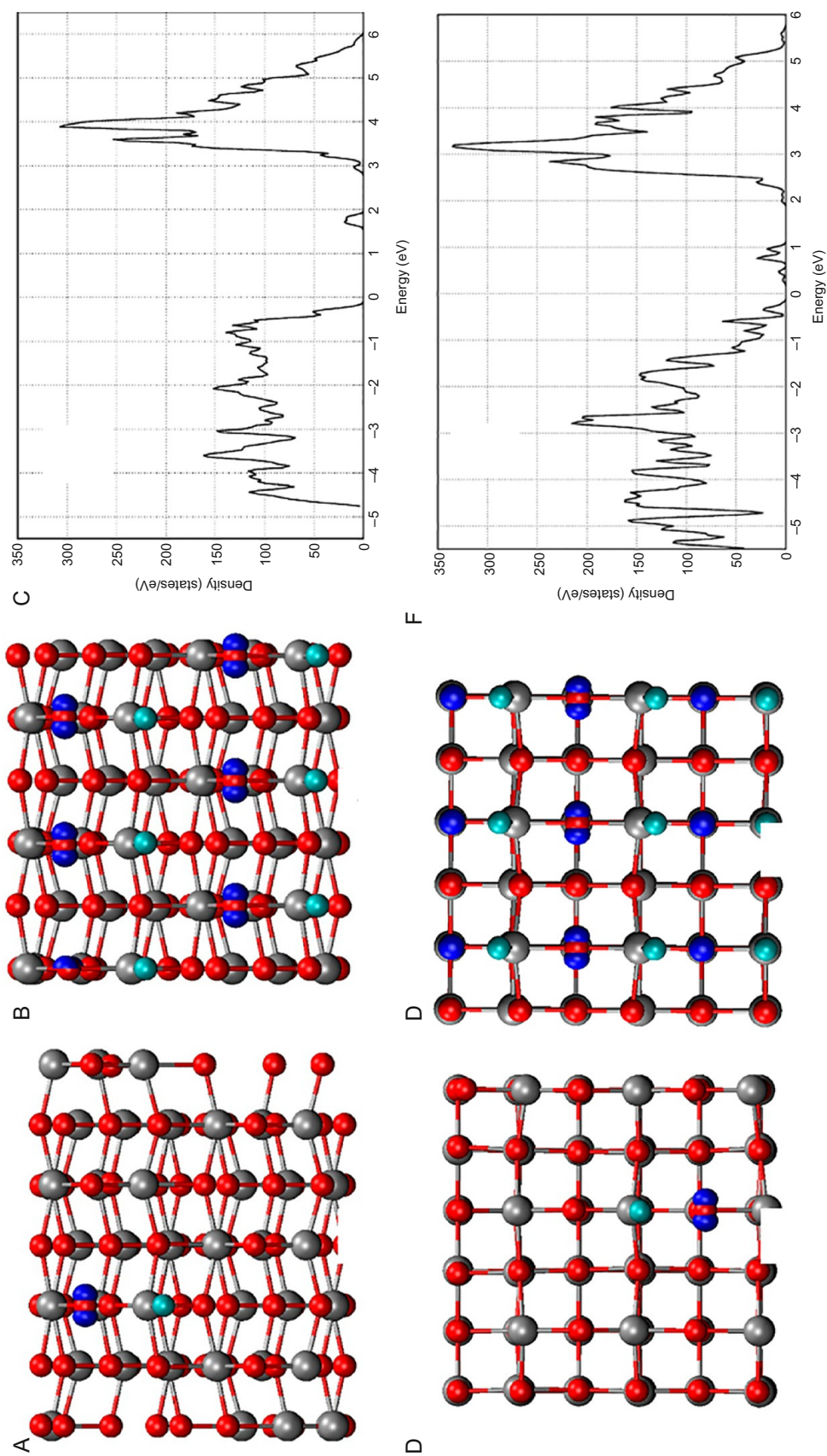
Mete and coworkers performed DFT calculations for Au and Pt incorporated into Rutile (110). At one monolayer coverage, gold dimers form parallel to the oxygen rows, and the interatomic distances are somewhat longer than the gold dimer length, indicating strong Au–Au coordination (Fig. 22). However, substituting Au for  $\text{Ti}_{5c}$  causes substantial distortion of the surface morphology. This distortion leads to an increased bonding distance between the  $\text{Ti}_{5c}$  and the oxygen below it from 1.83 to 2.64 Å. Platinum, on the other hand, distorts the surface much less than gold. Pt leads to a fourfold coordination with basal oxygens, causing a gap state within the valence band. The Fermi energy is increased by 0.33 eV compared to that of a clean surface. At concentrations less than one monolayer, Au and Pt atoms are adsorbed within the interstitial lattice sites. Increased catalytic behavior within the visible spectrum is predicted due to the narrowing of the bandgap. Differing concentrations of Pt could be used to tune to a specific wavelength (85).

Adsorption of F onto the anatase (101) surface (always interacting with the fivefold coordinated Ti ( $\text{Ti}_{5f}$ ) surface cations) can be seen in Fig. 23A and B (86). The electronegativity of the F oxidizes anatase O anions. Formally,  $\text{O}^{2-}$  is oxidized to  $\text{O}^-$  and F becomes  $\text{F}^-$ . The total DOS for the (101) surface (Fig. 23C) exhibits a peak within the bandgap that is 1 eV below



**Fig. 22** (left) Relaxed geometries  $\text{Au/TiO}_2$  and  $\text{Pt/TiO}_2$  (110)-(1  $\times$  1). (right) Corresponding bandgap states and bulk projected band structures (85).





**Fig. 23** Surface coverage with Fluorine for anatase (A) (101) with 17% coverage, (B) (101) 100% coverage, (C) total DOS of (101) with all  $\text{Ti}_{5f}$  cations covered by F, (D) (001) with 11% coverage, (E) (001) with 100% coverage, and (F) total DOS of (001) with all  $\text{Ti}_{5f}$  cations covered by F (gray = Ti, red = O, and light green = F atoms) (86).

the conduction band, which is largely due to the oxidation of the O anion. The (001) surface shows unpaired electrons localized in one of the oxygen atoms of the TiO<sub>2</sub> (Fig. 23D), a feature also displayed at 100% coverage (Fig. 23E). There is also a peak within the bandgap as with the (101) case; however, the total DOS is broader since there are different types of oxygen atoms on the surface. A surprising conclusion of this work was that the fluorine-doped (001) surface was more stable than the fluorine-doped (101) surface, which is opposite of the clean TiO<sub>2</sub> surfaces.

The doping of rutile with either carbon or nitrogen atoms was investigated where the C/N atoms were either substituted for an oxygen or occupied interstitial positions (87). When a single C is substituted for an O, a 2  $\mu_B$ /unit cell magnetic moment is formed. The substitution leads to two holes in the system, and a complete band becomes unoccupied. Substituting a single N atom creates only one hole, and consequently, a magnetic moment half of the C-substituted system. Doping with either C or N increases atomic distances within the crystal structure. Nitrogen, being more electronegative, interacts more with the TiO<sub>2</sub>, in particular its oxygen neighbors. Substituting two C or N atoms shows a doubling of the magnetic moment for each system. There is a slight increase in the cell volume but not nearly as much as that seen with the one atom substitution scenario. The changes in bandgap energies for the single substitution can be found in Table 8, and those for two C/N atom substitutions can be found in Table 9. When placed within the interstitials, neither C nor N yielded any magnetic moment; however, the electronic structures were similar to C/N-doped experiments.

N-doping of the rutile does not lead to mid-band energy states, which is seen as a positive. Mid-band energy states behave as electron-hole traps and

**Table 8** DFT calculated bandgap energies for rutile with singular C/N atom doping (87).

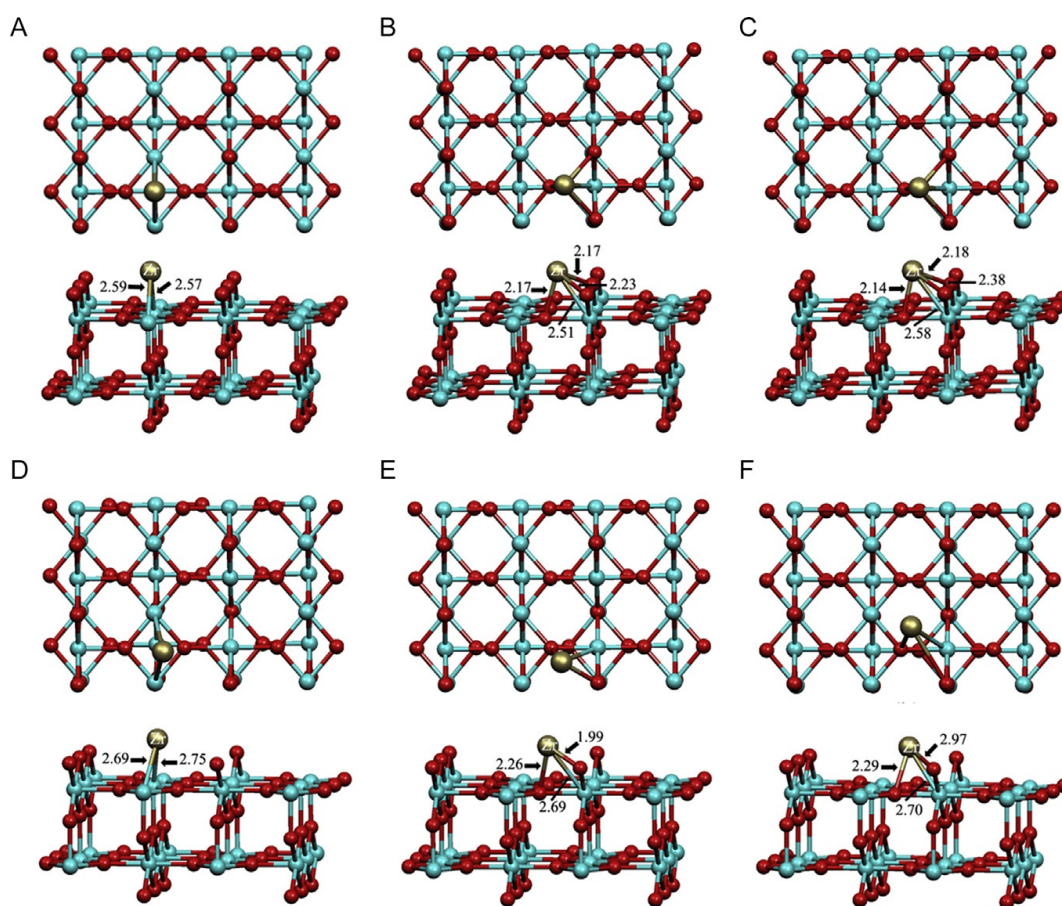
Bandgap (eV)	O	C	N
Spin up bandgap	3.24	2.20	3.20
Spin down bandgap	3.24	2.06	2.60

**Table 9** DFT calculated bandgap energies for rutile with two C/N atom doping (87).

Bandgap (eV)	C (1,2)	C (1,3)	N (1,2)	N (1,3)
Spin up bandgap	1.40	1.90	2.45	3.16
Spin down bandgap	1.40	1.90	2.45	2.33

recombination centers, reducing the efficiency of the photocatalyst. The authors point out that the key to maximizing efficiency is to reduce the bandgap without introducing mid-gap energy states. From these calculations, doping with N atoms should lead to increased efficiency for a rutile photocatalyst. C-atom substitution, however, leads to mid-gap energy states and is projected to be a less efficient photocatalyst.

Various configurations of Zr doping on a Rutile (110) surface with and without oxygen vacancies were studied using DFT (88). Of the configurations studied, Zr-TiO<sub>2</sub>-2 and Zr-(TiO<sub>2</sub> + V<sub>O</sub>)-2 were found to be the most stable (please see Fig. 24 for configuration identification). The adsorption of Zr onto the surface had binding energies of  $-3.36$  and  $-3.26$  eV for the Zr-TiO<sub>2</sub>-2 and Zr-(TiO<sub>2</sub> + V<sub>O</sub>)-2, respectively. Bandgap energies are presented in Table 10. In addition, adsorption of H<sub>2</sub> molecule (for one



**Fig. 24** Zirconium doped structures for rutile (110) surface without oxygen defect (A) Zr-TiO<sub>2</sub>-1, (B) Zr-TiO<sub>2</sub>-2, (C) Zr-TiO<sub>2</sub>-3, on the oxygen vacancy defect (D) Zr-(TiO<sub>2</sub> + V<sub>O</sub>)-1, (E) Zr-(TiO<sub>2</sub> + V<sub>O</sub>)-2, and (F) Zr-(TiO<sub>2</sub> + V<sub>O</sub>)-3 (88).



**Table 10** DFT calculated bandgap energies and adsorption energies for 1 and 2 hydrogen molecular adsorption for rutile (110) with Zr doping (please refer to Fig. 24 for position location coding) (88).

Surface	Bandgap (eV)	$\Delta E_{\text{ads}}$ (1H <sub>2</sub> )	$\Delta E_{\text{ads}}$ (2H <sub>2</sub> )
Clean Rutile (110)	2.68		
Zr-TiO <sub>2</sub> -1	1.78		
Zr-TiO <sub>2</sub> -2	0.80	−1.43	−1.90
Zr-TiO <sub>2</sub> -3	0.87		
Clean (TiO <sub>2</sub> + V <sub>o</sub> )	1.35		
Zr-(TiO <sub>2</sub> + V <sub>o</sub> )-1	1.08		
Zr-(TiO <sub>2</sub> + V <sub>o</sub> )-2	1.62	−1.45	−2.55
Zr-(TiO <sub>2</sub> + V <sub>o</sub> )-3	1.98		

and two molecules adsorbed) was also studied on the most stable structures. The adsorption of the second H<sub>2</sub> molecule was found to be much stronger than the first.

Composite materials offer a compelling compromise between materials with mid-bandgap energy states, exhibiting short electron–hole separation times, and charge transferring materials. Zhang *et al.* investigated the structure of a composite material containing anatase, SnS<sub>2</sub>, and reduced graphene oxide (RGO) (89). The SnS<sub>2</sub> forms a hexagonal platelet (Fig. 25 (left)) with edges that are metallic (electron deficient) and sulfur. The Ti–OH constituents are coupled with the smooth edges of the RGO and are electron donating. Fig. 25 (right) shows that the two Ti–OH oxygen atoms coordinate with the SnS<sub>2</sub> metallic edges. The authors describe the enhancement of the separation of photogenerated electron/hole pairs, a necessity in photocatalysis, occurs at the interface between TiO<sub>2</sub>/SnS<sub>2</sub> and RGO, which are connected by strong hydrogen bonds.

DFT modeling of CuO<sub>x</sub> nanocluster adsorption on rutile (110) and anatase (101) surfaces show an upshift in the valence band, and thus, a red shift in the bandgap energy (90). Different stoichiometries (Cu<sub>4</sub>O<sub>4</sub>, Cu<sub>4</sub>O<sub>3</sub>, Cu<sub>10</sub>O<sub>10</sub>, and Cu<sub>10</sub>O<sub>8</sub>) were tested, yielding no significant differences in the bandgap narrowing. There was, however, strong adsorption of the copper oxide nanoclusters to both surfaces (−7.45 eV for rutile and −3.27/−2.41 Cu<sub>4</sub>O<sub>4</sub>/Cu<sub>10</sub>O<sub>10</sub> for anatase). On reduced TiO<sub>2</sub> surfaces (i.e., containing oxygen vacancies), two Cu<sup>+</sup> cations are formed for each O vacancy.

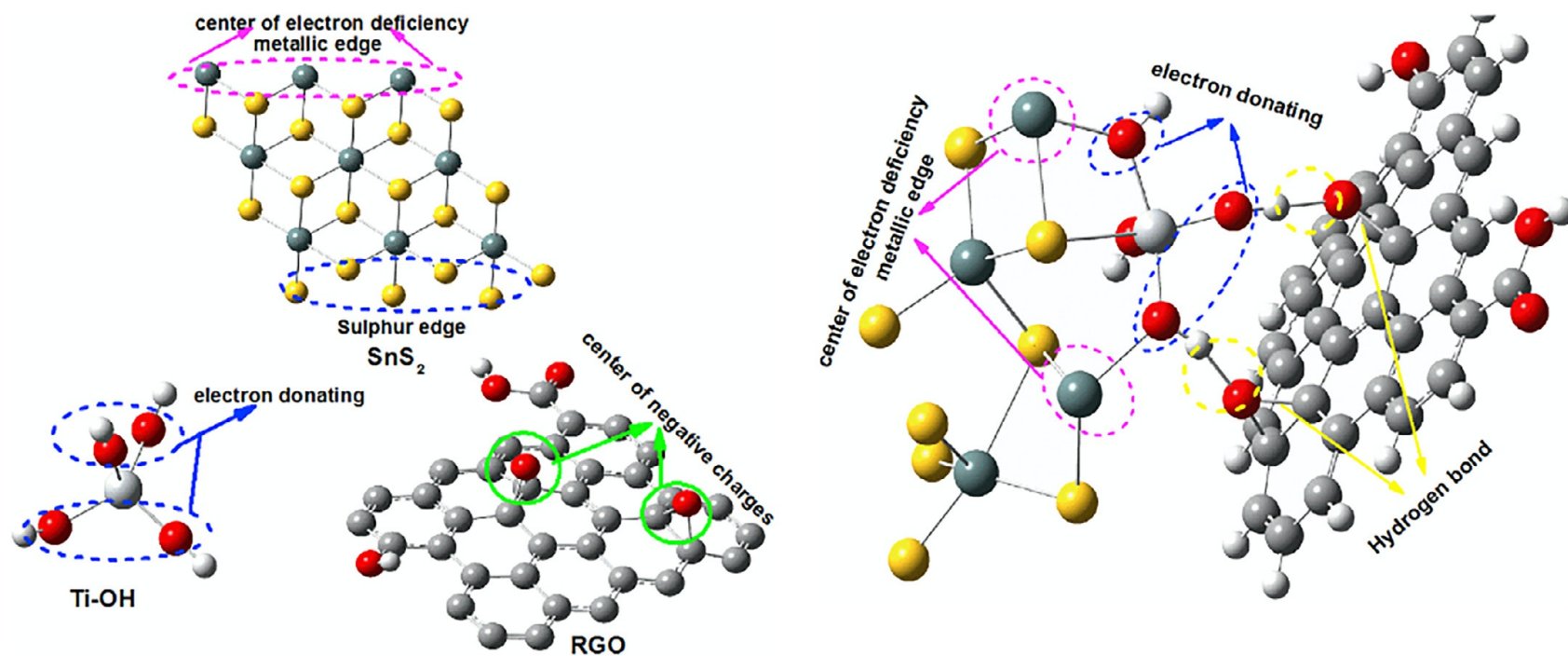


Fig. 25 Proposed structure of  $\text{SnS}_2$ ,  $\text{Ti-OH}$  of  $\text{TiO}_2$ , and RGO (gray = Sn, red = O, silver = Ti, yellow = S, silver-gray = H, light gray = C) (89).

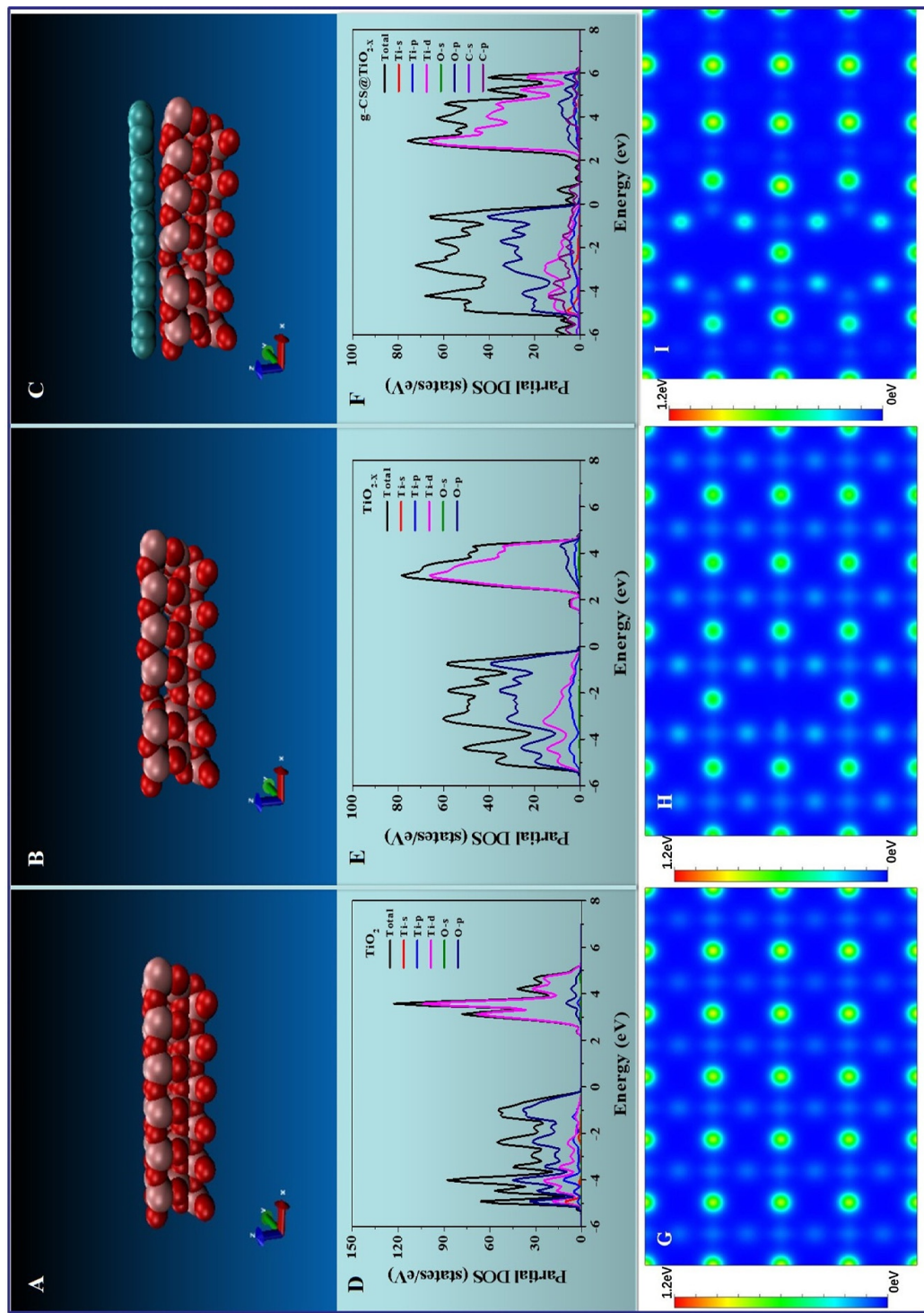
The DOS and Partial Density of States (DOS) were evaluated for TiO<sub>2</sub> (i.e., no Ti<sup>3+</sup>), TiO<sub>2-x</sub> (i.e., induced oxygen vacancies forming Ti<sup>3+</sup>), and g-CS@TiO<sub>2-x</sub> (i.e., graphitic carbon and Titania composites) (91). Using the Vienna Ab-Initio Simulation Package (VASP), electron-ion interactions were determined using the project augmented wave (PAW) method. The PDOS results showed for TiO<sub>2</sub> that the primary valence states came from O 2p orbitals and conduction states derived from Ti 3d orbitals. When lattice oxygens were removed, forming Ti<sup>3+</sup>, a small conduction band minimum was formed along with a lower bandgap energy (Fig. 26). This small energy level was formed from Ti 3d orbitals. Introducing a layer of graphite-like carbon spheres (g-CS) to the TiO<sub>2-x</sub>, on the other hand, established mid-gap states between the valence band minimum and the conduction band minimum, which can further reduce the bandgap. When irradiated with visible light, excited electrons easily transfer from the VB of TiO<sub>2-x</sub> to these mid-gap levels or from a mid-gap level to the CB of the TiO<sub>2-x</sub>. Electron-hole recombinations are impeded since movement from the CB to the VB is more difficult. Furthermore, new C-O bonds could be formed from the strong interactions arising from unpaired  $\pi$ -electrons with free electrons on the TiO<sub>2-x</sub> surface.

#### 8.4 Interactions (adsorption/reaction) with TiO<sub>2</sub> and organic and inorganic molecules

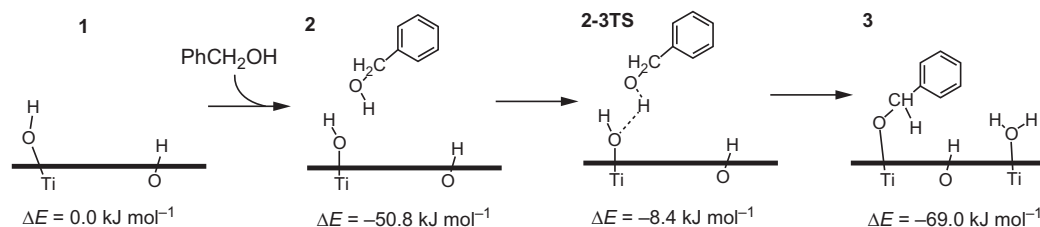
The behavior of a surface's interactions with reactionary molecules (i.e., CO, O<sub>2</sub>, formaldehyde, etc.) is necessary to understand specific reaction mechanisms, adsorption/desorption energies, and potential poisoning effects. For instance, Wang *et al.* demonstrated through DFT calculations that there is a synergistic effect of an oxygen vacancy and Pd doped on anatase (101) surface for the adsorption of formaldehyde. The oxygen atom of the formaldehyde occupies the oxygen vacancy, while the carbon atom binds to the Pd (91,92).

Likewise, CO oxidation on rutile (110)/Co<sub>2</sub>B<sub>2</sub> alloy. CO preferentially binds to the CO<sub>2</sub> sites, which also promotes the linear adsorption of O<sub>2</sub> molecules. Since adsorption of both CO and O<sub>2</sub> occurred on the CO<sub>2</sub> site via the Langmuir-Hinshelwood mechanism, this catalyst is believed to have good activity for CO oxidation (93). The specific character of CO<sub>2</sub> sites was not very well described by the authors, and no further description is provided here.

The selective oxidation of benzyl alcohol to form benzaldehyde was investigated using DFT (Fig. 27). Benzyl alcohol interacted with



**Fig. 26** DFT models, partial density of states, and charge difference for  $\text{TiO}_2$  (A, D, G),  $\text{TiO}_{2-x}$  (B, E, H), and  $\text{g-CS@TiO}_{2-x}$  (C, F, I). (For A, B, and C, red = oxygen atoms, purple = titanium atoms, and turquoise = carbon atoms) (91).



**Fig. 27** Interaction of benzyl alcohol with TiO<sub>2</sub> surface (94).

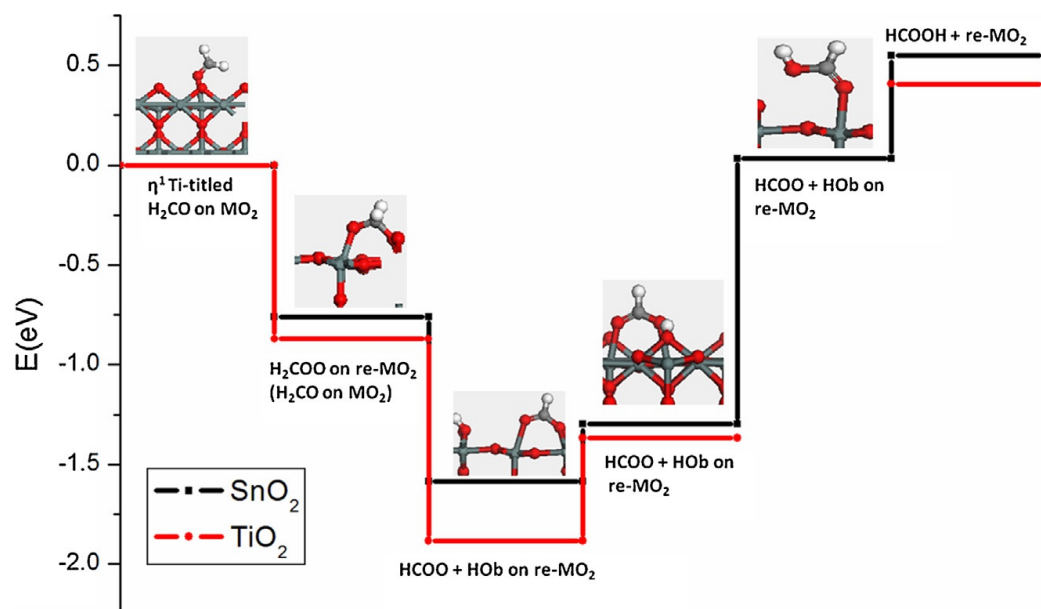
[Ti]-OH group on the anatase surface, forming an alkoxide species. Irradiating TiO<sub>2</sub> with visible light attributed to electronic transition from the donor levels that were created by the alkoxide species to the conduction band minimum of the anatase catalyst (94).

The adsorption of formaldehyde, formic acid, and formate were studied for rutile (110) and SnO<sub>2</sub> by Tang and coworkers (95). SnO<sub>2</sub> exhibited stronger binding energies for the three adsorbates on surfaces without oxygen vacancies, which was reversed on surface with oxygen vacancies. The rutile was deemed to have higher activity for the reaction of formaldehyde oxidation to formic acid than SnO<sub>2</sub>. The key intermediate being a V<sub>o</sub>-bidentate formate species. The potential energy diagram is presented in Fig. 28.

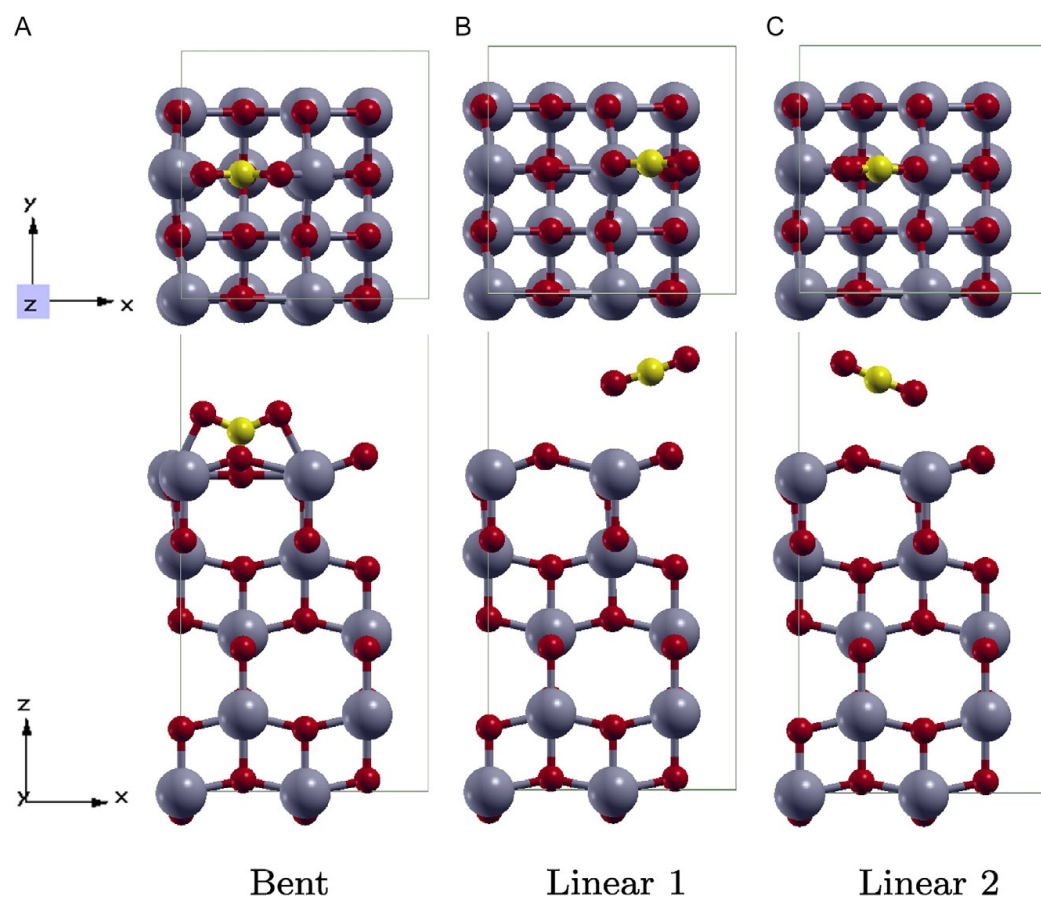
When considering the adsorption of CO<sub>2</sub> to the anatase (001) surface, the three scenarios considered were (1) CO<sub>2</sub> aligned with x-axis, (2) CO<sub>2</sub> aligned with y-axis, and (3) CO<sub>2</sub> perpendicular to the surface (80). When only the DFT + U calculations were performed, only two of the structures showed to be stable. However, when the van der Waals dispersion forces were considered, all three structures were shown to be stable, which were also shown experimentally. The most stable adsorbate/adsorbent system was that where the CO<sub>2</sub> was bent. The C atom was bound with the O<sub>2</sub>C, and the oxygen atoms were bound to two Ti<sub>5</sub>C atoms (Fig. 29A). In addition, the two linear scenarios (Fig. 29A and C) show CO<sub>2</sub> being physisorbed and being closer to the surface when the vdW dispersions forces were used in the calculation. Calculated adsorption energies are shown in Table 11.

The adsorption of a H<sub>2</sub> molecule onto anatase (101) surface with oxygen vacancies, [TiO<sub>2</sub> + V<sub>O</sub>], and combined with noble metals (Pt, Pd, Au, and Ag) (Fig. 30) was investigated (96). The model employed was the hybrid B3LP that included Becke's three-parameter exchange and Lee-Yang-Parr correlation. The 3-1p1G model was used for the adsorption of H<sub>2</sub> to the anatase surface. The models indicated that all systems behaved with physisorption of H<sub>2</sub>, except for the Pt[TiO<sub>2</sub> + V<sub>O</sub>] where H<sub>2</sub> was shown to dissociate. The calculated binding energies are presented in Table 12.





**Fig. 28** Potential energy diagram for the conversions of formaldehyde and formate on rutile and SnO<sub>2</sub> surfaces (95).

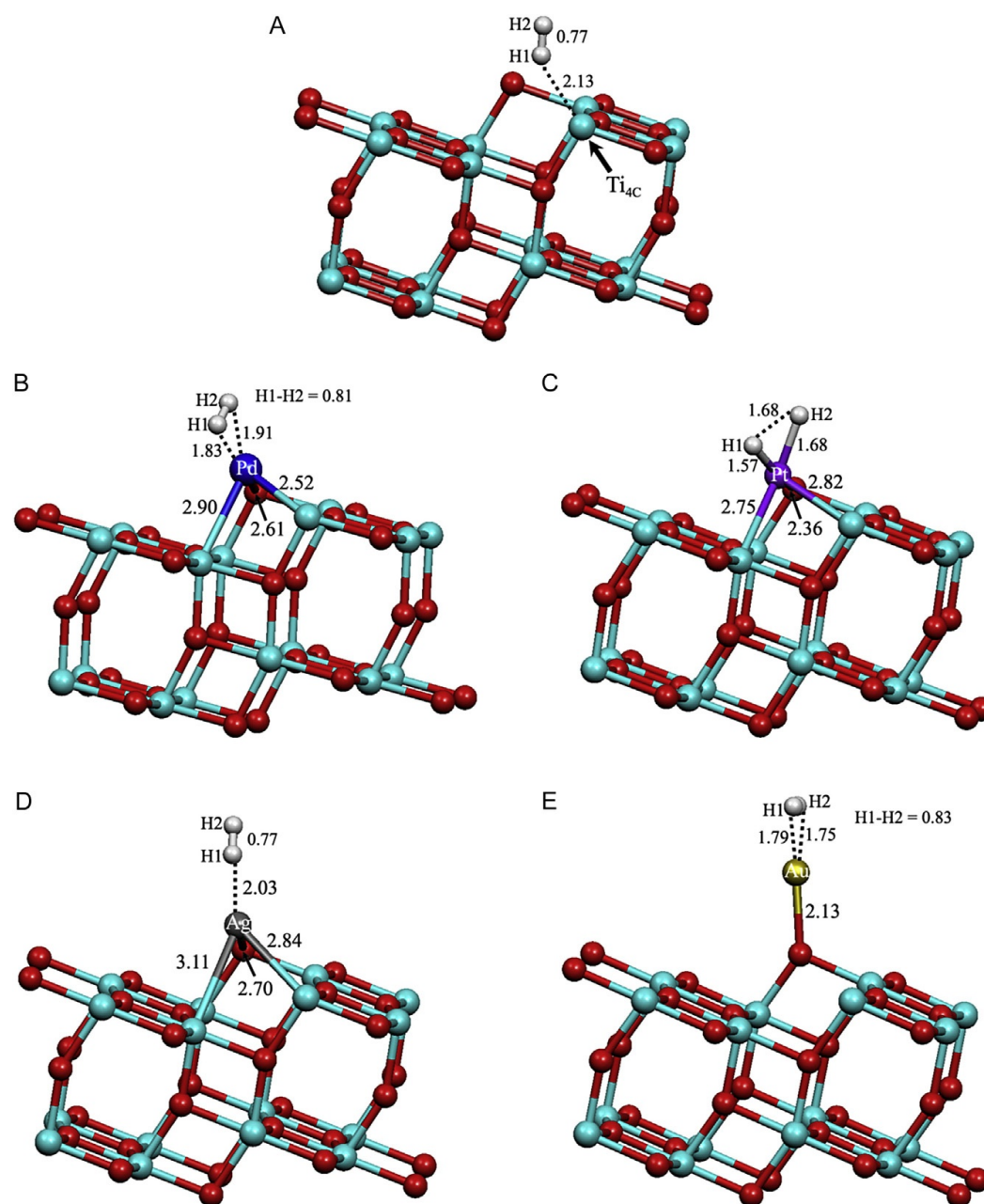


**Fig. 29** CO<sub>2</sub> adsorption on the anatase (001) surface (80).



**Table 11** Adsorption energies (eV) of  $\text{CO}_2$  on the anatase (001) surface (80).

	DFT+U+vdW	DFT+U
Bent	−1.528	−1.377
Linear 1	−0.264	—
Linear 2	−0.296	−0.159

**Fig. 30** Optimized structures for  $\text{H}_2$  molecule adsorbed to (A) oxygen vacancy ( $\text{TiO}_2 + \text{V}_\text{o}$ ), (B)  $\text{Pd}/(\text{TiO}_2 + \text{V}_\text{o})$ , (C)  $\text{Pt}/(\text{TiO}_2 + \text{V}_\text{o})$ , (D)  $\text{Ag}/(\text{TiO}_2 + \text{V}_\text{o})$ , and (E)  $\text{Au}/(\text{TiO}_2 + \text{V}_\text{o})$  (96).

**Table 12** Adsorption energies (eV) of H<sub>2</sub> on anatase (101) with and without and noble metal doping (96).

	<b>E<sub>ads</sub> (eV)</b>
TiO <sub>2</sub> + V <sub>O</sub>	−0.62
Pt[TiO <sub>2</sub> + V <sub>O</sub> ]	−2.11
Au[TiO <sub>2</sub> + V <sub>O</sub> ]	−1.55
Pd[TiO <sub>2</sub> + V <sub>O</sub> ]	−1.16
Ag[TiO <sub>2</sub> + V <sub>O</sub> ]	−0.62

The DFT calculations of OH-groups adsorbed on  $\gamma$ -Al<sub>2</sub>O<sub>3</sub>, TiO<sub>2</sub>, and MgO. For TiO<sub>2</sub>, anatase (101), (001), and (100) surfaces were examined (97). Calculations were performed using the generalized gradient approximation exchange correlation found within the VASP software. While the authors chose these materials due to their usage in typical thermochemical catalytic conversions, their underlying surface interactions with adsorbed compounds may lead to better understanding of how TiO<sub>2</sub> (and other materials) will behave under photocatalytic conditions and is, therefore, included in this discussion.

Bond energies, E<sub>M-O</sub> for the metal oxide crystals were determined using Eq. (5).

$$E_{M-O} = \frac{1}{n} [-U(M_xO_y) + U(M_x) + U(O_y)] \quad (5)$$

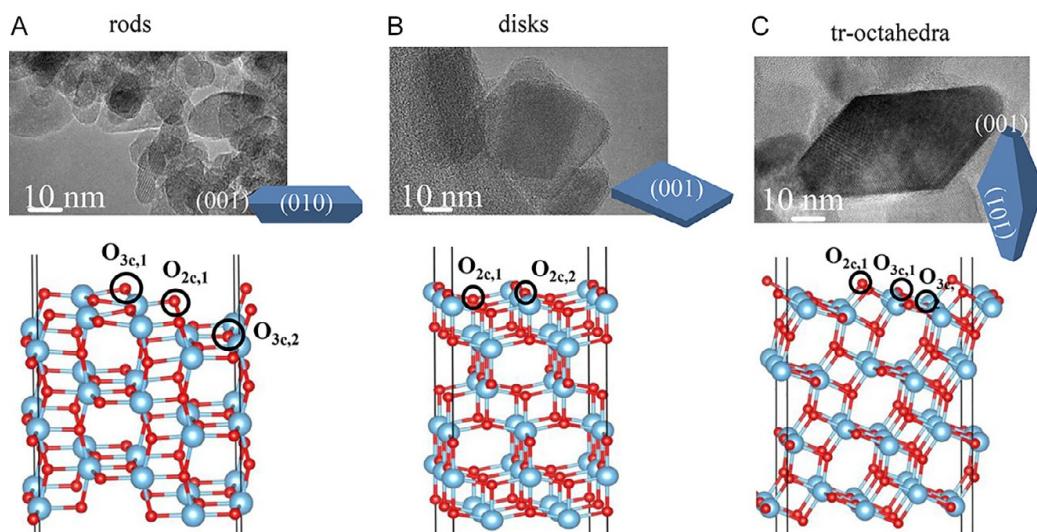
where n is the number of nearest oxygen neighbors and U(M<sub>x</sub>O<sub>y</sub>), U(M<sub>x</sub>), and U(O<sub>y</sub>) are the energies of the unit cell, unit cell with y oxygen atoms removed, and unit cell with x metal atoms removed, respectively.

As a comparison of material types, MgO, an ionic oxide, has a much lower E<sub>M-O</sub> than the covalent oxides, anatase and  $\gamma$ -Al<sub>2</sub>O<sub>3</sub> (Table 13). In general, ionic oxides have high coordination numbers due to electrostatic effects. Long range electrostatic effects, therefore, will play a major role as compared to the covalent oxides.

Water was found to adsorb, molecularly, only on flat surfaces that have the lowest coordinated cations (i.e., TiO<sub>2</sub> (101), Al<sub>2</sub>O<sub>3</sub> (100), and MgO (100)), indicating that cation coordination plays a major role in the dissociation of the water molecule. All other surfaces studied lead to the formation of hydroxyl groups. These hydroxyl groups formed from dissociation on

**Table 13** Bond energies (kJ/mol) for metal oxides (97).




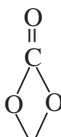

	MgO	TiO <sub>2</sub> (anatase)	$\gamma$ -Al <sub>2</sub> O <sub>3</sub>
E <sub>M-O</sub>	154	287	229

**Fig. 31** TEM images and their corresponding geometries of various TiO<sub>2</sub> surfaces (98).

all surfaces, except TiO<sub>2</sub> (001), in which hydrolysis was the underlying mechanism. The TiO<sub>2</sub> (001) surface facilitates strong hydrogen bonding between the two O<sub>1C</sub>-H formed, indicating that hydrogen bonding plays an important role in stabilizing hydrated systems. The hydrolysis reaction extracts surface oxygen (O<sup>2-</sup>) anions, causing a local destruction of the TiO<sub>2</sub> (001) surface lattice structure (97).

A Combined in situ IR and DFT study for interactions of both CO<sub>2</sub> and SO<sub>2</sub> on anatase rods {(010), (101), and (001)}, disks {(001) and (101)}, and truncated octahedra {(101), (001), and (010)} were investigated (98). CO<sub>2</sub> is proposed to adsorb, mechanistically, according to the surface geometry (Fig. 31). From the DFT study, the linear CO<sub>2</sub> molecule adsorbs via a monodentate carbonate by bending the CO<sub>2</sub> molecule coordinating with a surface oxygen atom. In the bridged carbonate motif, the CO<sub>2</sub> is also bent; however, the molecule is adsorbed via the C atom with a surface oxygen and with a molecular CO<sub>2</sub> oxygen and a Ti ion in a bidentate fashion (Table 14). The authors also state that the adsorption motifs are based on initial configurations that do not qualitatively match their initial structures due to weak coordination between the CO<sub>2</sub> and the surface sites. This leads to difficult comparisons between theory and experiment. The predicted CO<sub>2</sub> binding energies for different geometrically adsorbed CO<sub>2</sub> can be seen in Fig. 32.

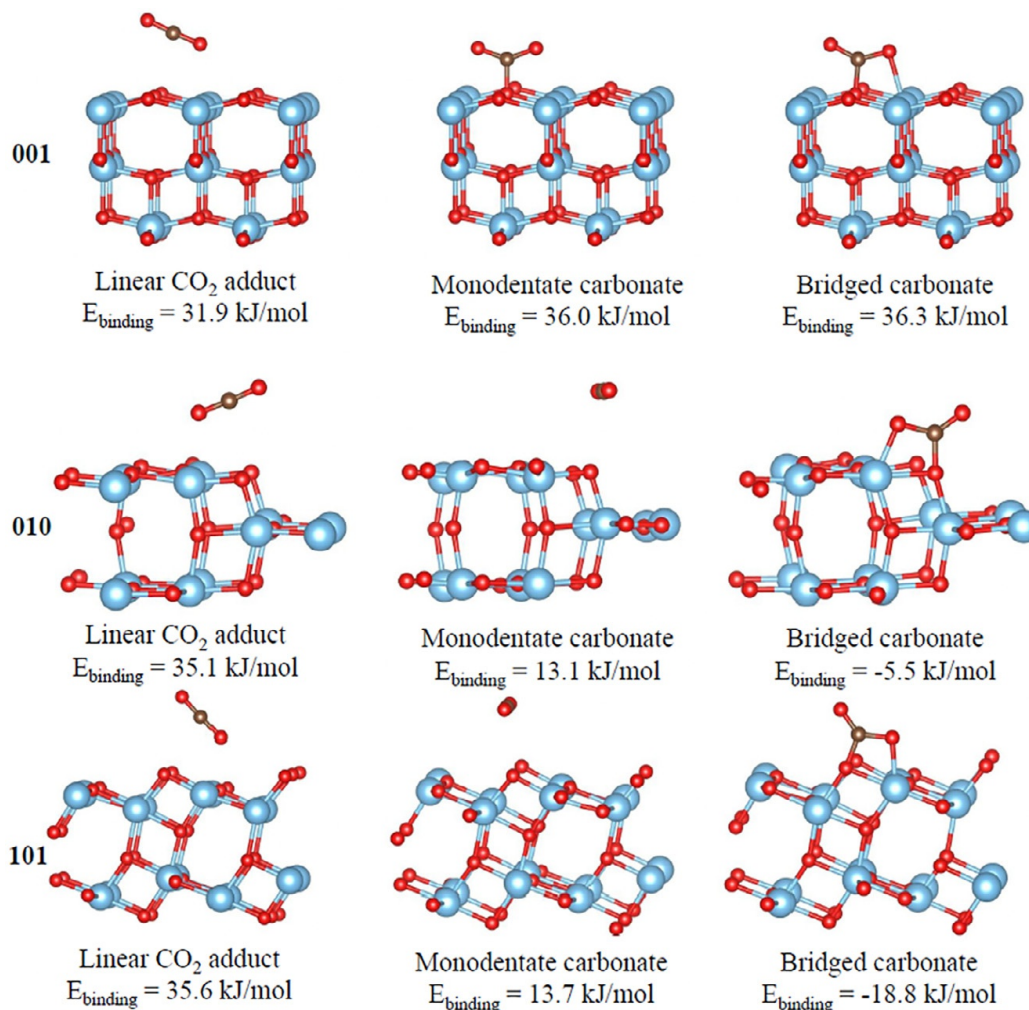
**Table 14** Adsorption geometries of CO<sub>2</sub> (98).

Geometry type	Configuration
Carboxylate	
Bicarbonate	
Monodentate carbonate	
Bidentate carbonate	
Bridged carbonate	

The TiO<sub>2</sub> disks primarily consist of the (001) surface, where bridged carbonates are predicted to be more dominant motif over the monodentate carbonates. Bicarbonates, however, are not predicted through DFT calculations but are seen from in situ IR experiments mostly due to a lack of surface hydroxylation that is apparent under experimental conditions but not considered in the theoretical calculations.

## 8.5 Summary of theoretical investigations

In summary, density functional theory has provided much fundamental understanding of the surface and subsurface phenomenon associated with defect chemistries, including oxygen vacancies and perturbations caused by surface modifications. However, there are limitations to the calculations, particularly when attempting to reconcile the effects of subsurface oxygen



**Fig. 32** Optimized TiO<sub>2</sub> disks (001) and truncated octahedron (010) facets with adsorbed CO<sub>2</sub> (98).

vacancies and potential gradients a might be the case under photocatalytic conditions. Understanding the limitations is paramount to effective modeling. There are significant differences between surface and subsurface oxygen vacancies that require specific computational parameters for a proper evaluation. An oxygen vacancy most likely induces midgap energy states, resulting in a lower band gap energy. However, without an electron acceptor (i.e., Pt, Au, C, etc.), these induced midgap energy states perform as electron–hole recombination centers. Evaluating the DOS for these midgap energy states requires Hubbard corrections, hybrid DFT models, or spin-unrestricted models. Applying van der Waals interaction forces provides a better understanding for adsorbed molecules such as CO<sub>2</sub>, formic acid, formaldehyde, or benzyl alcohol.



Adsorption energies of adsorbed molecules, such as  $\text{H}_2$ , on transition metal-doped  $\text{TiO}_2$  was enlightening, particularly in the case of Zr-doped rutile (110) where a second  $\text{H}_2$  molecule adsorbed more strongly than the first by 32.9 and 75.9% for Zr- $\text{TiO}_2$  and Zr- $[\text{TiO}_2 + \text{V}_\text{o}]$ , respectively. This phenomenon was not observed for other metals doped on  $\text{TiO}_2$  but could hinder reactions where  $\text{H}_2$  is used as a reductant, used either as a coreactant or evolved from water splitting reactions.



## 9. $\text{TiO}_2$ defect synthesis techniques for photocatalytic purposes

As computational output of  $\text{TiO}_2$  photocatalytic materials has surged over the last two decades, so has the desire to synthesize  $\text{TiO}_2$  materials capable of mimicking the results from the computations. The DFT computations (i.e., oxygen vacancies,  $\text{Ti}^{3+}$  sites, estimation of bandgap energies, etc.) only take into the activation of the surface site, particularly for reactions while subjected to UV and/or visible light. These calculations, however, do not take into account the other requirements of a catalyst, namely pore size distributions, surface areas, and robustness. As discussed in Section 8,  $\text{TiO}_2$  can be altered to create mid-gap energy states; however, electron–hole recombination times reduce catalyst effectiveness. An attempt is made here to reconcile these two worlds—computation and synthesis. Researchers often use various probe molecules (i.e., methylene blue, Rhodamine B,  $\text{CO}_2$ , etc.) to test the activity of the synthesized materials. While this work focuses on  $\text{CO}_2$  conversions on  $\text{TiO}_2$ , the activity of other probe molecules will also be presented for the sake of clarity and catalyst comparison purposes.

### 9.1 Synthesis methods for black $\text{TiO}_2$

Black  $\text{TiO}_2$  is a hydrogenated form of  $\text{TiO}_2$  that has shown to have improved photocatalytic properties. The methods tested include high pressure processes, thermal  $\text{H}_2$  annealing processes,  $\text{H}_2$  or metal reduction processes, and facile surfactant processes. These processes generally produce mesoporous anatase or anatase/rutile mixtures, whose properties greatly depend on the specific conditions employed for each method (99–101). For the facile surfactant process, preparation parameters and characterization information are presented in Table 15. None, however, presented bandgap energy values, complicating the comparison between DFT computations and synthesis. Instead, Electron Spin Resonance (ESR) was used by some to determine a material's ability to form electron–hole trapping sites.

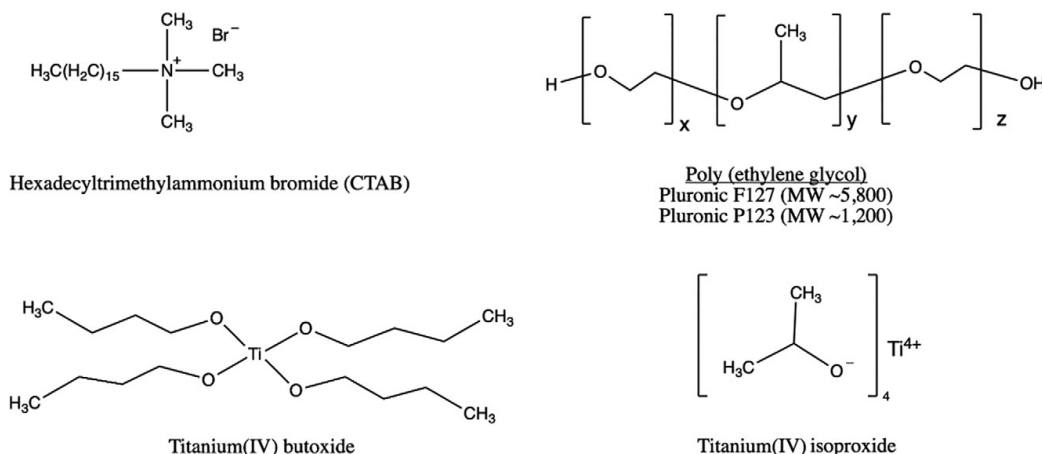
Table 15 Preparation parameters and outcomes for black TiO<sub>2</sub> synthesis.

Surfactant	Titania precursor: surfactant ratio, by mass	Calcination temp (°C)	BET surface area (m <sup>2</sup> /g)	Pore size (nm)	Pore volume (cm <sup>3</sup> /g)	Anatase crystal size (101) (nm)	G factor	Refs.
None	–	450 (air)	72	7.27	0.26	11	–	(99)
CTAB <sup>a</sup>	1:1 <sup>b</sup>	450 (air)	46	8.81	0.20	15	–	(99)
Pluronic F-127	2:1 <sup>c</sup>	400 (air)	48.36	23.42	0.293	7.84	1.9985	(100)
Pluronic F-127	1:1	400 (air)	85.54	13.07	0.316	7.04	2.0021	(100)
Pluronic F-127	1:2	400 (air)	110.00	14.17	0.439	6.17	2.0679	(100)
							2.0125	
							2.0729	
							1.9993	
Pluronic F-127	1:3	400 (air)	73.23	13.30	0.252	6.11	2.0679	(100)
							2.0125	
							2.0729	
							1.9993	
CTAB	10:1 <sup>b</sup>	80	71.05	2.49	0.044	5.2	–	(101)
CTAB	10:1	300	116.75	6.35	0.186	6.2	2.003	(101)

<sup>a</sup>CTAB—cetyltrimethylammonium bromide.

<sup>b</sup>Titanium (IV) tetrabutoxide.

<sup>c</sup>Titanium (IV) isopropoxide.



**Fig. 33** Precursor materials used in facile synthesis of  $\text{TiO}_2$ .

From the ESR, a G-factor is determined. G-factors  $>2$  indicate the formation of hole trapping sites (i.e., oxygen vacancies) (Fig. 33).

Reactions using these materials were typically performed with organic molecules. Under visible light photocatalytic conditions, the CTAB/ $\text{TiO}_2$  catalyst prepared by Zhong *et al.* showed significantly higher methyl orange decomposition rate constants compared to  $\text{TiO}_2$ , 0.6685 vs  $0.2021 \text{ h}^{-1}$ , respectively (99). They proposed that photo-generated holes can oxidize the methyl orange or react with surface absorbed water to form hydroxyl radicals. The rate of hydroxyl radical formation, as shown by Oseghe *et al.* was directly proportional to the surfactant concentration. As the concentration of surfactant increased during preparation, there is an increase in hydroxyl radical formation. However, photocatalytic degradation rates of methyl blue (Table 16) showed no correlation between OH radical formation and material activities. The authors attributed this phenomenon to the high surface area and electron-hole trapping sites of the catalyst rather than the OH radical formation (100).

In another study on the facile production of  $\text{TiO}_2$ , Han and coworkers combined tetrabutyl titanate in ethanol with acetic acid in DI water (102). The hydrolysis and polymerization took place in an ice bath (stirring for 2 h and aging for 24 h) before undergoing vacuum calcination at  $400^\circ\text{C}$  for 4 h (labeled B- $\text{TiO}_2$ ). To compare, white  $\text{TiO}_2$  was synthesized with the same method except calcination took place in air (labeled W- $\text{TiO}_2$ ). The EPR spectrum for W- $\text{TiO}_2$  showed no signal. The B- $\text{TiO}_2$  had a strong signal at  $g=2.002$ , indicating oxygen vacancies. The strong intensity implied a high concentration of oxygen vacancies. The XPS results confirmed the existence of oxygen vacancies. Photocatalytic experiments were carried

**Table 16** Pseudo first order kinetics for methyl blue decomposition (32 W daylight lamp) (100).

Sample	Rate constant (10 <sup>-3</sup> )	R <sup>2</sup>
Commercial TiO <sub>2</sub>	3.49	0.9735
T <sub>2</sub> S <sub>1</sub> <sup>a</sup>	3.88	0.9460
T <sub>1</sub> S <sub>1</sub>	2.34	0.9937
T <sub>1</sub> S <sub>2</sub>	3.66	0.9559
T <sub>1</sub> S <sub>3</sub>	4.18	0.9259

<sup>a</sup>Subscripts indicate mass ratios of the titanate precursor (titanium (IV) isopropoxide) and surfactant (Pluronic F-127).

**Table 17** Synthesis parameters and characterization results of plasma generated Black TiO<sub>2</sub> (103).

Electrolyte	Electrolyte concentration (mM)	Synthesis rate (mg/h)	Ti <sup>3+</sup> /Ti <sup>4+</sup>	Bandgap energy (eV)
KCl	0.3	13.2	0.170	3.08
	3.0	21.6	0.196	2.92
HNO <sub>3</sub>	0.3	32.2	0.311	2.50
	3.0	46.9	0.411	2.44

out in visible light using phenol as the test molecule. The pseudo-first order rate constants were 0.1316, 0.0176, and 0.0252 h<sup>-1</sup> for B-TiO<sub>2</sub>, W-TiO<sub>2</sub>, and Degussa P25, respectively. The fivefold increase in the rate constant for B-TiO<sub>2</sub> when compared to W-TiO<sub>2</sub> was attributed to the formation of continuous states and increased concentrations of photo-generated electron-hole pairs of the B-TiO<sub>2</sub>. These electron-hole pairs can be effectively separated by interface transfer due to the dense, compact nature of the nanoparticles (102).

A solution plasma technique was used for producing black TiO<sub>2</sub> with lower bandgap energies than typical anatase TiO<sub>2</sub>. Titanium rods were immersed in electrolytic solutions (either KCl or HNO<sub>3</sub>) and then subjected to pulsed (2.0 μs) 20 kHz voltage with discharge times 1–4 h. Samples were then dried (100 °C) overnight (Table 17). During the preparation, micro-gas bubbles formed around the electrode tips, whereby electrons flowed inside the gas bubbles. Consequently, plasma was formed within the gas/liquid interface. Interestingly, the electrolyte HNO<sub>3</sub> produced black

TiO<sub>2</sub> 2.17 to 2.44 times faster than the KCl electrolyte, possibly due to the highly acidic nature and conductivity of the HNO<sub>3</sub>. Two mechanisms were proposed by the authors toward the formation of Ti<sup>3+</sup> ions. The first is from the rapid quenching of the molten Ti clusters as they disengage from the electrode tip. The second from the reaction between the lattice oxygen and highly energetic atoms (i.e., H, O, and OH radicals) or electrons inside the plasma zone. Either would lead to the formation of oxygen vacancies, leaving two electrons that delocalize to neighboring titanium atom. Photocatalytic reactions were performed using glycerol as a test molecule. Reactions took place in the UV spectrum. Glycerol conversion across the synthesized catalysts followed the pattern of maximum conversion with lowest bandgap material; least conversion with highest bandgap (103).

Xin *et al.* examined calcination temperatures (300–700 °C) for tailoring the location of oxygen vacancies (104). Their intent was to create more sub-surface Ti<sup>3+</sup> sites rather than surface sites that readily undergo oxidation via reacting species. The preparation method consisted of titanium hydride powder dissolved in water before adding 30 wt% H<sub>2</sub>O<sub>2</sub> and vigorously stirring for 12 h. After which, ethanol was added, and a pH 9 was accomplished using NaOH. Sodium borohydride was added as an antioxidant. The system was autoclaved at 180 °C for 24 h. Ethanol and DI water were used to remove impurities (Na<sup>+</sup>, Cl<sup>−</sup>, BO<sub>3</sub><sup>2−</sup>). The powders were dried in a vacuum oven for 12 h before undergoing calcination (300–700 °C) at 4 °C/min.

Characterization information of the self-doped TiO<sub>2</sub> can be seen in Table 18. The high temperature annealing increases the crystallite size but at the expense of surface area. Likewise, there is a definite red-shift in the 300, 400, and 500 °C samples but a slight blue-shift in the 600 and 700 °C samples. XPS was used to probe for Ti<sup>3+</sup> sites on the surface since XPS is applicable for up to 5 nm below the surface.

**Table 18** Physico-chemical properties of self-doped TiO<sub>2</sub> (104).

Sample ID	Calcination temperature (°C)	Anatase crystal size (101) (nm)	BET surface area (m <sup>2</sup> /g)	Bandgap energy (eV)
TiO <sub>2-x</sub>	–	8.9	272.87	3.12
TiO <sub>2-x</sub> -300	300	9.1	245.96	3.03
TiO <sub>2-x</sub> -400	400	9.2	235.06	2.85
TiO <sub>2-x</sub> -500	500	9.5	170.48	2.63
TiO <sub>2-x</sub> -600	600	9.7	147.80	2.67
TiO <sub>2-x</sub> -700	700	14.2	78.98	2.75

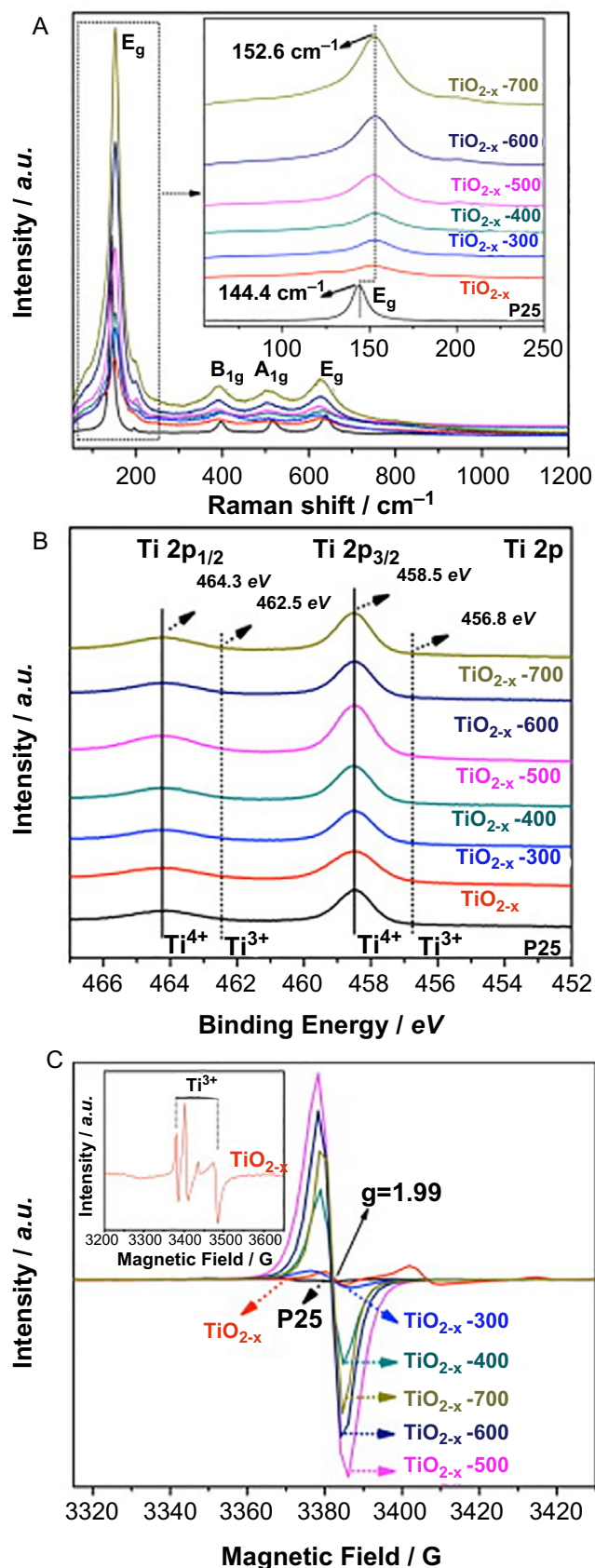


XPS (Fig. 34B) was used to probe for Ti<sup>3+</sup> sites on the surface since XPS is applicable for up to 5 nm below the surface. Due to an absence of peaks at 456.8 and 462.5 eV, the XPS shows no Ti<sup>3+</sup> sites on the surfaces of the prepared samples. The EPR spectra (Fig. 34C), on the other hand, shows an abundance of Ti<sup>3+</sup> sites with the maximum occurring at the 500 °C annealing temperature. The authors state that the intense axially symmetric signal at  $g = 1.99$  indicates free electrons occupying interior Ti positions (i.e., Ti<sup>3+</sup> defects). A schematic of the synthesis preparation and mechanism can be seen in Fig. 35. Performance testing was conducted using methylene blue in the visible light spectrum. Photocatalytic activity followed annealing temperature in the order of  $500 > 600 > 700 > 400 > 300$  °C  $\gg$  no annealing > P25. These results seem to suggest that Ti<sup>3+</sup> defect sites can be “engineered,” and the catalyst can be pushed toward visible light activity (104).

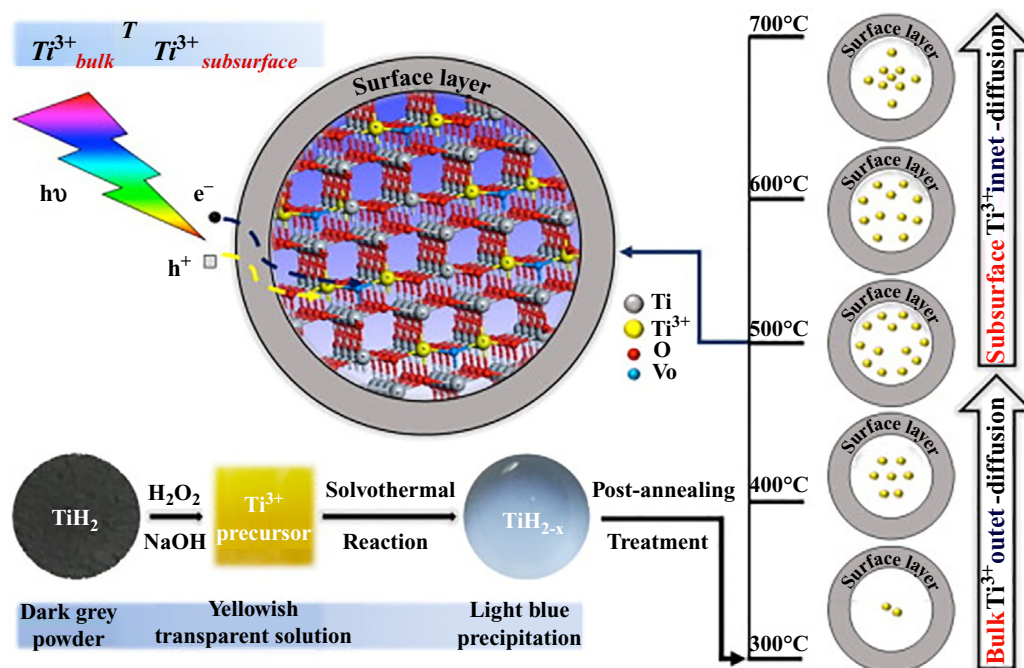
A triblock copolymer, Pluronic P123, was used as a template to synthesize an ordered mesoporous black TiO<sub>2</sub>, yielding a bandgap energy of 2.82 eV. Photocatalytic experiments showed 1.36  $\mu\text{mol/g}_{\text{cat}}$  h H<sub>2</sub> production, compared to 0.77  $\mu\text{mol/g}_{\text{cat}}$  h of the white TiO<sub>2</sub> (AM 1.5 light source with 100 mW/cm<sup>2</sup> power density) (105).

## 9.2 Controlling Ti<sup>3+</sup> sites

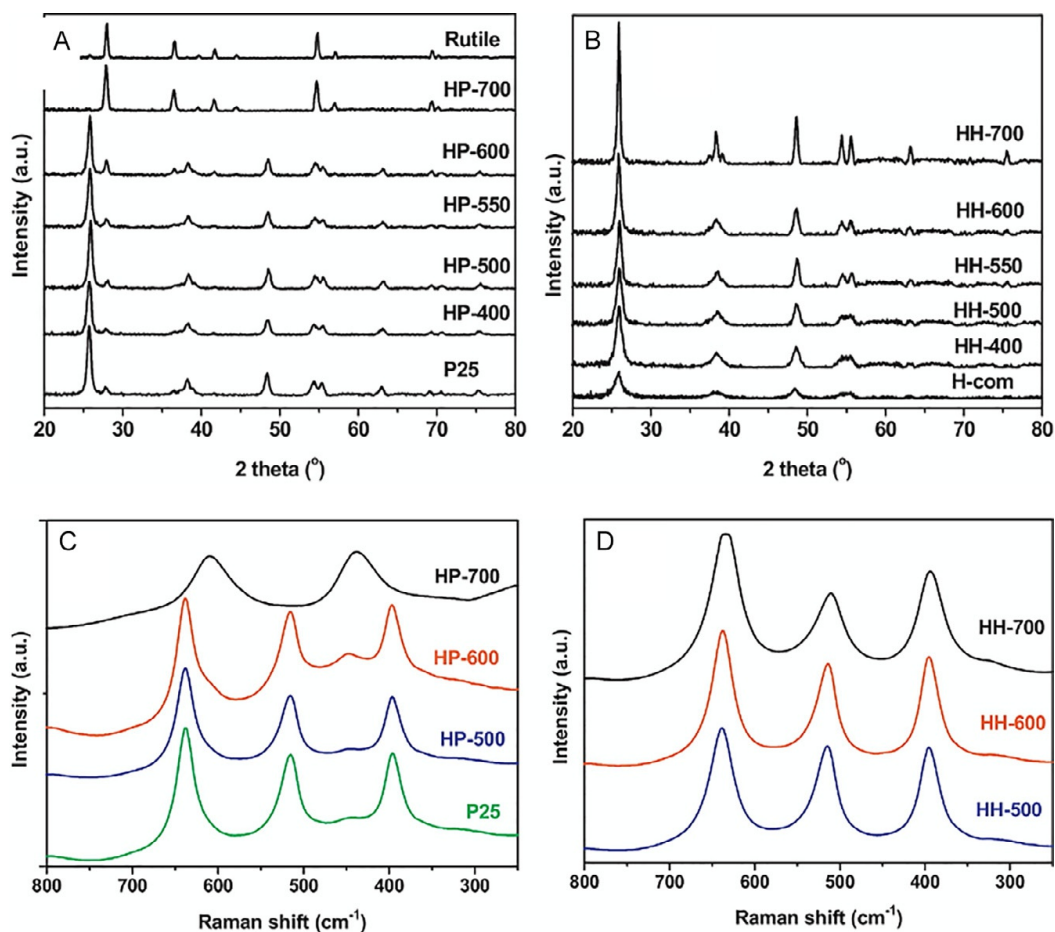
Saputera *et al.* and Hamdy *et al.* developed synthesis methods for Ti<sup>3+</sup>-containing TiO<sub>2</sub> and size-tunable TiO<sub>2</sub> nanoparticles, respectively (106,107). Commercial TiO<sub>2</sub> can be hydrogenated (flowing H<sub>2</sub> during calcination process at temperatures ranging from 400 to 700 °C) to form Ti<sup>3+</sup>-containing TiO<sub>2</sub>. The color change for Wombikat and rutile samples changed from white, pale yellow, yellowish gray, and then to gray according to calcination temperatures, 400, 500, 600, and 700 °C, respectively. P25, on the other hand, changed to pale yellow at 400 °C and then to off-white for higher temperatures. Note, then, that these do fall within the black TiO<sub>2</sub> classification. X-ray diffractions and Raman spectra can be seen in Fig. 36. There are significant phase transitions and the higher temperatures, particularly above 600 °C. Photocatalytic degradation of methyl orange was best using the hydrogenated P25 that was calcined at 500 °C ( $k \sim 9400 \text{ min}^{-1}$ ). Decomposition rate constants for the hydrogenated Hombikat UV-100 (calcined at 600 °C) and the hydrogenated P25 (calcined at 550 °C) were  $\sim 3800 \text{ min}^{-1}$ , respectively. EPR spectra revealed that all three phases of TiO<sub>2</sub>, when hydrogenated, could be made to form oxygen vacancies. The starting TiO<sub>2</sub> phase was not a major factor (105).



**Fig. 34** Raman shift, XPS, and EPR spectra for black  $\text{TiO}_2$  undergoing different annealing temperatures (104).



**Fig. 35** Proposed mechanism for the formation and distribution of Ti<sup>3+</sup> sites for black TiO<sub>2</sub> (104).



**Fig. 36** Characterizations for hydrogenated TiO<sub>2</sub>. (A) XRD of P25 and rutile, (B) XRD of Hombikat UV-100, (C) Raman spectra of P25, and (D) Raman spectra of Hombikat UV-100 (106).

### 9.3 Synthesis of doped TiO<sub>2</sub> photocatalysts

To enhance the efficiency of TiO<sub>2</sub> photocatalysts, N and S were codoped onto anatase using thiourea prior to 400 °C calcination in air for 1 h. XPS spectra (Fig. 37) revealed two N 1s peaks with binding energies of 399.2 and

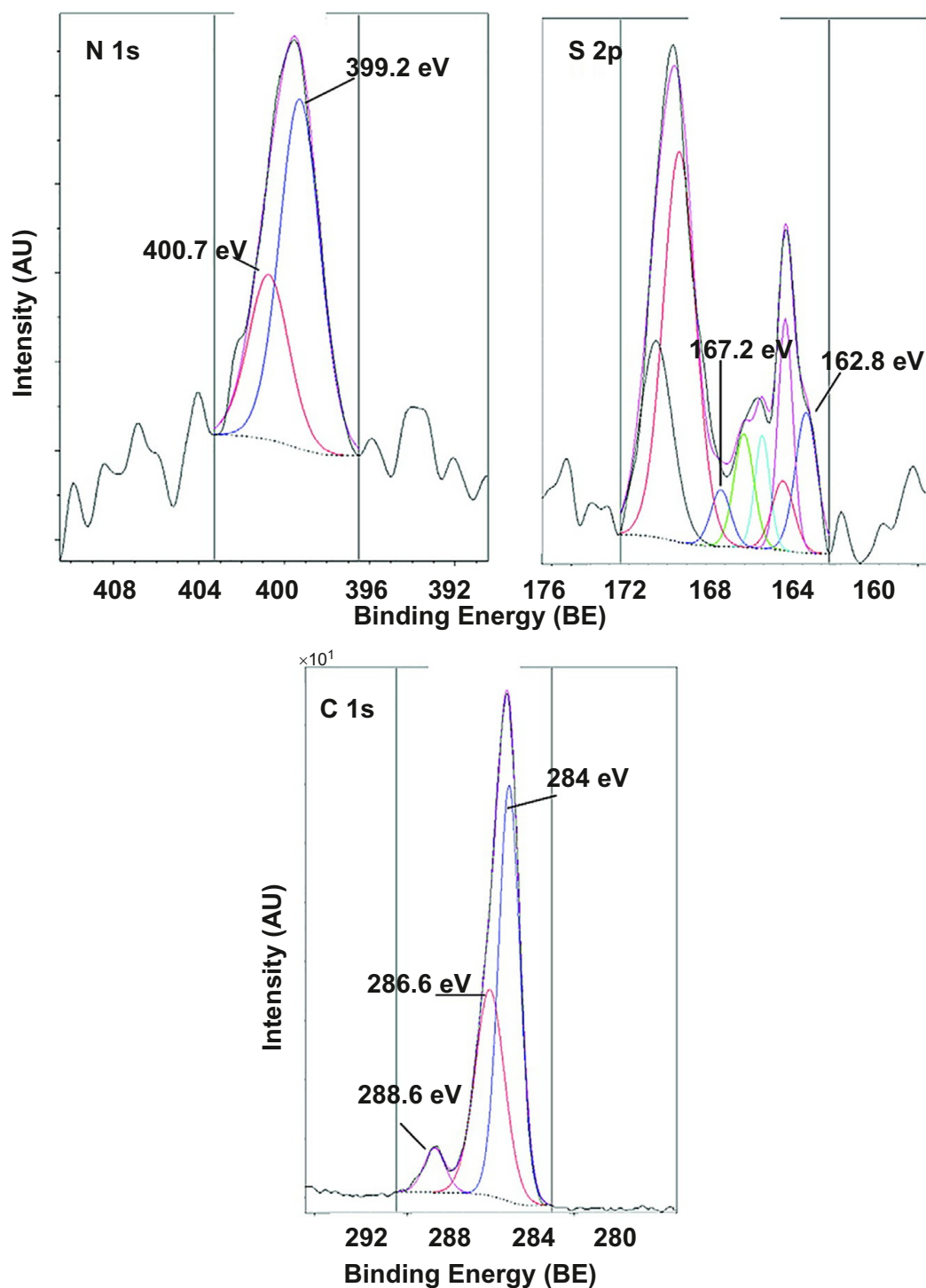


Fig. 37 High resolution XPS illustrating N 1s and S 2p peaks for TiO<sub>2</sub> codoped with N and S using thiourea (108).

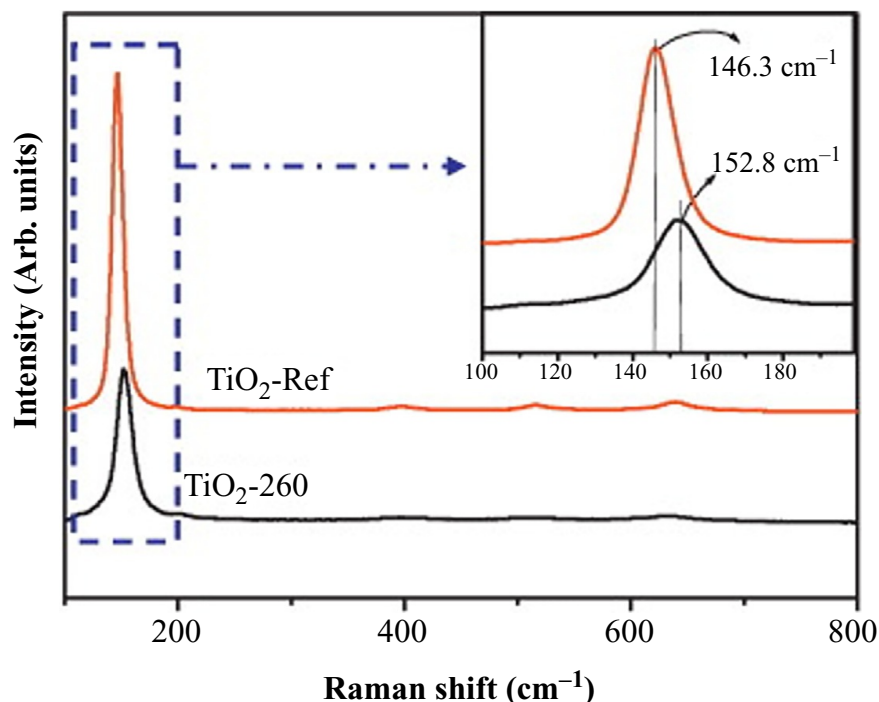
400.7 eV that were believed to be due to N-doping, forming Ti–O–N species. In addition, S 2p peaks were found for high oxidation states, perhaps SO<sub>4</sub><sup>2−</sup> with a binding energy >168 eV. Oxygen vacancies were investigated using ESR, finding none for undoped TiO<sub>2</sub>. ESR of singlet oxygen was made possible using 2,2,6,6-tetramethylpiperidine-1-oxyl (TEMPO) as a paramagnetic product. In a previous study, the authors found that hydroxyl radicals could not be formed using illuminated N/S codoped TiO<sub>2</sub>, perhaps because photoinduced holes at the midgap levels are insufficient to reach the redox potential needed to form the radicals. The authors concluded that electrons from midgap energy levels could be excited by visible light absorption. Molecular oxygen could be adsorbed onto oxygen vacancies and then reacted with the excited electrons, producing superoxide radicals. The radicals could then be oxidized by the holes trapped on the midgap N, S states (108,109).

Wang *et al.* investigated a supercritical preparation technique using Ti(n-OC<sub>4</sub>H<sub>9</sub>)<sub>4</sub> and TiF<sub>4</sub> (50:50 M ratio) dissolved in nitric acid/ethanol solution (110). The catalyst samples were subjected to supercritical conditions ( $240 \leq T \leq 280$  °C) for 2 h before drying for 6 h at 80 °C. For comparison purposes, a reference TiO<sub>2</sub> was synthesized using tetrabutyl titanate in an aqueous HF solution. As shown in Table 19, surface area, pore volume, and pore diameter are considerably smaller than the same characteristics achieved via surfactant preparation methods. X-Ray diffraction showed that anatase was chiefly formed with typical 2-theta peaks appearing at 25.8°, 37.7°, 47.8°, and 55.0°, which are representative of (101), (004),

**Table 19** Structural characteristics of TiO<sub>2</sub> photocatalysts synthesized under supercritical conditions (110).

Sample ID	Synthesis temperature (°C)	BET surface area (m <sup>2</sup> /g)	Pore volume (cm <sup>3</sup> /g)	Pore size (nm)
TiO <sub>2</sub> —Ref	—	96	0.39	16
TiO <sub>2</sub> —240	240	40	0.09	2.1
TiO <sub>2</sub> —250	250	48	0.11	2.1
TiO <sub>2</sub> —260	260	51	0.17	2.3
TiO <sub>2</sub> —270	270	51	0.17	2.2
TiO <sub>2</sub> —280	280	50	0.16	2.0

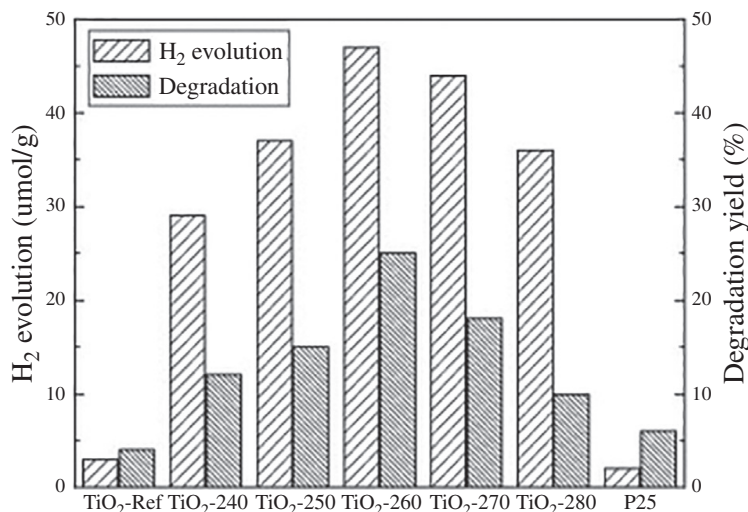




**Fig. 38** Raman spectra illustrating formation of  $\text{Ti}^{3+}$  from a  $6.5 \text{ cm}^{-1}$  shift from principle peak position (110).

(200), and (211) facets, respectively. The degree of crystallization increased with increased synthesis temperature, and (001) facets formed as the  $\text{TiO}_2$  transformed from octahedra to decahedra. The EPR spectra had strong signals at 1.95 and 2.00, confirming the presence of  $\text{Ti}^{3+}$ . The Raman spectra (Fig. 38) showed a  $6.5 \text{ cm}^{-1}$  shift from the principle peak position ( $\text{TiO}_2$ —260 vs  $\text{TiO}_2$ —ref), which further confirmed the presence of oxygen vacancies. These oxygen vacancies were attributed to the absorbance of visible light shown by the UV–vis diffuse reflectance spectra.

Reaction experiments (Fig. 39) were carried out synchronously using Pt- $\text{TiO}_2$  as an  $\text{H}_2$  evolution catalyst along with the supercritically-produced  $\text{TiO}_2$  catalysts for degradation of methylene blue. The reference  $\text{TiO}_2$  and the P25 had low perform, presumably due to their relatively large bandgaps. The  $\text{TiO}_2$ —260 catalyst gave the best performance most likely due to a transformation from nanorods to nanosheets between 240 and 260 °C, which left exposed (001) facets. The (001) facets had increased surface energies and favored visible light excitation. The (001) facets could also retard electron–hole recombinations, thus increasing quantum efficiency. The authors hypothesized that the lower reactivity of the 270 and 280 °C produced catalysts was due to agglomeration and stacking of  $\text{TiO}_2$  nanosheets (110).



**Fig. 39** Reaction results of TiO<sub>2</sub> photocatalysts synthesized under supercritical conditions (reaction conditions: Aqueous methylene blue, 30 °C, 3 h, 300 W Xenon lamp,  $\lambda$  420 nm) (110).

A thorough investigation into the photocatalytic performance and mechanism for Ni(OH)<sub>2</sub>/TiO<sub>2</sub> and Ni(OH)<sub>2</sub>/Ni<sub>x</sub>O/TiO<sub>2</sub> catalysts was performed by Neppolian's (111,112). To prepared anatase dispersed in water, nickel nitrate hexahydrate was added with either a N<sub>2</sub> or O<sub>2</sub> purge, adjustment of pH with NaOH, and either in darkness or with UV–vis light (Table 20). Photocatalytic activity, H<sub>2</sub> production from H<sub>2</sub>O using glycerol as a hole scavenger, was tested in direct solar light using a mixture of glycerol and water (9:95 v/v). The UV–vis diffuse reflectance spectra (Fig. 40a) of the materials showed an absorption edge at ~390 nm; however, the –ONT samples showed a second absorption peak at 675 nm. The Kubelka–Munk plot (Fig. 40b) yielded bandgap energies of 3.18, 3.10, and 3.06 for TiO<sub>2</sub>, a-O<sub>2</sub>ONT, and d-O<sub>2</sub>ONT catalysts, respectively. This lowering of the bandgap was attributed to the effect of the Ni(OH)<sub>2</sub> and O<sub>2</sub> interactions. In addition, all of the –ONT samples had bandgap energy excitations into the visible spectrum.

Valence band XPS was performed to elucidate the role of O<sub>2</sub> in the performance of the photocatalyst. As shown in Table 20, the valance band edge (VBE) shifts downward compared to pure TiO<sub>2</sub>. This is a remarkable feature but explains why the bandgap energy is still fairly large, but the catalysts are excited in the visible region. The authors concluded that defect states are formed in between the conduction and valence bands, causing the VBE to shift to lower energies. Furthermore, the addition of photo-reduced graphene (rGO) provided extended catalyst lifetimes under a 4-cycle test (111).

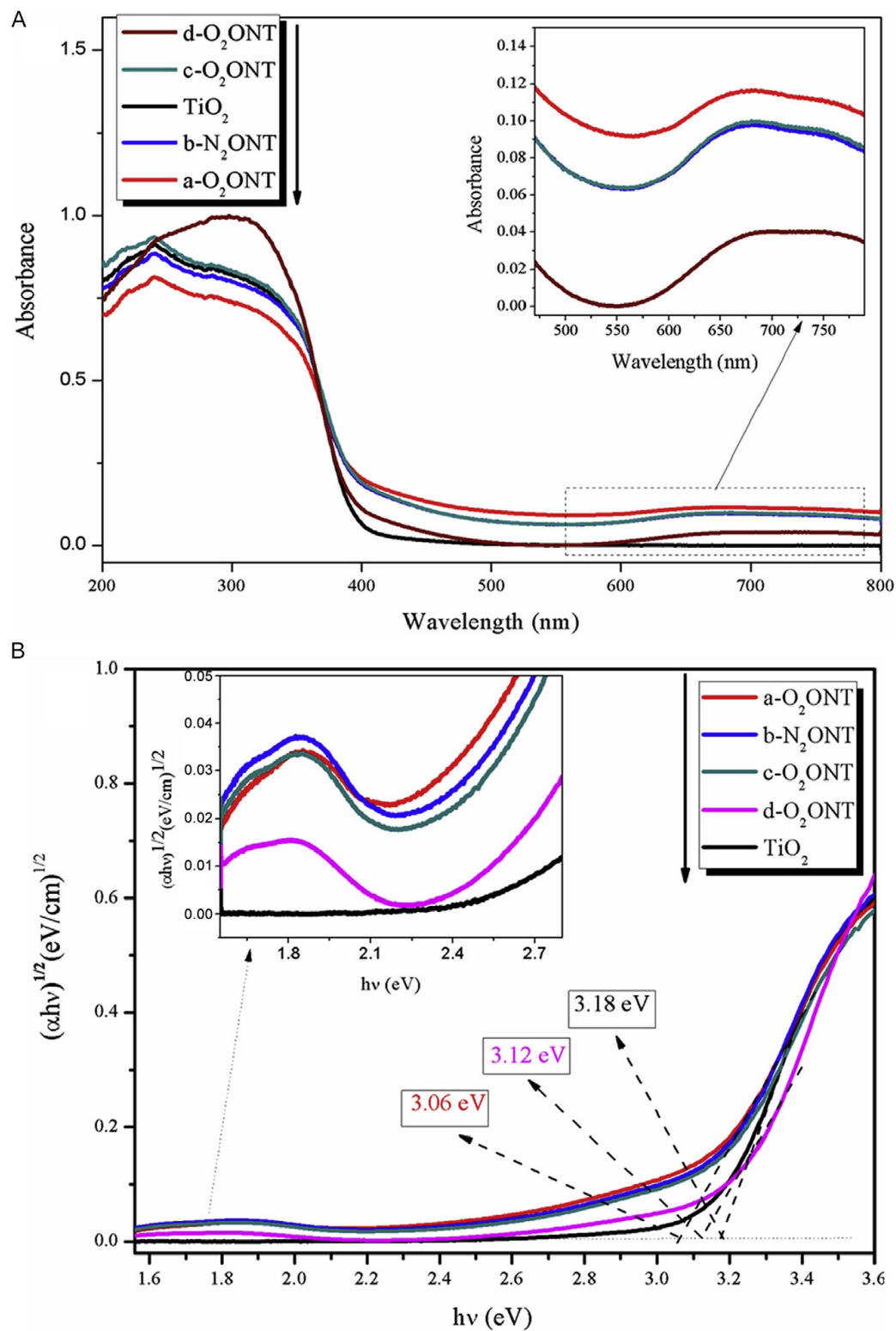
**Table 20** Ni(OH)<sub>2</sub>/TiO<sub>2</sub> formulation characterization and reaction results (111).

Sample ID	G factor	Bandgap energy (eV)	Valence band energy (eV)	XPS O1s peak area ratio <sup>a</sup>	H <sub>2</sub> production (μmol/g <sub>cat</sub> /h)
TiO <sub>2</sub> <sup>b</sup>	2.004	3.18	2.71	—	115
4O <sub>2</sub> T <sup>c</sup>	2.004	—	—	—	367
a-O <sub>2</sub> ONT <sup>d</sup>	2.4	3.06	1.96	0.49	6624
b-N <sub>2</sub> ONT <sup>e</sup>	2.24	3.08	1.99	0.37	4468
c-O <sub>2</sub> ONT <sup>f</sup>	—	3.09	2.27	0.30	4830
d-O <sub>2</sub> ONT <sup>g</sup>	2.04	3.12	2.44	2.02	8289
O <sub>2</sub> ONTG <sup>h</sup>	—	—	—	—	11,500 <sup>i</sup>

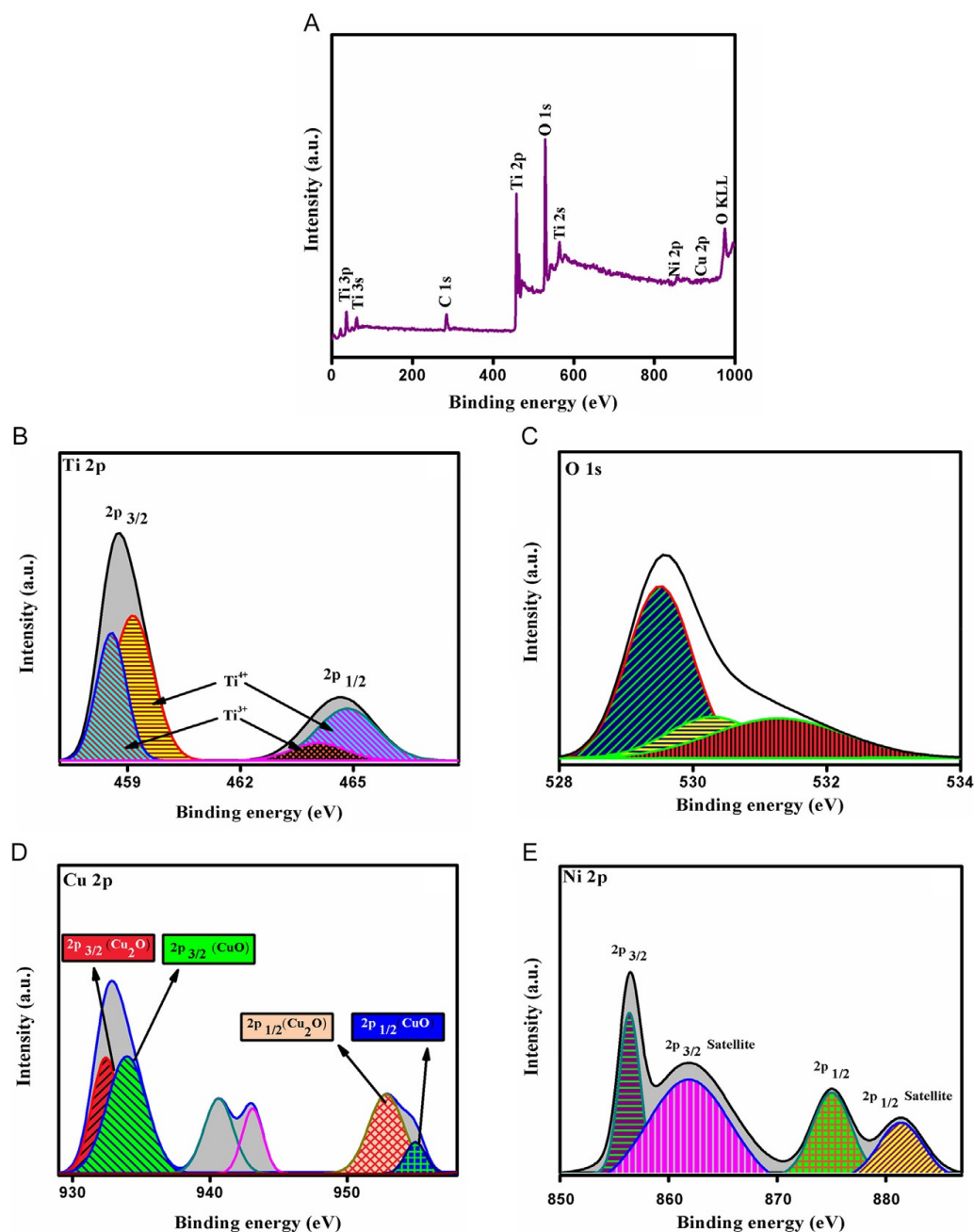
<sup>a</sup>Ratio: (Ti—OH)/(Ti—O—Ti).<sup>b</sup>TiO<sub>2</sub> → No purging.<sup>c</sup>4O<sub>2</sub>T O<sub>2</sub> → O<sub>2</sub> purging before and after NaOH addition.<sup>d</sup>a-O<sub>2</sub>ONT → O<sub>2</sub> purging after NaOH addition.<sup>e</sup>b-N<sub>2</sub>ONT → N<sub>2</sub> purging before NaOH addition.<sup>f</sup>c-O<sub>2</sub>ONT → O<sub>2</sub> purging before NaOH addition.<sup>g</sup>d-O<sub>2</sub>ONT → O<sub>2</sub> purging before and after NaOH addition, 250 W Xenon lamp (40 min).<sup>h</sup>O<sub>2</sub>NTG → addition of graphene, N<sub>2</sub> purging (30 min), 250 W Xenon lamp (4 h).<sup>i</sup>Adapted from graph.

Using a sol–gel preparation method, Sugha *et al.* synthesized a TiO<sub>2</sub> containing both nickel hydroxide and copper oxide within the lattice structure (112). Initial studies showed that 0.5 wt% Cu<sub>x</sub>O/TiO<sub>2</sub> was an optimized photocatalyst. To that, Ni(OH)<sub>2</sub> (0–2.0 wt%) was tested for its photocatalytic performance of water splitting. The optimum catalyst (1 wt% Cu<sub>x</sub>O/TiO<sub>2</sub>) yielded a hydrogen production rate of 15,789 μmol/g<sub>cat</sub>/h. The XPS spectra (Fig. 41) shows spin–orbital split peaks at 458.5 and 464.1 eV (Ti 2p<sub>3/2</sub> and Ti 2p<sub>1/2</sub>, respectively), which corresponds to Ti<sup>3+</sup> sites. These results suggest that nickel hydroxide is attached to the surface via hydrogen bonding, possibly from the OH groups binding with surface lattice oxygens. The effect of copper, on the other hand, was shown by the doublet peaks at 934.4 and 954.6 eV (Cu 2p<sub>3/2</sub> and Cu 2p<sub>1/2</sub>, respectively). The CuO was seen as satellite peaks at 940.6 and 943.1 eV (Cu 2p<sub>3/2</sub> and Cu 2p<sub>1/2</sub>, respectively). The nickel and copper were found to exist as Ni<sup>+</sup> and Cu<sup>+</sup>, according to the XPS results.

The mechanism for water splitting (Fig. 42) shows two possible pathways for charge transfer at the Ni(OH)<sub>2</sub>/TiO<sub>2</sub> and Cu<sub>x</sub>O/TiO<sub>2</sub> interface. Electron excitation from irradiation of solar light takes place on TiO<sub>2</sub>, Cu<sub>x</sub>O, and CuO surfaces. TiO<sub>2</sub> had the fastest electron–hole recombination



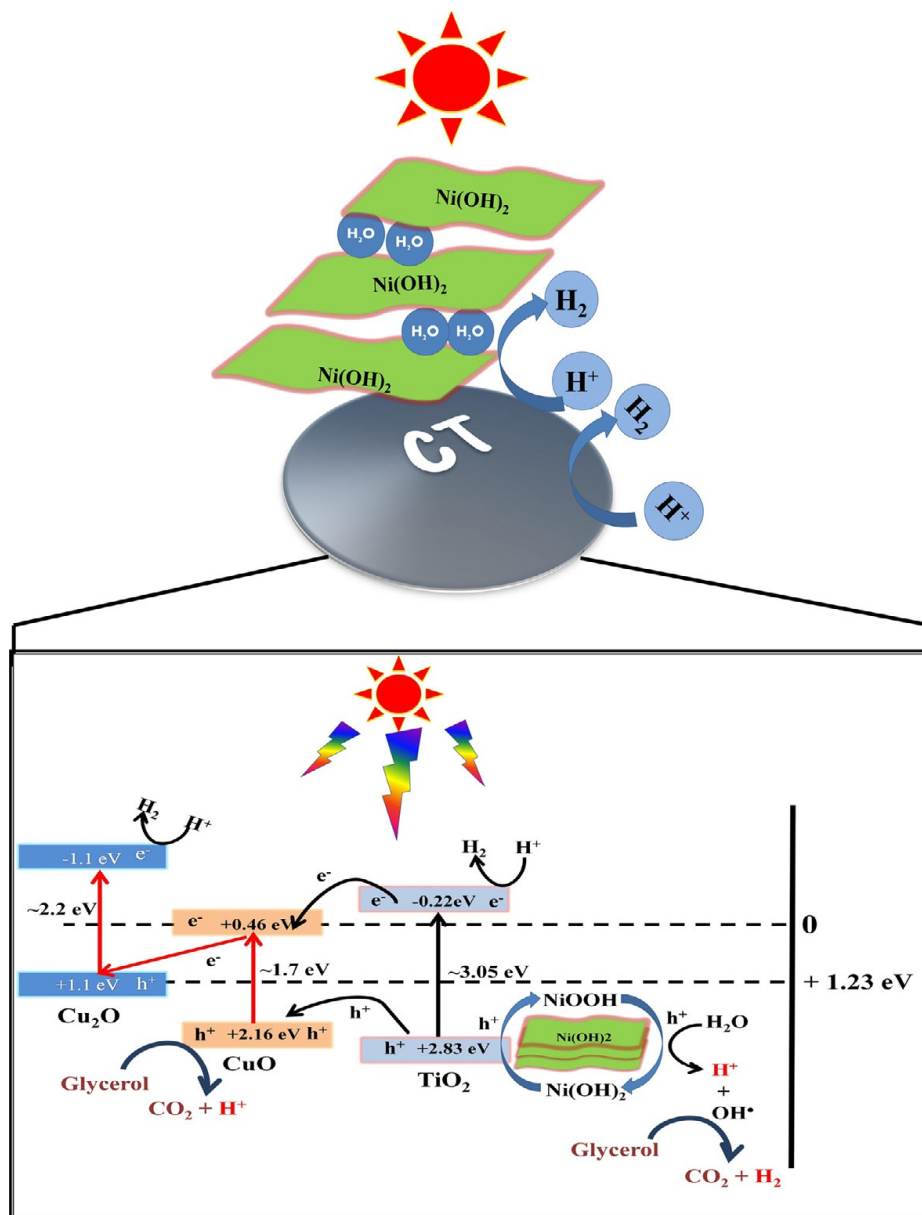
**Fig. 40** (A) UV-Vis absorption spectra, (B) determination of Bandgap energy from Kubelka-Munk function (111).



**Fig. 41** XPS spectrum of 1.0 wt% Ni(OH)<sub>2</sub> supported on 1 wt% Cu<sub>x</sub>O/TiO<sub>2</sub> (112).

and poor light absorption, yielding only 4.116  $\mu\text{mol/g}_{\text{cat}}/\text{h}$  hydrogen production. Subsequently, Ni(OH)<sub>2</sub> had a layered morphology that was paramount in H<sub>2</sub> production due to weak bond interactions of the OH groups that intercalated with water's hydrogen bonding. The photogenerated holes in the valence band were believed to be scavenged by Ni(OH)<sub>2</sub>, which is known to oxidize to NiOOH. When reduced back to Ni(OH)<sub>2</sub>, NiOOH provides holes for H<sub>2</sub>O in the interlayer space. The H<sub>2</sub>O increases the





**Fig. 42** Proposed mechanism for water splitting on Ni(OH)<sub>2</sub>/Cu<sub>x</sub>O/TiO<sub>2</sub> illustrating two different charge transfer pathways (112).

surface charge transfer reactions. The desorbed water dissociates, thus increasing the rate of surface reactions from the generated H<sup>+</sup>. The role of the glycerol is to scavenge TiO<sub>2</sub> valence band holes, producing H<sup>+</sup> ions for increased H<sub>2</sub> production. Addition of copper doubles the charge transfer mechanism via a z-scheme. The synergistic effect observed by codoping Ni(OH)<sub>2</sub> and Cu<sub>x</sub>O onto TiO<sub>2</sub> was due to suppression of electron–hole recombinations at the Cu<sub>x</sub>O/TiO<sub>2</sub> heterojunctions and by trapping holes for the Ni(OH)<sub>2</sub> redox reactions (112).

While much attention is given toward crystalline  $\text{TiO}_2$  structures, amorphous structures can also be used as photocatalysts. Hitam *et al.* used an electrolysis technique to synthesize  $\text{CuO}/\text{TiO}_2$  with good results for desulfurization of dibenzothiophene via a sol–gel method, titanium (IV) isopropoxide was used to prepare the amorphous  $\text{TiO}_2$  (113). The electrolytic cell, used to prepare  $\text{CuO}$  nanoparticles, was comprised of a platinum plate cathode and a copper plate anode operating at 120 mA and 273 K. The  $\text{TiO}_2$  was impregnated with  $\text{CuO}$  (5–20 wt%).

The proposed structure (Fig. 42) was determined using vibrational and XP spectroscopies. The FTIR spectra (not shown) indicated C–H and C–N stretching modes of the  $\text{CuO}/\text{TiO}_2$  catalysts as well as the formation of Ti–O–N. The consumption of tetraethylammonium perchlorate during electrolysis was deduced from the decrease in the IR bands with the increase in Cu loading concentration. Comparing the AT and 10CAT materials, the XPS spectra was more revealing of the catalyst structure (Fig. 43). Approximately half of the  $\text{Ti}^{4+}$  were reduced to  $\text{Ti}^{3+}$  states (i.e., formation of oxygen vacancies), noticed by comparing the peak intensities of Ti  $2p_{1/2}$  and Ti  $2p_{3/2}$  (470–455 eV). In addition, Ti–O–H and Ti–O–H formations are seen in the O 1s spectrum (531.8 and 529.9 eV, respectively) in the AT catalyst. These peaks also decrease with the incorporation of Cu, with two new peaks developing at 532.1 and 530.5 eV which were attributed to

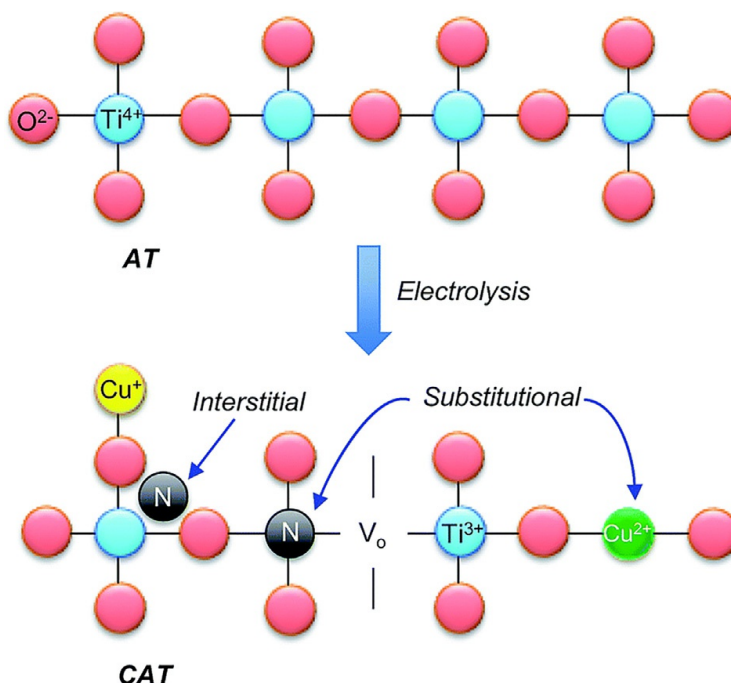


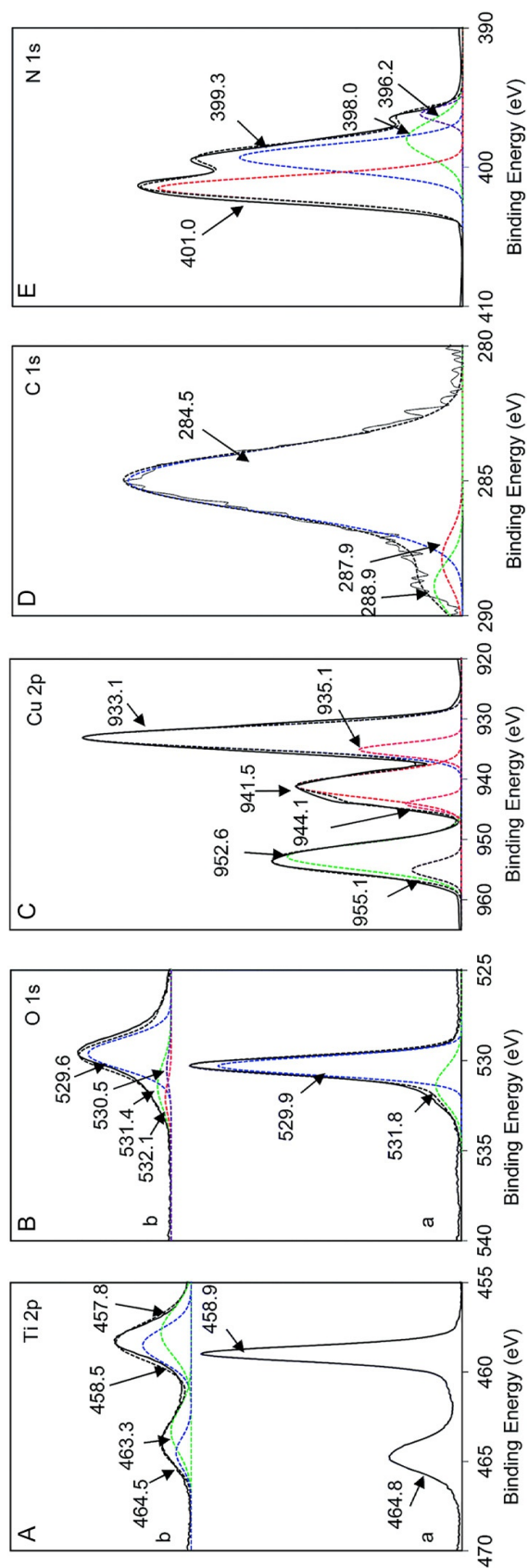
Fig. 43 Proposed structure of the  $\text{CuO}/\text{TiO}_2$  catalyst with interstitial N formation (113).

Ti-O-N and Ti-O-Cu, respectively. The authors suggested that Cu<sup>2+</sup> ions were reduced to Cu<sup>0</sup> at the cathode and then oxidized to CuO during the drying step (seen by Cu 2p<sub>3/2</sub> and Cu 2p<sub>1/2</sub> (935.1 and 955.1 eV, respectively). The Ti-O-N and Ti-O-Cu were mostly likely formed from ion exchanges between Ti<sup>4+</sup> and N and Ti<sup>4+</sup> and Cu<sup>2+</sup>, respectively. Interstitial nitrogen atoms were seen in the N 1s spectra and were located in the band gap between the VB and the CB (Fig. 44).

The photodecomposition of dibenzothiophene (DBT), diluted in isooctane (0.6–1.0 g/L), was used to test the activity of the catalysts (Table 21). The activity increased with Cu loading from 5 to 10 wt% but decreased at higher Cu loadings. Effects due to the Cu, N, and V<sub>o</sub> were attributed to capturing photo-generated electrons from the CB and decreased the rate of electron–hole recombinations. The higher Cu loadings (i.e., 15 and 20 wt%) were thought to block light, inhibiting the catalyst performance. The 10 wt% Cu loading performed the best in the UV experiments but was only  $\sim 5 \times 10^{-3}$  mM/min slower than the 15 wt% catalyst in the visible range experiments. This phenomenon also followed the lower bandgap energy for the 15 wt% vs 10 wt% Cu loading (2.76 vs 2.48 eV, respectively) (113).

Liu *et al.* investigated the role of copper addition and heat treatment (air, helium, and hydrogen) on the visible light reaction of CO<sub>2</sub> on TiO<sub>2</sub> (Table 22). Copper (0.05 M CuCl<sub>2</sub> aqueous) was added to P25 (0.25 M NaOH aqueous) via precipitation and then calcining in air at 400 °C for 2 h. Atomic ratios Cu:Ti were 1% and 5%. Pretreatment was accomplished in situ by flowing He or H<sub>2</sub> through reactor at 220 °C for 1.5 h. The intent of pretreatment was to increase the number of oxygen vacancies and to reduce Cu<sup>2+</sup> to Cu<sup>+</sup> and Cu<sup>0</sup> (114).

UV–vis diffuse reflectance showed an absorption educe of 420 cm<sup>-1</sup> for the 1% Cu/Ti(UP) and then a red-shift for the 1% Cu/Ti(He) and 1% Cu/Ti(H<sub>2</sub>) catalysts, owing to a narrowed bandgap energy for the He and H<sub>2</sub> treated samples. DRIFTS showed a disappearance of the OH stretching bands (3693 and 3635 cm<sup>-1</sup>) of the treated (both He and H<sub>2</sub>) vs untreated. In addition, a new shoulder emerged at 3717 cm<sup>-1</sup> and was attributed to Ti<sup>3+</sup>–OH. These results indicated that unpretreated Cu/TiO<sub>2</sub> had few, if any, defects and would most likely not be a good choice for CO<sub>2</sub> reduction. XPS results were similar as those reported for Cu on amorphous TiO<sub>2</sub>. Since XPS cannot adequately distinguish between Cu<sup>+</sup> and Cu<sup>0</sup>, CO adsorption was measured via in situ DRIFTS. Cu<sup>0</sup>–CO, Cu<sup>+</sup>–CO, Ti<sup>4+</sup>–OH–CO, and Ti<sup>4+</sup>–CO were identified at 2097, 2112, 2160, and



**Fig. 44** (A) XPS spectra of Ti 2p (a) AT and (b) 10 CAT, (B) O 1s (a) AT and (b) 10 CAT, (C) Cu 2p, (D) C 1s and, (E) N 1s of 10 CAT (113).

**Table 21** CuO/TiO<sub>2</sub> photocatalyst characteristics (113).

Catalyst	BET surface area (m <sup>2</sup> /g)	Pore volume (cm <sup>3</sup> /g)	Bandgap energy (eV)	Initial rate of UV light photooxidation (10 <sup>-3</sup> mM/min) <sup>a</sup>	Initial rate of visible light photooxidation (10 <sup>-3</sup> mM/min)
AT <sup>b</sup>	402	0.451	3.16	0.7	0.5
5 CAT <sup>c</sup>	124	0.137	2.95	2.0	2.4
10 CAT	104	0.134	2.76	4.6	3.9
15 CAT	93	0.113	2.48	1.9	4.4
20 CAT	141	0.186	2.43	—	1.9
CuO	2	0.008	1.55	—	—

<sup>a</sup>Photooxidation rates (both UV and Visible light) approximated from graphs.<sup>b</sup>AT: Amorphous TiO<sub>2</sub>.<sup>c</sup>CAT: Copper Amorphous TiO<sub>2</sub> (preceding number indicates wt% CuO).**Table 22** 1% Cu/TiO<sub>2</sub> photocatalyst characteristics (114).

Catalyst	BET surface area (m <sup>2</sup> /g)	Pore volume (cm <sup>3</sup> /g)	Bandgap energy (eV)	Surface atomic ratio (Cu/Ti) <sup>a</sup>	CO production (μmol/g <sub>cat</sub> ) <sup>b</sup>	CH <sub>4</sub> production, (μmol/g <sub>cat</sub> ) <sup>b</sup>
1% Cu/Ti(UP) <sup>c</sup>	51.1	0.246	3.04	0.035	2.7	0.2
1% Cu/Ti(He)	52.4	0.315	2.85	0.025	11	0.5
1% Cu/Ti(H <sub>2</sub> )	53.7	0.321	2.89	0.023	25	4.4

<sup>a</sup>Measured by XPS.<sup>b</sup>Production determined by integrating the production rate (μmol/g<sub>cat</sub>/h) over the 6.5 h time of experiment for the 1% Cu catalysts.<sup>c</sup>UP = Unpretreated, He = thermal pretreatment at 220 °C for 1.5 h under flowing helium, H<sub>2</sub> = thermal pretreatment at 220 °C for 1.5 h under flowing hydrogen.

2182 cm<sup>-1</sup>, respectively. The signature at 2097 cm<sup>-1</sup> appeared as a shoulder and was only seen for the H<sub>2</sub> treated Cu/TiO<sub>2</sub> (114)

Raguram and Rajini point out that TiO<sub>2</sub> can behave both as a semiconductor and as a magnetic material by what they termed as diluted magnetic semiconductors (DMS) (115). This dual role can be governed through electric charge and electron spin properties. Using a sol–gel synthesis technique, titanium tetraisopropoxide was added to DI water and isopropanol for 1 h.



Nitric acid was added (pH not provided) and stirred vigorously for 45 min before drying at 80 °C for 5 h. The material was annealed at 300 °C for 3 h to produce anatase TiO<sub>2</sub> (according to the XRD). To produce Ni or Cu-doped TiO<sub>2</sub>, nickel nitrate hexahydrate or copper nitrate hexahydrate was diluted in water (0.3 M) and then added to the TiO<sub>2</sub>.

X-ray Diffraction (Fig. 45 (left)) shows a CuO (002) and CuO (112) formation at  $\sim 36^\circ$  and  $38^\circ$ , respectively, for the Cu/TiO<sub>2</sub>. The two planes (110) and (103) for the Ni/TiO<sub>2</sub> were attributed to anatase. The addition of Ni or Cu did not alter the tetragonal phase of the anatase but slightly shift the (101) plane to a lower angle due to ionic radii of the dopants (0.69 Å for Ni<sup>2+</sup> and 0.73 for Cu<sup>2+</sup>). The Kubelka–Monk plot (Fig. 45 (right)) shows a remarkable decrease in bandgap energy for the doped materials. The bandgap values were 3.25, 2.48, and 1.25 for TiO<sub>2</sub> (undoped), Ni/TiO<sub>2</sub>, and Cu/TiO<sub>2</sub>, respectively. This decrease in bandgap energies was attributed to the formation of sub-band states of Ni<sup>2+</sup> and Cu<sup>2+</sup> and oxygen vacancies. The photoluminescence emission spectra (Fig. 46) shows a charge transfer from Ti<sup>3+</sup> to oxygen anion (468–471 nm), yielding [TiO<sub>6</sub>]<sup>8-</sup>, indicating the origination of the bands from the intrinsic state, not from the surface sites (115).

#### 9.4 Microwave, ionic liquid, and combined microwave/ionic liquid methodologies

Beyond the more typical synthesis routes for TiO<sub>2</sub> includes microwave assisted, use of ionic liquids (ILs), and combined microwave/ionic liquid methodologies. The need is for low bandgap materials (i.e., rutile) but with high surface area (i.e., anatase). To improve the surface area of rutile, Huang and Chien tested microwave irradiation on rutile powders that had been dispersed in 10 M NaOH (116). The resulting material was rutile nanorods (listed at Tnt in Table 23) whose inner diameters ranged 3–5 nm and outer diameters ranged 8–10 nm and had a 100-fold increase in surface area compared to the rutile powder. While a bandgap energy was not provided, the UV–Vis spectra indicated a slight “blue shift.” Upon calcining at 300 °C in the presence of H<sub>2</sub>, the material exhibited a light gray-blue color, which the authors attributed to the formation of oxygen vacancies. These oxygen vacancies were hypothesized to create sub-bands with energy states located below the conduction band (Fig. 47). The three types of oxygen vacancy energy states appear to be O<sub>v</sub><sup>++</sup>, [O<sub>v</sub>••Ti<sup>3+</sup>], and [O<sub>v</sub>••2Ti<sup>3+</sup>].

Conversions of NO under visible light was in the order Rutile/Tnt > P25 > rutile, 95.0, 53.6, and 45.5, respectively. The same order was

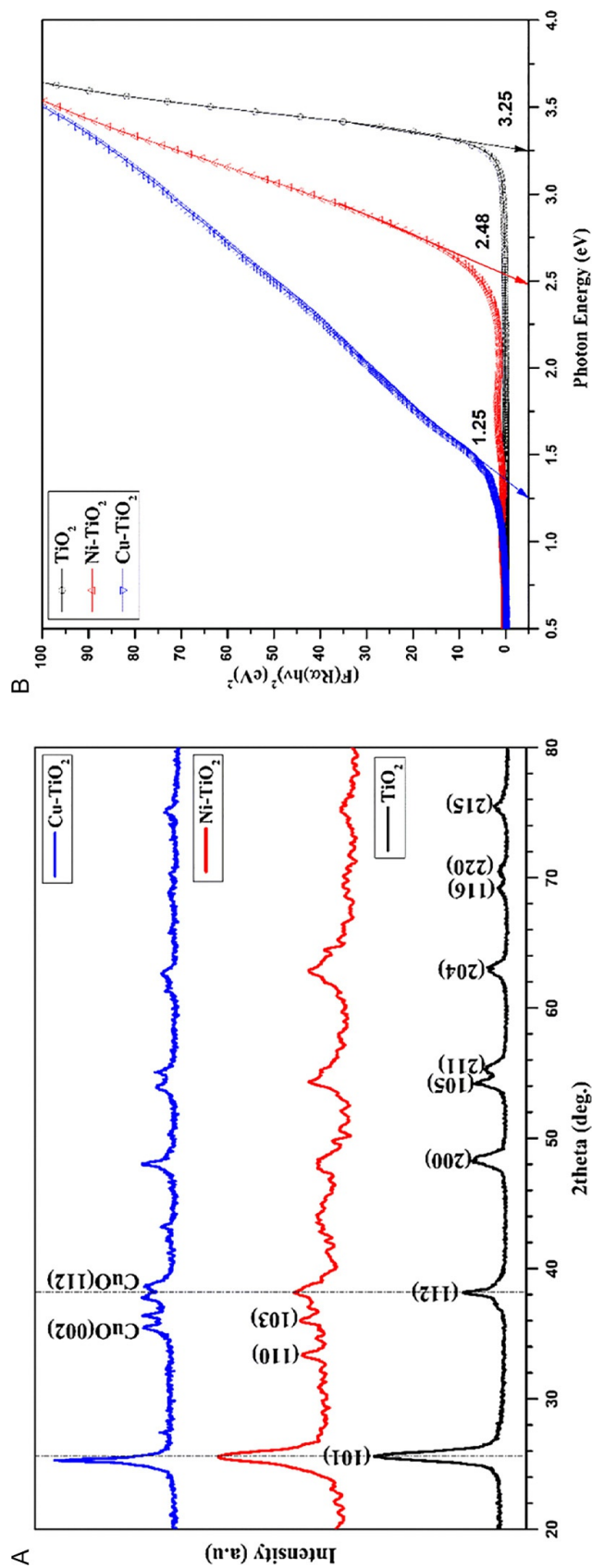


Fig. 45 (left) X-ray diffraction and (right) Kubelka-Munk plot of TiO<sub>2</sub>, Ni-TiO<sub>2</sub>, and Cu-TiO<sub>2</sub> nanoparticles (115).

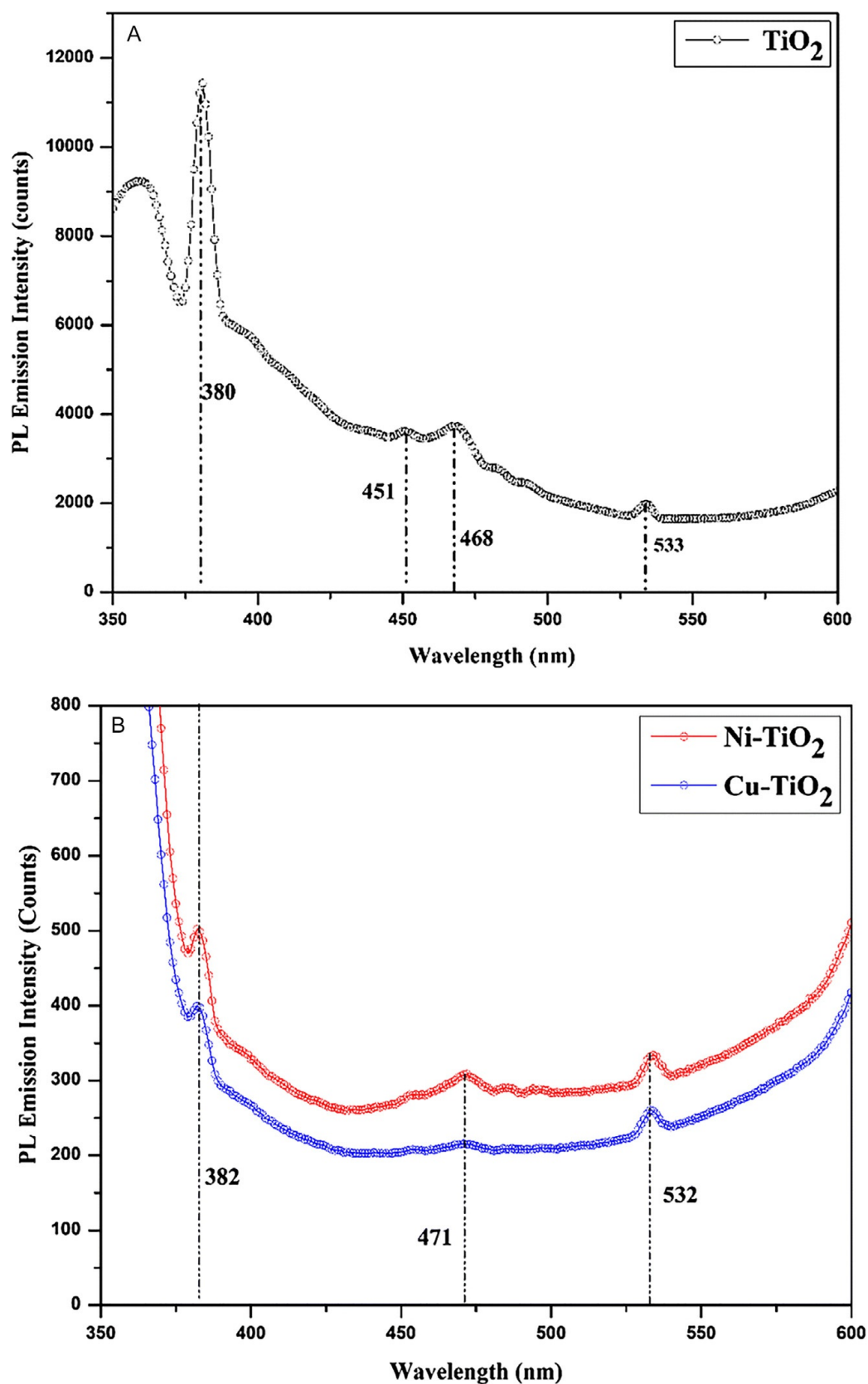
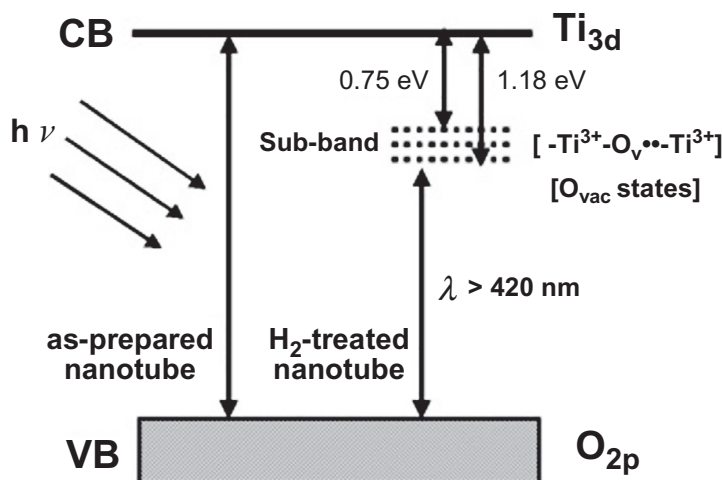


Fig. 46 Photoluminescence spectra of (A)  $\text{TiO}_2$  and (B)  $\text{Ni-TiO}_2$ , and  $\text{Cu-TiO}_2$  nanoparticles (115).

**Table 23** Preparation, characterization, and testing of TiO<sub>2</sub> prepared with microwave, ionic liquid, and combined microwave/ionic liquids (116–118).

Methodology	Catalyst	BET surface area (m <sup>2</sup> /g)	Pore volume (cm <sup>3</sup> /g)	Bandgap energy (eV)	Reaction rate constant (h <sup>-1</sup> )
Microwave assisted <sup>a</sup>	Rutile	~2	–	–	0.108 <sup>b</sup>
	P25	–	–	–	0.244
	Rutile/Tnt	214	0.86	–	0.591
Ionic liquid template <sup>c</sup>	Anatase/NaCl	154	0.37	–	1.788 <sup>d</sup>
	Anatase/CaCl <sub>2</sub>	199	0.60	–	1.326
	Anatase/NH <sub>4</sub> Cl	183	0.79	–	2.748
	Anatase/NH <sub>4</sub> NO <sub>3</sub>	170	0.82	–	2.28
Microwave/IL combined <sup>e</sup>	Anatase/[Bmim][BF <sub>4</sub> ]	98	0.26	3.12	
	Anatase/[Bmim][Cl]	129	0.33	3.20	
	Anatase/[Bmim][BF <sub>4</sub> ] <sup>f</sup>	94	0.23	3.05	

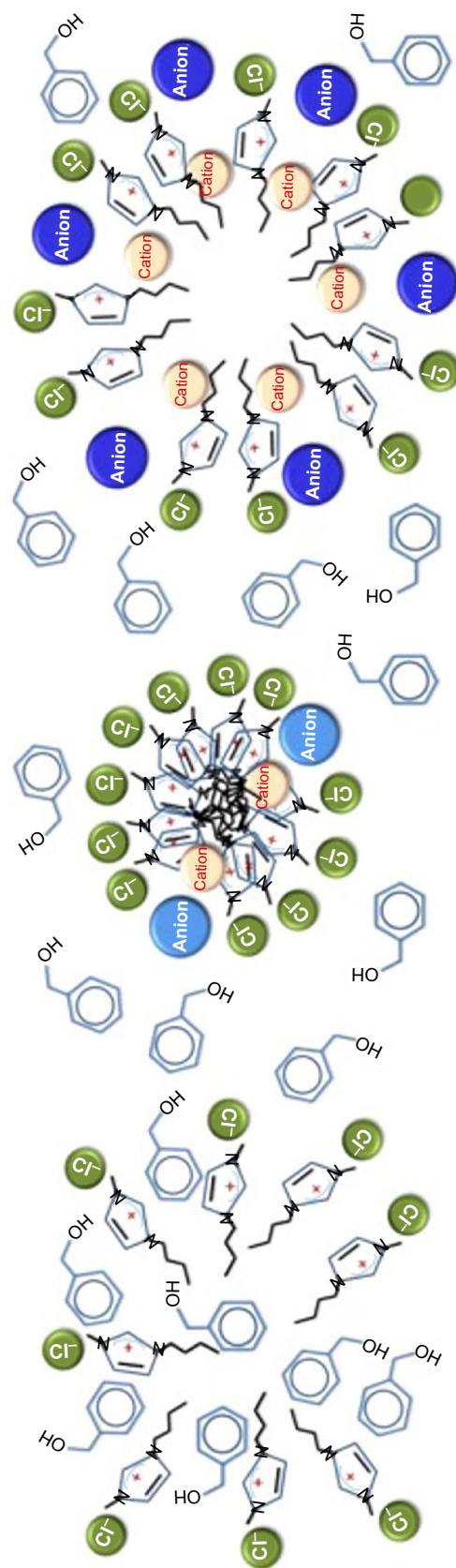
<sup>a</sup>Titania nanorods prepared from rutile powder under microwave irradiation at 200 °C.<sup>b</sup>Visible light photodegradation of NO light at 30 °C.<sup>c</sup>TiO<sub>2</sub> prepared using sol–gel process containing titanium tetra-isopropoxide and 1-butyl-3-methylimidazolium chloride ([C<sub>4</sub>mim][Cl]).<sup>d</sup>UV light photodegradation of bisphenol A.<sup>e</sup>TiO<sub>2</sub> prepared using sol–gel process containing titanium (IV) tetrabutoxide under microwave irradiation at 150 °C and calcined at 200 °C.<sup>f</sup>Calcined at 200 °C under vacuum.**Fig. 47** Energy diagram for rutile nanotube heat treated (300 °C) under H<sub>2</sub> atmosphere (116).

followed under natural solar light with conversions of 100, 96.1, and 63.3, respectively. The reaction rates also followed this same pattern and are presented in Table 23. It was theorized that mid-gap energy states, located below the conduction band, are formed when the material is heat treated with  $H_2$  resulting in the narrowing of the bandgap. In this scenario, visible light energy excites an electron from the oxygen vacancy (Fig. 47) (116). Under cyclic conditions, there was a still >90% conversion of NO and >50%  $N_2$  selectivity after 3 reaction cycles. The Tnt photocatalysts were also effective for converting methylene blue. The authors proposed that the high surface areas ( $214\text{ m}^2/\text{g}$ ) and tubular structure promoted diffusion of methylene blue reactants.

In another attempt to tailor pore sizes of ion liquid-templated  $TiO_2$  catalysts, inorganic salts were studied as auxiliary agents since their interactions with benzyl alcohol, a hydrophobic solvent, could aid in the self-assembly of 1-n-butyl-3-methylimidazolium chloride ( $[C_4mim][Cl]$ ), a hydrophilic ionic liquid (IL), to form micellular aggregates (117). The UV photodegradation of bisphenol A was carried out on a  $TiO_2$  anatase produced using an IL but in the presence of differing salts (i.e., NaCl,  $CaCl_2$ ,  $NH_4Cl$ , and  $NH_4NO_3$ ). Physically, the salt templating increased the pore diameter of the catalyst compared unmodified  $TiO_2$ . The order being  $TiO_2 < NaCl < CaCl_2 < NH_4Cl < NH_4NO_3$  with pore diameters of 4.2, 8.7, 12.4, 13.7, and 16.8 nm, respectively. A micelle-like mechanism was used to describe the interactions between the salts, ILs, and titanium precursor (Fig. 48) where larger ionic radii produced larger pore sizes. The ionic radii were 95, 99, 148, 181, and 264 pm for  $Na^+$ ,  $Ca^{2+}$ ,  $NH_4^{4+}$ ,  $Cl^-$ , and  $NO_3^-$ , respectively. Noncovalent interactions, such as with  $\pi$ - $\pi$  stacking, between the butyl alcohol chains and the  $[C_4mim][Cl]$  assisted in the self-assembly process. Addition of phosphoric acid increased the ionic strength of the solution and promoted the separation of the IL from the butyl alcohol, creating more well-defined, denser aggregates. The growth of colloids is then hindered due to a chelation effect of the phosphate ions to the  $Ti^{4+}$  centers. Therefore, a high-quality templating effect is realized, and pore sizes can be manipulated.

Activity tests revealed that pore size tailoring effected the reaction rate. Although the bandgap energies of each catalyst were not provided, the range of measured bandgaps was 3.12–3.30 eV, measured using DRIFTS. Since these are fairly large bandgap energies, the authors suggest that mid-gap energy states may be present. The pseudo-first order rate constants for the salt-assisted photocatalysts were on the order of  $NH_4Cl > NH_4NO_3 > NaCl > CaCl_2 > TiO_2$  with rate constants (in  $\text{min}^{-1}$ )





The  $\pi$ - $\pi$  stacking and non-covalent interactions between the imidazolium cations drive the self-assembly of  $C_4\text{mimCl}$  molecules in the BA medium.

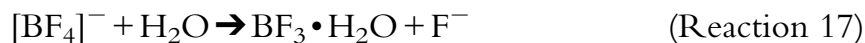
Small amounts of salts improve the phase separation and shrink the IL-aggregates.

The salts swell the IL-aggregates upon volume exclusion and Coulomb repulsion at high concentrations.

**Fig. 48** Self-assembly of ionic liquid in butyl alcohol medium with salt effects (117).

$4.58 \times 10^{-2}$ ,  $3.8 \times 10^{-2}$ ,  $2.8 \times 10^{-2}$ ,  $8.30 \times 10^{-3}$ , respectively. Further analysis revealed poor crystallinity and salt contaminations (i.e.,  $\text{Ca}_3(\text{PO}_4)_2$  and  $\text{NaPO}_3$ ) of the catalysts but all had higher reaction activities than the synthesized  $\text{TiO}_2$  with pore size tailoring (117).

When microwave irradiation was combined with ILs (in this case  $[\text{Bmim}][\text{BF}_4]$  and  $[\text{Bmim}][\text{Cl}]$ ), hollow structured  $\text{TiO}_2$  nanocrystals were formed (118). The intent was to take advantage of the formation of localized “hot spots” (or superheating) that occur from microwave irradiation. This superheating within the aqueous solution leads to nucleation and crystal growth throughout the bulk solution. Under microwave irradiation, the boiling temperature of the IL is rapidly achieved, and the  $\text{F}^-$  ion dissociates, creating a fluorine ion-rich system.



Interestingly, the bandgap energy of the  $\text{TiO}_2$  produced with  $[\text{Bmim}][\text{Cl}]$  was larger than P25 (3.2 vs 3.15 eV). And, that of the  $[\text{Bmim}][\text{BF}_4]$  (3.12 eV) was not significantly different. If the material, however, was subjected to calcination under vacuum, a bandgap of 3.05 eV could be realized.  $\text{Ti}^{3+}$  sites were detected by EPR in the sample produced using  $[\text{Bmim}][\text{BF}_4]$  under vacuum. Physically, wormhole-like structures were synthesized using the microwave/IL synthesis method. Activity tests were conducted using visible light from a 300 W xenon lamp. Reaction results showed that selective oxidation of benzyl alcohol, using  $\text{Ti}^{3+}$  sites, to benzaldehyde and the photodegradation of methylene blue were made easier due to the wormhole formations, owing to better diffusion rates. The trend in yield of benzaldehyde was  $\text{Anatase}/[\text{Bmim}][\text{BF}_4]_{\text{vacuum}} > \text{Anatase}/[\text{Bmim}][\text{BF}_4] \gg \text{P25} > \text{Anatase}/[\text{Bmim}][\text{Cl}]$ . In subsequent experiments, the molar ratio of  $[\text{Bmim}][\text{BF}_4]$  to Ti was adjusted (0–5). Catalytically, at ratio of 2 performed far superior than other tested mixtures in both the benzyl alcohol and methylene blue reactions (118).

## 9.5 $\text{TiO}_2$ (B): The fourth polymorph of $\text{TiO}_2$

$\text{TiO}_2$  (B) has gained a great deal of interest in energy storage applications, particularly as an electrode material for rechargeable Li ion batteries.  $\text{TiO}_2$  (B) has an open structure consisting of large continuous channels that are well suited for intercalation and is the least dense of all the polymorphs.  $\text{TiO}_2$  (B) is the primary constituent of titania nanotubes; however, there have been few theoretical studies (structural and vibrational) for  $\text{TiO}_2$  (B) (119).

Although its photocatalytic activity has been noted to be lower than anatase,  $\text{TiO}_2$  (B) when combined with anatase has shown to provide photocatalytic activity. The composite material shows a unique positioning of the valence and conduction bands.  $\text{TiO}_2$  (B) has its CB located above the CB of anatase, and the VB of  $\text{TiO}_2$  (B) is positioned in the energy gap of anatase, creating a Type II heterojunction similar to anatase and rutile mixtures. This Type II heterojunction promotes charge migration and separation. Yang *et al.* synthesized a composite core-shell fibril structure consisting of  $\text{TiO}_2$  (B) fiber anchored with anatase nanocrystals (120). The catalyst structure had anatase forming interfaces with a  $\text{TiO}_2$  (B) fibril core. The synergistic composite material exhibited superior photocatalytic activity over Degussa P-25 in degradation of the organic dye sulfo-rhodamine B (SRB). The synergism comes from  $\text{TiO}_2$  (B) crystals providing excellent mechanical properties simultaneously with anatase providing good electron traps. Anatase has a strong ability to adsorb oxygen molecules which in turn captures electrons and reduces recombinations of electron and hole. The placement of the band energies of anatase and  $\text{TiO}_2$ (B) provides for efficient charge carrier migration with photogenerated holes moving from the anatase outer shell to the core of  $\text{TiO}_2$  (B) while the electrons travel from  $\text{TiO}_2$  (B) to anatase. The superior photocatalytic activity was also attributed to the structural factors of the catalyst with interfaces playing the major role. The interface is an important structural component while synthesizing mixed phase composites for good electron-hole migration and separation (119).  $\text{TiO}_2$ (B)/anatase provided a well-matched phase interface. Similar inferences were studied by Li *et al.* for photocatalytic oxidation of iodide using anatase/ $\text{TiO}_2$  (B) core-shell nanofiber (121), by Liu *et al.* using synthesized  $\text{TiO}_2$  (B)/anatase core-shell heterojunction nanowires for the photodegradation of methyl orange solution (122), and by Voepel *et al.* using synthesized multiphase  $\text{TiO}_2$ (B)/anatase nanoparticle heterojunctions using ionic liquids to produce hydrogen from water-methanol mixtures (49). For all the reasons mentioned above (i.e., the narrow band gap, the specific conduction, and valence band edge potential of  $\text{TiO}_2$  (B) creating a good heterojunction when combined with anatase promoting charge migration and separation) photocatalytic reactions have been carried out using  $\text{TiO}_2$  (B) and anatase mixtures in the areas of organic pollutant degradation. However, the research on implementing  $\text{TiO}_2$  (B) in  $\text{CO}_2$  photoconversion is not available at this time.

The unique crystal structure of  $\text{TiO}_2$ (B) has led to it being implemented in photocatalysis and electrocatalysis. One of the major disadvantages of  $\text{TiO}_2$  (B) is its metastable nature with its transformation into anatase and

rutile at high temperatures. Wang *et al.* was able to restrict its conversion to anatase by using HF as structure-controlling agent even at high temperatures. This technique was able to maintain the TiO<sub>2</sub> (B) phase even at 750 °C. The reason reported was that the adsorption of F<sup>+</sup> ions onto the TiO<sub>2</sub> (B) surface leads to the reduction of the surface energy from 0.63 J/m<sup>2</sup> on a clean surface to −0.22 J/m<sup>2</sup> when treated with HF causing the restriction of the phase change. This technique can be implemented in synthesizing TiO<sub>2</sub>(B)/anatase heterojunctions even at high temperatures as high as 750 °C for application in CO<sub>2</sub> photoreduction, hydrogen production, and pollution degradation (123).

## 9.6 Hybrid photocatalysts constituting of TiO<sub>2</sub> and their respective defects

ZnO, MgO, and BiOBr are among the other extensively studied photocatalysts alongside TiO<sub>2</sub> because of their low-cost, high stability, nontoxic nature, and unique photocatalytic efficiencies. TiO<sub>2</sub> when combined with ZnO, MgO and BiOX (where X is Cl or Br) forms hybrid nanocomposite photocatalysts. These hybrid photocatalysts have been reported to perform better than semiconductors used in their pure forms, usually in the degradation of organic pollutants, that has been attributed to long term separation of charge carriers (125). Coupling semiconductor such as ZnO, MgO, and BiOX having conduction band gap edges placed in varying positions with TiO<sub>2</sub> creates heterojunctions leading to “built-in” potential gradients at the junction or interface producing efficient charge separation and interfacial charge transfers (126). For example, the heterojunction formed between ZnO and TiO<sub>2</sub> semiconductor is shown in Fig. 15. (83). When the light falls on ZnO, the photon energy excites the electron from VB of ZnO to its CB leaving behind a hole in the VB. Due to the potential difference between the conduction bands of both the semiconductors (Fig. 49), the electrons from CB of ZnO flow to the CB of TiO<sub>2</sub>. In a similar way, the holes flow from TiO<sub>2</sub> to ZnO (124).

Nanostructured TiO<sub>2</sub>-ZnO hybrid photocatalyst was shown to convert CO<sub>2</sub> in the presence of water to CH<sub>4</sub> by Wu *et al.* When in comparison with pure TiO<sub>2</sub>, the hybrid gave a fivefold increase in conversion of CO<sub>2</sub> to CH<sub>4</sub>, with pure TiO<sub>2</sub> forming 0.55 μmol/g<sub>cat</sub> h methane and TiO<sub>2</sub>-ZnO hybrid forming 2.56 μmol/g<sub>cat</sub> h methane (127). Xi *et al.* reported the photo-conversion of CO<sub>2</sub> to CH<sub>4</sub> was five or sixfold greater for TiO<sub>2</sub>/ZnO hybrids than commercial P-25 (128). TiO<sub>2</sub>/ZnO generated 55 μmol/g<sub>cat</sub> h of methane, whereas P-25 using the same experimental conditions produced

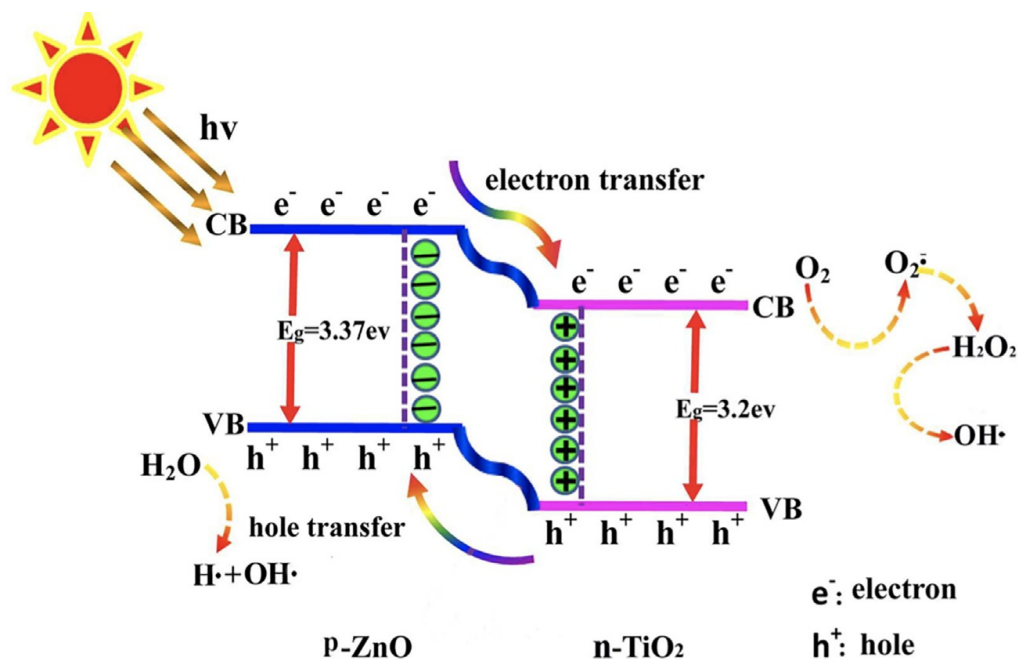


Fig. 49 The heterojunction formed between ZnO and TiO<sub>2</sub> (124).

9.3  $\mu\text{mol/g}_{\text{cat}}$  h of methane. The authors concluded that the increase was due to the increase in electron mobility in the hybrid. TiO<sub>2</sub>/ZnO has an electron mobility of 205–300  $\text{cm}^2/\text{VS}$  (Degussa P 25 has 0.1–1  $\text{cm}^2/\text{VS}$ ). Also, the hybrid has a much higher surface area (225  $\text{m}^2/\text{g}$ ) compared to P25 (50  $\text{m}^2/\text{g}$ ). The most significant aspect being reduced charge carrier recombinations due to the interface heterojunction between ZnO-TiO<sub>2</sub> (128).

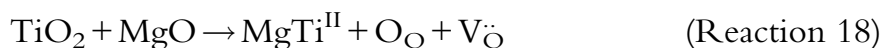
Mazabuel-Collazos *et al.* studied defects (oxygen vacancies, oxygen interstitials, zinc vacancies, and zinc interstitials) on ZnO-TiO<sub>2</sub> nanocomposites. Combining ZnO and TiO<sub>2</sub> led to the substitution of  $\text{Zn}^{2+}$  with  $\text{Ti}^{4+}$  since the ionic radius of  $\text{Ti}^{4+}$  (0.61 Å) is smaller than  $\text{Zn}^{2+}$  (0.74 Å). There is a displacement of  $\text{Zn}^{2+}$  ions located in their regular structure to free surfaces causing zinc vacancy or interstitial defects in ZnO-TiO<sub>2</sub> hybrid materials (128). The synthesis method (ball milling of TiO<sub>2</sub> in H<sub>2</sub>O solution doped with p-ZnO) also led to the crystal lattices of TiO<sub>2</sub> undergoing severe plastic deformation of the crystal lattice. The role of such defects present in TiO<sub>2</sub>-ZnO in CO<sub>2</sub> conversion is yet to be studied (129).

BiOBr is a p-type semiconductor known for its unique photocatalytic efficiency. The as-synthesized TiO<sub>2</sub> nanotube coupled with BiOBr has higher photocatalytic activity than P25 in sunlight for organic molecules (130). Deng *et al.* synthesized mesoporous TiO<sub>2</sub>-BiOBr microspheres

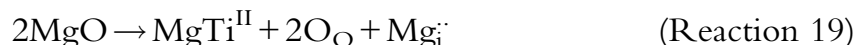


where it was suggested that doping Ti atoms into BiOBr could introduce defects in BiOBr crystal structures (131). Wang *et al.* constructed amorphous TiO<sub>2</sub>/BiOBr heterojunctions by coupling the (001) facets of TiO<sub>2</sub> and BiOBr. The (001) facet of the BiOBr photocatalyst is said to provide efficient electron–hole separations. Creating heterojunctions on such (001) facets can prove to be more productive. The amorphous TiO<sub>2</sub> implemented had solid-state defect levels which provided a photo-induced charge transfer route. In other words, the photogenerated electrons of BiOBr were easily transferred to the defect levels of amorphous TiO<sub>2</sub> leaving behind more holes in the VB of BiOBr, which then increased the separation efficiency of photogenerated charges (132).

Photocatalytic reduction of CO<sub>2</sub> to methane with water as a reductant using TiO<sub>2</sub>-MgO nanotube hybrid was studied by Li *et al.* (133). The MgO plays a critical role in methanation of CO<sub>2</sub> as it has a strong adsorption ability for CO<sub>2</sub> forming magnesium carbonate. TiO<sub>2</sub> nanotubes, on the other hand, play an important role by providing a large BET surface area, strong adsorption ability, and efficient utilization of light. These are not properties that are found in MgO. The other most significant attribute of this hybrid is that the MgO covered on TiO<sub>2</sub> prevents CO or CH<sub>4</sub> from contacting TiO<sub>2</sub>. This prevents the re-oxidizing of CO<sub>2</sub> and CH<sub>4</sub>. Liu *et al.* also performed photoconversion of CO<sub>2</sub> to CO using MgO patched TiO<sub>2</sub> microsphere (134). The photocatalyst hybrid showed good stability in photoreaction when compared to TiO<sub>2</sub>. The production of CO decreased rapidly after an hour with TiO<sub>2</sub>. The hybrid, on the other hand, had a higher stability whose CO production slowly decreased after 4 h. Furthermore, the hybrid showed a fourfold increase in the activity of the temperature range of 120–150 °C when compared to bare TiO<sub>2</sub> (98). Synthesizing TiO<sub>2</sub>-MgO mixed oxides through a sol–gel method gave rise to structural defects according to Lopez *et al.* (135). Similar to Ti<sup>4+</sup> substitution in the places of Zn<sup>2+</sup> in TiO<sub>2</sub>-ZnO hybrid photocatalyst, in TiO<sub>2</sub>-MgO, Mg<sup>2+</sup> becomes substituted by Ti<sup>4+</sup> ions, creating vacancies in the titania lattice that leads to structural defects (i.e., titania vacancies and titanium interstitials). Reactions 17 and 18 describe the formation of other defects, including oxygen vacancies and magnesium interstitials formed. One of the main goals to defect formation is to maintain charge neutrality in the catalyst hybrids. The importance of defects of MgO and TiO<sub>2</sub> combination in CO<sub>2</sub> photoconversion has not been well studied at this time.



where  $V_{\text{O}}^{\bullet}$  represents an oxygen vacancy.



where  $\text{Mg}_{\text{i}}^{\bullet\bullet}$  represents a magnesium interstitial.

## 9.7 Summary of defect synthesis methods

Black TiO<sub>2</sub> defect synthesis methods have centered largely on sol–gel preparation and heat treatment approaches. For the sol–gel systems, titania precursors and various surfactants have been the most tested parameters, whereas calcination temperatures (200–700 °C) and atmospheres (i.e., air, He, and H<sub>2</sub>) have been the focus for heat treatments. Unfortunately, band gap energies for many of the black TiO<sub>2</sub> have not been reported, making a true comparison with DFT results difficult. Annealing of TiO<sub>2</sub> up to 600 °C under H<sub>2</sub> atmosphere gave reasonable physical and optical results with absorption energies in the visible region. Temperatures above 600 °C saw a sharp increase in crystal size and a collapse in the BET surface area, making the material less effective as a catalyst.

Doping of TiO<sub>2</sub> with metals can lead short band gap energies but often at the expense of creating mid-gap energy states that negatively impact electron–hole recombinations. Composite materials, such as nickel oxides or copper oxides combined with TiO<sub>2</sub>, offer a solid compromise through electron scavenging mechanisms. The art lies in the preparation procedures to provide intimate contact between the two (or more) types of materials such that a valence band electron can be excited by a photon and effectively transfer across the heterojunction.

Ionic liquid templated, microwave assisted synthesis method produced titanium nanorods which could be ideal for moving reactants through the porous solid. Pore sizes can be readily tailored using inorganic salts. There different types of oxygen vacancy energy states were formed due to the localized heating effect of microwave irradiation. However, no information could be found toward optimization of either the inorganic salts (i.e., salt concentrations or salt mixtures) or microwave parameters (i.e., wavelength or irradiation time).



## 10. CO<sub>2</sub> Photocatalytic conversions using TiO<sub>2</sub>

While most of the experimental research has focused on conversion of organic compounds (i.e., dyes), there has been much work toward the

conversion of CO<sub>2</sub>. From both the DFT studies and the TiO<sub>2</sub> synthesis efforts, a few major points of interest emerge. The development of catalyst surfaces with (1) oxygen vacancies, (2) lower bandgap energies, and (3) increased electron–hole–recombination times are among the most significant. Thermal treatment and addition of dopant elements appear to be the pathways studied by most to achieve these desired qualities. Prior to being adsorbed onto the TiO<sub>2</sub> surface, it is believed that CO<sub>2</sub> must be activated via photogenerated electrons (CO<sub>2</sub><sup>−</sup>) (136–138). As was shown from DFT calculations, CO<sub>2</sub> adsorbs via a bent geometry onto Ti<sup>3+</sup> sites rather than its normal linear geometry. Indeed, the reduction of CO<sub>2</sub> using H<sub>2</sub>O must overcome the Gibbs free energy barrier (Table 24) to produce commonly accepted valued-added products (139).

### 10.1 Conversion of CO<sub>2</sub> on unsupported TiO<sub>2</sub>

Photocatalytic activity for Cu-doped TiO<sub>2</sub> by Liu *et al.* consisted of continuously passing CO<sub>2</sub> saturated with H<sub>2</sub>O vapor through a reactor (2 mL/min) using a 150 W (90 mW/cm<sup>2</sup>, 200–1000 nm wavelength) light (114). Production of CO and CH<sub>4</sub> were monitored throughout each experiment. Once irradiated, the catalysts deactivated after ~6.5 h (Fig. 50). Mechanistically, the authors point toward a decrease in the Cu<sup>+</sup>–CO band (observed via in situ DRIFTS), indicating conversion of Cu<sup>+</sup> to Cu<sup>2+</sup>. Since Cu<sup>+</sup> is hypothesized to be a hole scavenger, a decline in reactivity would be expected. Integrating the production rate over time revealed that CO production was 4 to 1 for the helium pretreatment vs unpretreated catalyst, and 2.27 to 1 when hydrogen pretreatment was compared to helium

**Table 24** Gibbs free energy for conversion of CO<sub>2</sub> to value-added products (adapted from figure) (119).

Reaction	Gibbs free energy (kJ/mol)
CO <sub>2</sub> → CO + 1/2O <sub>2</sub>	257
CO <sub>2</sub> + H <sub>2</sub> O → HCOOH + 1/5O <sub>2</sub>	286
CO <sub>2</sub> + H <sub>2</sub> O → CH <sub>2</sub> O + O <sub>2</sub>	522
CO <sub>2</sub> + 2H <sub>2</sub> O → CH <sub>3</sub> OH + 3/2O <sub>2</sub>	703
CO <sub>2</sub> + 2H <sub>2</sub> O → CH <sub>4</sub> + 2O <sub>2</sub>	818

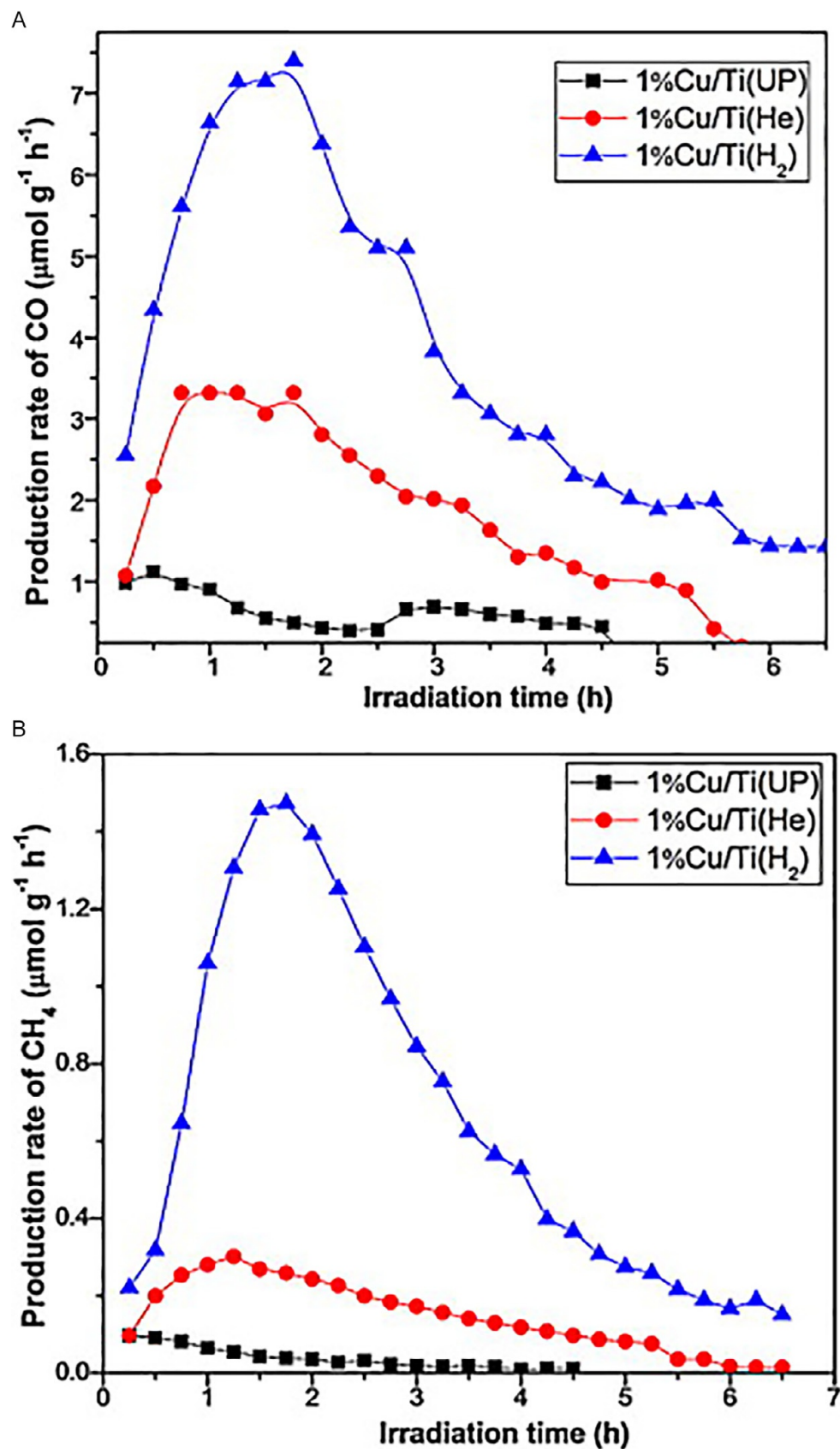


Fig. 50 Production rate of (A) CO and (B)  $\text{CH}_4$  for 1%Cu/Ti catalysts (114).

pretreatment. The production of  $\text{CH}_4$  was always lower than  $\text{CO}$ , most likely due to fact that methane requires eight electrons to two for carbon monoxide. Decoupling the effects of pretreatment vs Cu addition revealed Cu enhanced both  $\text{CO}$  and  $\text{CH}_4$  production since Cu hinders electron–hole recombinations by trapping electrons.

To differentiate between the effects of copper species and defect sites, an enhancement factor,  $F$ , was determined from the normalized productions of  $\text{CO}$  and  $\text{CH}_4$ .

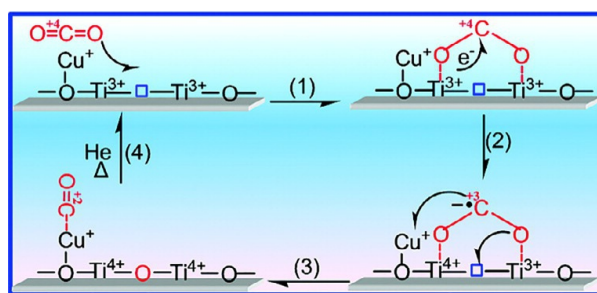
$$F_{\text{Cu}} = Y_{\text{Cu}}/Y_{\text{Ti(UP)}} \quad (6)$$

$$F_{\text{D}} = Y_{\text{Ti(He)}}/Y_{\text{Ti(UP)}} \quad (7)$$

where  $F_{\text{Cu}}$  is the enhancement due to Cu species,  $F_{\text{D}}$  is the enhancement due to defect sites formed by pretreatment (either in He or  $\text{H}_2$ ), and  $y$  is the production of either  $\text{CO}$  or  $\text{CH}_4$ .

For the production of  $\text{CO}$  and  $\text{CH}_4$ , the  $F_{\text{Cu}}$  was 1.3 and 7.4, respectively, which indicated that Cu promoted the formation of both  $\text{CO}$  and  $\text{CH}_4$  since Cu inhibits electron–hole recombinations by trapping electrons.  $F_{\text{D}}$  was 1.1 and 7.4 for  $\text{CO}$  and  $\text{CH}_4$ , respectively, for reactions on  $\text{Ti(He)}$  and 4.8 and 3.5, respectively for reactions on  $\text{Ti(H}_2\text{)}$ . Since they are all above unity, pretreatment, either in He or  $\text{H}_2$ , promoted photoreduction due to the formation of surface defects such as  $\text{Ti}^{3+}$ . The authors postulated that there was a higher concentration of  $\text{Ti}^{3+}$  sites on the  $\text{Ti(H}_2\text{)}$  than the  $\text{Ti(He)}$  since the  $\text{Ti(H}_2\text{)}$  catalyst had a higher  $F_{\text{D}}$  value, and thus, a higher production of  $\text{CO}$ .

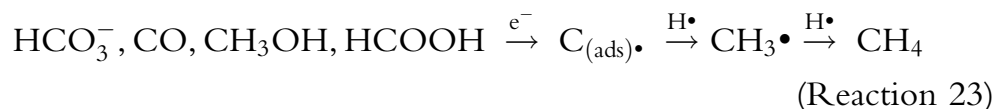
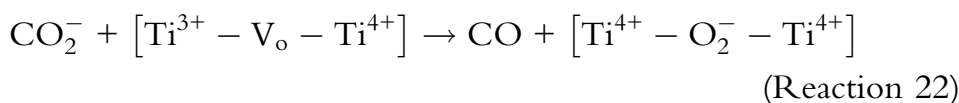
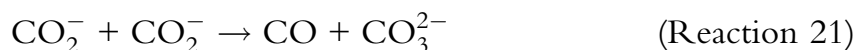
To elucidate the mechanism for activation and reduction of  $\text{CO}_2$ , in situ DRIFTS was used. In situ DRIFTS indicated the formation of bidentate carbonate ( $\text{CO}_3^{2-}$ ), bicarbonate ( $\text{HCO}_3^-$ ),  $\text{CO}_2^-$ , and  $\text{Cu}^+-\text{CO}$ . A mechanism, first postulated by this group in 2012, explains these findings (Fig. 51) (140). The defect sights ( $\text{Ti}^{3+}$ ) holds excess charge that



**Fig. 51** Proposed mechanism for dissociation of  $\text{CO}_2$  on  $\text{TiO}_2$  (140).

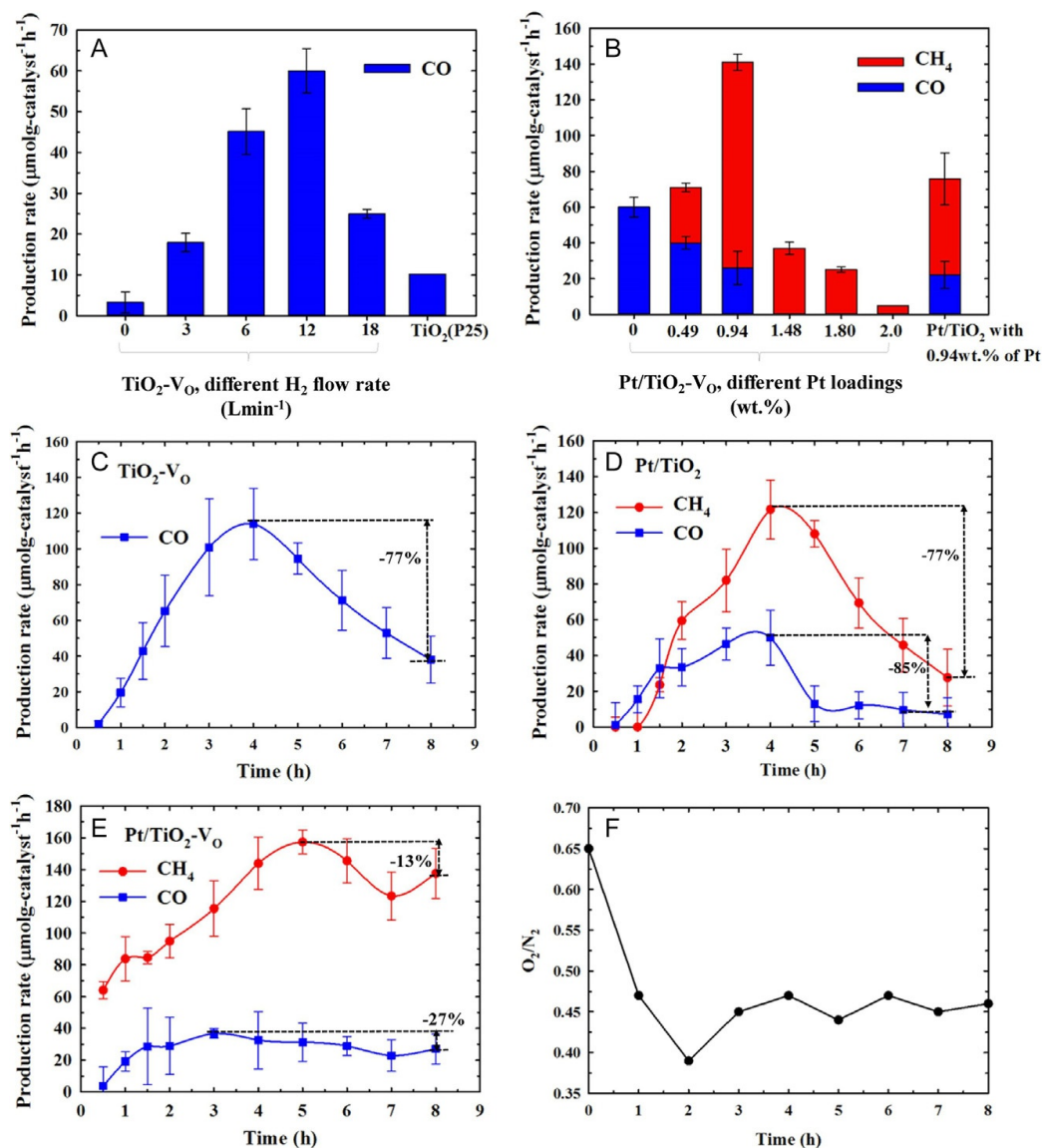


migrates to adsorbed CO<sub>2</sub>, forming CO<sub>2</sub><sup>-</sup>. CO<sub>2</sub> can be dissociated via the CO<sub>2</sub><sup>-</sup> intermediate, forming CO. The function of the Cu could be increased adsorption sites for CO<sub>2</sub>. The reaction mechanism, as reported by the authors, is presented in Reactions 20–23. CO<sub>2</sub><sup>-</sup> can be reduced to CO by H<sup>+</sup> or self-transformation, forming CO<sub>3</sub><sup>2-</sup>. CO can also be formed from direct dissociation (or “healing”) with an oxygen vacancy. The formation of methane, on the other hand, is more complicated since methane requires eight electrons vs two needed by CO. Once a dissociated H is available, formic acid, methanol, formaldehyde, and CO can serve as intermediates for CH<sub>4</sub> formation (114). In this context, it is worth mentioning that Li and Li published a review on photocatalytic water splitting to produce H<sub>2</sub> on semiconductor-based photocatalysts including TiO<sub>2</sub> (141) xy.



Exchanging Pt for Cu, as shown by Lin *et al.*, flips the selectivity toward CH<sub>4</sub> over CO (Fig. 52) when compared to Cu/TiO<sub>2</sub> catalysts. Using a flame aerosol reactor for catalyst synthesis, platinum (platinum acetylacetonate) was infused into the TiO<sub>2</sub> (titanium isopropoxide) matrix which was hydrogenated to form oxygen vacancies (V<sub>o</sub>). Bandgap energies (in eV) were 2.90 (TiO<sub>2</sub>-V<sub>o</sub>), 3.05 (Pt/TiO<sub>2</sub>), and 2.88 (Pt/TiO<sub>2</sub>-V<sub>o</sub>). By adjusting the Pt loadings, the CO<sub>2</sub>/H<sub>2</sub>O reactants could be directed toward the production of methane, and in some cases, only methane. Unfortunately, the catalyst had a relatively short lifetime. In a continuous photocatalytic reactor, peak CO/CH<sub>4</sub> production occurred at 4 h, and then declined, with a 77% loss in production over the next 4 h of reaction time (142).

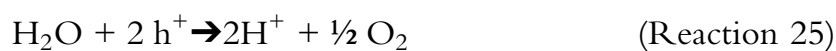
To help explain their results, the authors investigated the role of O<sub>2</sub> (obtained from the photo-oxidation of H<sub>2</sub>O). By defining the ratio of O<sub>2</sub>/N<sub>2</sub> as a parameter to discriminate from exogenous O<sub>2</sub> vs that obtained from the reaction, a mechanism could be postulated. Initially under dark conditions, the O<sub>2</sub>/N<sub>2</sub> ratio significantly reduced and could be defined as an electron scavenging effect.



**Fig. 52** (A) Average CO production rate (8 h) on  $\text{TiO}_2\text{-V}_0$  prepared under different  $\text{H}_2$  flow rates, (B) Effect of Pt content on CO and  $\text{CH}_4$  production rates on  $\text{Pt/TiO}_2\text{-V}_0$  prepared under 12  $\text{L/min}$   $\text{H}_2$  flow, (C–E) CO and  $\text{CH}_4$  Production rates on (C)  $\text{TiO}_2\text{-V}_0$ , (D)  $\text{TiO}_2\text{-V}_0$ , (E)  $\text{Pt/TiO}_2\text{-V}_0$ , (F)  $\text{O}_2/\text{N}_2$  volumetric ratio before and after  $\text{CO}_2$  photoreduction on  $\text{Pt/TiO}_2\text{-V}_0$  (142).



However, under irradiation, the ratio increased due to the photo-oxidation reaction.

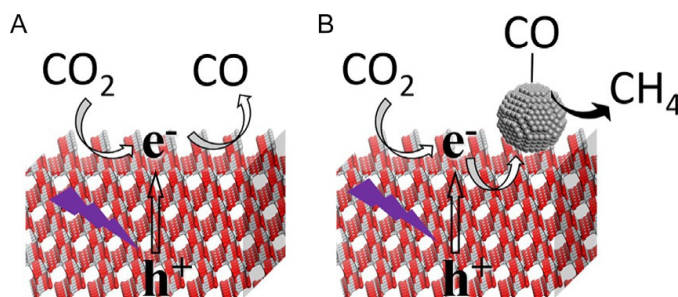


The authors also note that the  $\text{O}_2$  concentration was several orders of magnitude less than  $\text{CO}_2$ . While  $\text{CO}_2$  competed with  $\text{O}_2$  for photogenerated

electrons, the formation of CO and CH<sub>4</sub> indicated that photo-oxidation and photoreduction occurred simultaneously. A metal-support interaction (MSI) model describes the synergistic activity between the Pt and TiO<sub>2</sub>-V<sub>o</sub>. The Pt and TiO<sub>2</sub>-V<sub>o</sub> combination extended the life of the catalyst, as compared to a Cu/TiO<sub>2</sub> catalyst, and enhanced the absorption of light, the surface activation of CO<sub>2</sub>, and the separation efficiency of electron-hole pairs.

Electron-hole charge pairs were investigated using time resolved photoluminescence (PL) spectroscopy and transient photocurrent response measurement. The electron-hole lifetimes were found to be (in ns) 7.03 (TiO<sub>2</sub>-V<sub>o</sub>), 7.53 (Pt/TiO<sub>2</sub>), and 8.37 (Pt/TiO<sub>2</sub>-V<sub>o</sub>) using PL spectroscopy. The photocurrent density was in the order of TiO<sub>2</sub> < TiO<sub>2</sub>-V<sub>o</sub> < Pt/TiO<sub>2</sub> < Pt/TiO<sub>2</sub>-V<sub>o</sub>. These findings show that the strong EMSI promotes charge carrier separations and generates higher photocurrents. On the catalyst without Pt, no CH<sub>4</sub> was formed, most likely due to a lack of electrons needed for the kinetic product (i.e., CH<sub>4</sub>) to form rather than the thermodynamic product (i.e., CO). Addition of Pt provided the much needed photo-generated electrons for CH<sub>4</sub> synthesis. This mechanism is also supported by Tasbihi *et al.* (Fig. 53) who showed the conversion of CO/H<sub>2</sub>O to H<sub>2</sub>, CO, and CH<sub>4</sub> on Pt/TiO<sub>2</sub> (143).

Catalyst deactivation, however, is a major concern for nearly any type of metal impregnation. For the Pt/TiO<sub>2</sub> and Pt/TiO<sub>2</sub>-V<sub>o</sub> surfaces, XPS revealed higher binding energies for the Pt<sup>0</sup> signal for the Pt/TiO<sub>2</sub>, which was attributed to the formation of Pt—O. However, Pt/TiO<sub>2</sub>-V<sub>o</sub> showed no significant increase in the binding energy owing to its high chemical stability. DRIFT results showed high formate production and H<sub>2</sub>O on the Pt/TiO<sub>2</sub>-V<sub>o</sub> surface which was believed to be due to Pt<sup>0</sup> and V<sub>o</sub> surface species. Adsorption and dissociation of H<sub>2</sub>O generates protons that react with



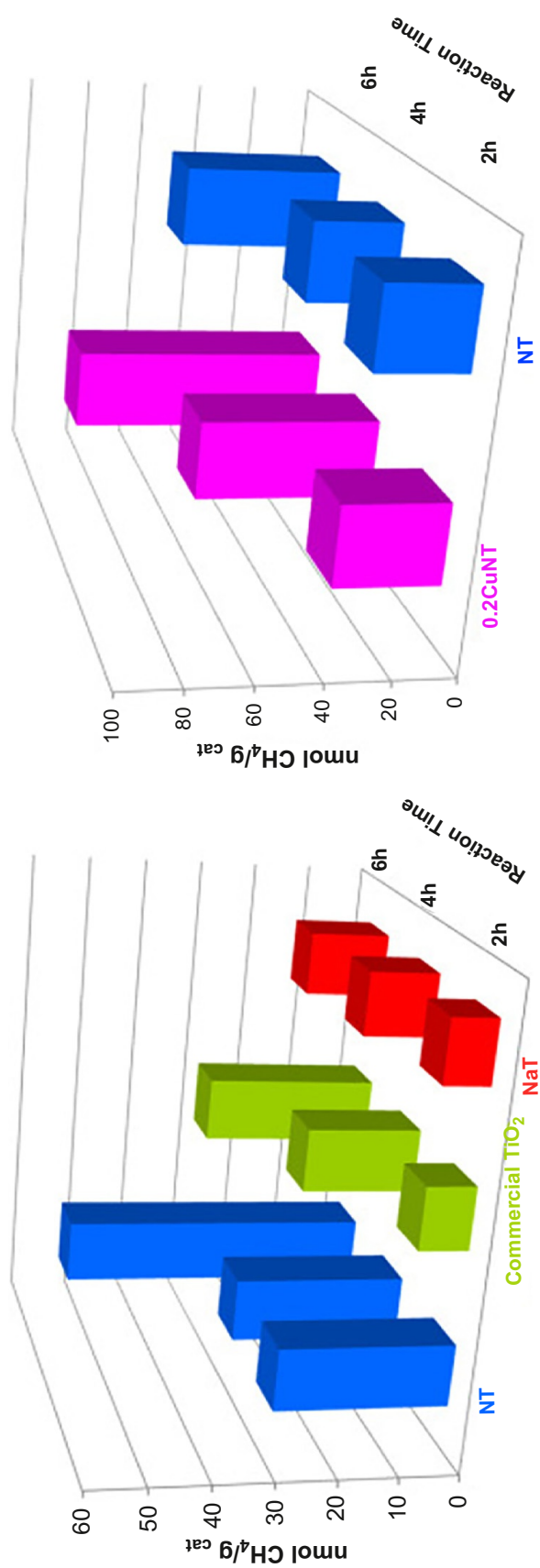
**Fig. 53** Proposed reaction pathway for conversion of CO<sub>2</sub>/H<sub>2</sub>O on (A) TiO<sub>2</sub> and (B) Pt/TiO<sub>2</sub> (143).

carbonates to form formate. Reaction sites are left unoccupied for the next redox cycle due to photoirradiation.  $\text{HCO}_3^-$  and  $\text{CO}_3^{2-}$  are less active intermediates and block surface active sites.

The selectivity toward methane for  $\text{CO}_2/\text{H}_2\text{O}$  reactions was also investigated by Olivo *et al.* (144). Anatase samples were prepared from titanyl sulfate while doping with Cu and N atoms. Reactions were performed in a tubular batch reactor with a 366 nm wavelength with  $50 \text{ W/m}^2$  light. Fig. 54 (left) shows the production of  $\text{CH}_4$  for three catalyst types (a commercial  $\text{TiO}_2$ , a  $\text{TiO}_2$  with N-doping (NT), and a  $\text{TiO}_2$  without N-doping (NaT)). There was a continued increase in methane production throughout the 6-h experiment time. Addition of N greatly enhanced the generation of methane. Methane, by the way, was the only detected product. Addition of Cu to the NT system increased methane generation rates by 40%–50% (Fig. 54 (right)).

When structural properties were considered, BET surface areas were  $93\text{--}110 \text{ m}^2/\text{g}$ , and according to XRD results, only anatase was observed ( $\sim 10 \text{ nm}$  crystallite sizes). Copper nanoparticles were not detected, even at the highest Cu loadings. Temperature programmed reduction (TPR) analyses indicated the reduction of  $\text{Cu}^{2+}$  to  $\text{Cu}^0$ . Furthermore, diffuse reflectance spectroscopy indicated a higher absorbance in the visible region for the 0.6 CuNT than the 0.2 CuNT due to a greater amount of the Cu metal. In the UV–vis region (390–480 nm), N-doping caused intense absorption since nitrogen does not deter light absorption by  $\text{TiO}_2$ . The least absorption was from the 0.6 CuNT catalyst probably from a higher copper concentration that partially covers the titania surface. The formation of methane can be linked to the effects of Cu since the conduction band energy of  $\text{CuO}$  (1.6 eV) is lower than  $\text{Cu}_2\text{O}$  (2.4 eV). Photoexcited D electrons are transferred from the  $\text{TiO}_2$  conduction band to the Cu oxide conduction band, causing a decrease in electron–hole recombinations.

A major focus of their investigation was the effect on product distribution for various  $\text{CO}_2/\text{H}_2\text{O}$  ratios (Table 25). By increasing the concentration of water (i.e., changing the ratio of  $\text{CO}_2$  to water from 13.3 to 2.0), hydrogen begins to appear as a product. In addition, a maximum Turn Over Number (TON) for methane was found to be  $139.9 \text{ nmol}_{\text{CH}_4}/\text{g}_{\text{cat}}$  for a  $\text{CO}_2/\text{H}_2\text{O}=2$ . The trend in  $\text{CH}_4$  production, a bell-shaped curve, could be interpreted by two competitive processes: (1) a required mutual interaction between  $\text{CO}_2$  and  $\text{H}_2\text{O}$  on the catalyst surface to reduce  $\text{CO}_2$  (i.e., more efficient interactions between the two reactants for lower



**Fig. 54** Methane production (left) comparison of a commercial TiO<sub>2</sub>, a TiO<sub>2</sub> with N-doping (NT), and a TiO<sub>2</sub> without N-doping (NaT) and (right) a TiO<sub>2</sub> with 0.2% Cu and N-doping and a TiO<sub>2</sub> with N-doping. Reactions performed with a CO<sub>2</sub>/H<sub>2</sub>O = 13.3 (144).



**Table 25** Methane and hydrogen production and methane selectivity on Cu and N-doped TiO<sub>2</sub> (144).

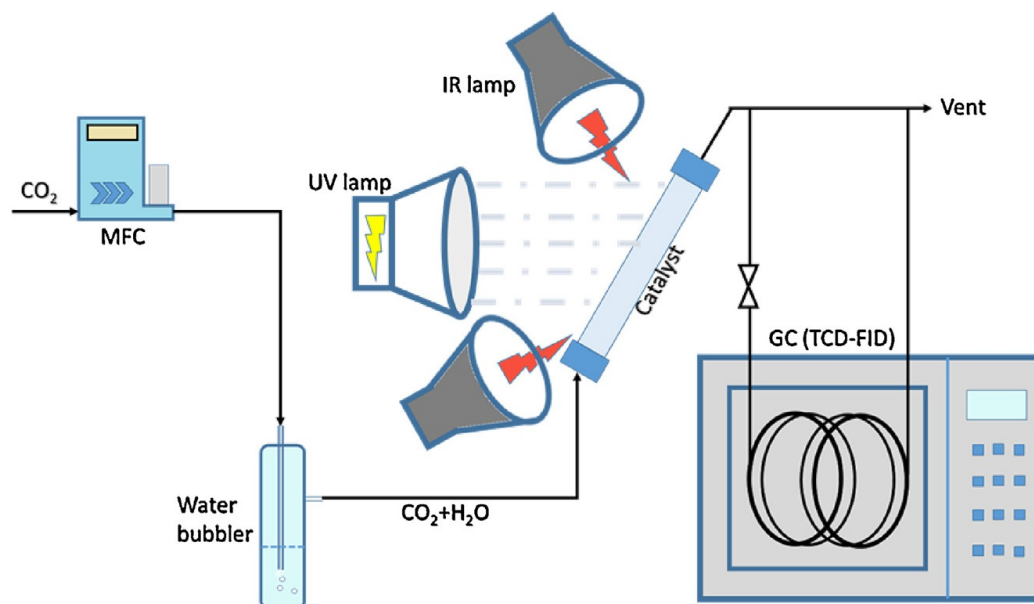
CO <sub>2</sub> /H <sub>2</sub> O	CH <sub>4</sub> production TON (nmol <sub>CH4</sub> /g <sub>cat</sub> )	H <sub>2</sub> production TON (nmol <sub>CH4</sub> /g <sub>cat</sub> )	CH <sub>4</sub> selectivity (%)
13.3	85.3	0	100
10	118.8	6.3	95
5	134.6	7.1	95
2.5	136.9	7.4	94.5
2	139.9	8	94.6
1	92.2	8.8	91.3

CO<sub>2</sub> concentrations) and (2) for CO<sub>2</sub>/H<sub>2</sub>O ≤ 1 water splitting is the main reaction leading to higher H<sub>2</sub> production. In either case, maximized CO<sub>2</sub> conversion is accomplished by an optimum CO<sub>2</sub>/H<sub>2</sub>O ratio (144).

## 10.2 Conversion of CO<sub>2</sub> on supported TiO<sub>2</sub> catalysts

The overall reaction pathway for CO<sub>2</sub> conversion on photocatalytically active TiO<sub>2</sub> follows the typical routes that include adsorption of reactant onto the surface of a catalyst particle, diffusion through the catalyst particle, reaction on an active site, followed by desorption and diffusion of products from the interior of the catalyst particle to the catalyst surface. If the TiO<sub>2</sub> (doped or undoped) nanoparticle is considered the active “site,” then dispersion of the TiO<sub>2</sub> onto a solid support allows for typical heterogeneous reactions to occur.

Mg/Al Layered Double Hydroxides (LDHs) have long been known for their adsorptive capacity for CO<sub>2</sub> (146–149). However, they are not particularly photocatalytically active. To merge the CO<sub>2</sub> adsorptive properties of MgAl-LDH with the photo-active properties of TiO<sub>2</sub>, Zhao *et al.* embedded titania (heat treated 100–600 °C) onto the LDH (145). Using a continuous flow, packed bed reactor (Fig. 55) (200–1000 nm, 420 mW/cm<sup>2</sup> light source), reactions were performed on a series of Ti-containing MgAl-LDH powders that had undergone hydrothermal treatment (HT) at temperatures 100–600 °C (Table 26). The photocatalyst exhibiting the highest production of CO was on HT150 (Ti-embedded on MgAl-LDH hydrothermally treated at 150 °C). Comparing catalysts (normalized by catalyst mass), the optimal hydrothermal treatment was 150–200 °C, where the HT150 catalyst was four times more active than P25 and 50% more active than without



**Fig. 55** Experimental set up for CO<sub>2</sub>/H<sub>2</sub>O conversion on Ti-MgAl-LDH. ( $T_{\text{rxn}} = 150\text{ }^{\circ}\text{C}$ ,  $C_{\text{H}_2\text{O}} = 2.3\text{ vol\%}$ , 200–1000 nm, 420 mW/cm<sup>2</sup> light source) (145).

hydrothermal treatment (CP) (Fig. 56A). When normalized by surface area (Fig. 56B), the HT200 was twice as active as CP and P25. These results show that hydrothermal treatment yielded catalysts that were more active than calcination treatment. By comparing the activity results with structural and optical properties (Table 26), the properties that effect CO<sub>2</sub> photoreduction include TiO<sub>2</sub> crystallinity, band gap energy, surface area, and CO<sub>2</sub> adsorption ability.

MgAl-LDHs are commonly used in purification processes to remove CO<sub>2</sub> from process streams; however, there is a significant cost in energy to desorb CO<sub>2</sub> in a cycling adsorption/desorption process. In an effort to reduce the cost of CO<sub>2</sub> desorption from LDHs, Liu *et al.* investigated the photocatalytic properties of MgAl-TiO<sub>2</sub> (150). To test for the optimum composition for both adsorption and conversion of CO<sub>2</sub>, they explored atomic ratios of Mg:Al:Ti of 3:1:1.5, 3:1:3, and 3:1:4.5, corresponding to 27, 43, and 53 atomic percent of Ti (determined by  $\text{Ti}/(\text{Mg} + \text{Al} + \text{Ti})$ ). Initially, CO<sub>2</sub> was adsorbed onto the MgAl-TiO<sub>2</sub> surface. Under UV reaction conditions (100–200 °C, <390 nm wavelength, continuous flow tubular reactor), CO was found to be the major product (two orders of magnitude more than CH<sub>4</sub>), and CO was then used to determine CO<sub>2</sub> conversion. The adsorbed CO<sub>2</sub> was found to be in the form of carbonate and bicarbonate (Fig. 57). Desorption of some CO<sub>2</sub> occurred and was released as gas phase CO<sub>2</sub> (determined as D%). Some CO<sub>2</sub> was converted (determined as C%),

**Table 26** Structural, optical, and CO<sub>2</sub> adsorption properties of Ti-MgAl-LDH materials (145).

Catalyst	BET (m <sup>2</sup> /g)	Pore size (nm)	Pore volume (cm <sup>3</sup> /g)	CO <sub>2</sub> adsorption capacity (%)	CO <sub>2</sub> adsorption capacity (mmol/g)	CO <sub>2</sub> adsorption capacity per unit surface area (μmol/m <sup>2</sup> )	Bandgap energy (eV)
CP <sup>a</sup>	169.9	5.5	0.25	2.07	0.470	2.77	3.40
HT100 <sup>b</sup>	181.4	6.3	0.3	—	—	—	3.40
HT150	117	10.8	0.38	0.66	0.150	1.28	3.32
HT200	78.3	14.3	0.33	0.62	0.141	1.80	3.31
R400 <sup>c</sup>	111.4	4.2	0.14	0.85	0.193	1.73	3.42
R500	102.1	4.4	0.16	—	—	—	3.35
R600	73.8	5.7	0.2	0.59	0.134	1.82	3.30
P25	—	—	—	0.11	0.025	0.5	3.20

<sup>a</sup>Coprecipitation of Ti onto MgAl-LDH without hydrothermal treatment.<sup>b</sup>Coprecipitation of Ti onto MgAl-LDH with hydrothermal treatment (HT) (in °C).<sup>c</sup>Coprecipitation of Ti onto MgAl-LDH calcined in muffle furnace (R) (in °C).

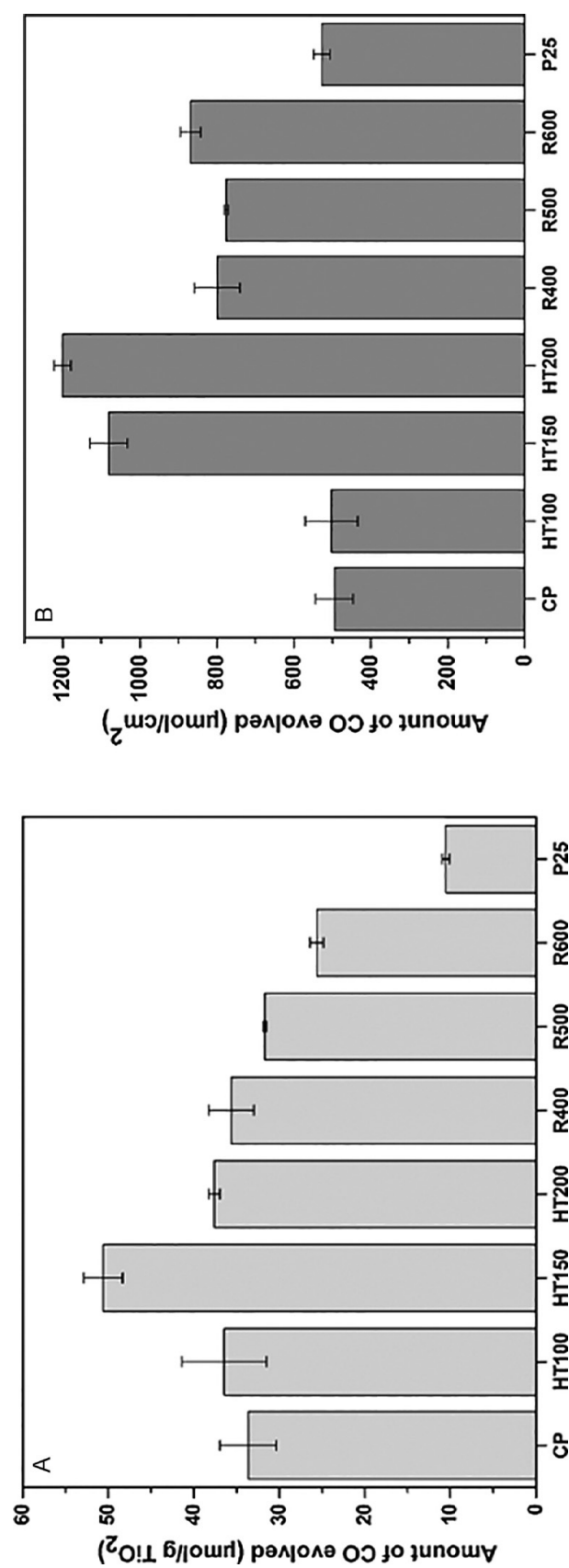
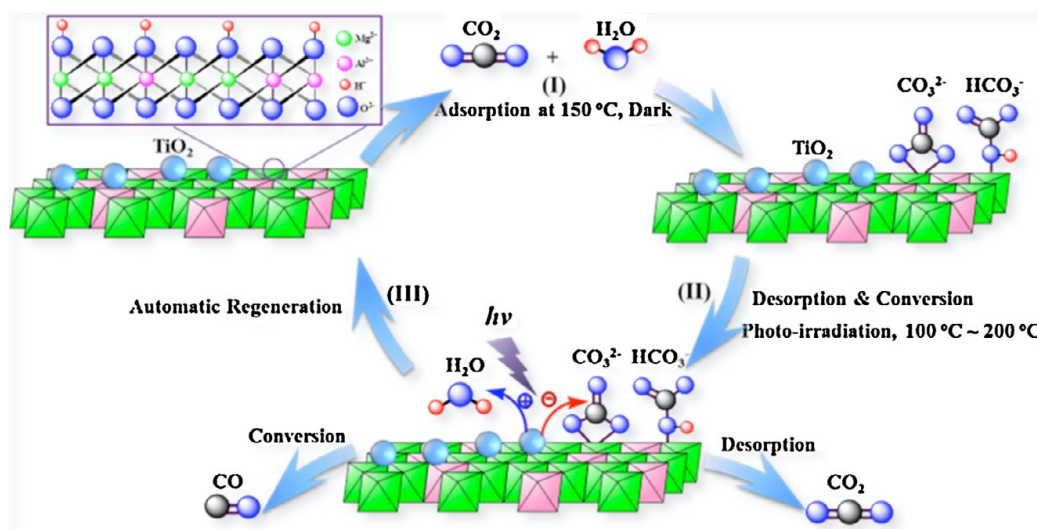


Fig. 56 CO production for  $\text{CO}_2/\text{H}_2\text{O}$  conversion after 5 h UV irradiation (A) normalized by catalyst mass (B) normalized by catalyst surface area (145).



**Fig. 57** Schematic of the integrated CO<sub>2</sub> capture and photocatalytic conversion on TiO<sub>2</sub>-MgAl-LDH catalyst (150).

**Table 27** Percent concentrations for desorbed, converted, and residual CO<sub>2</sub> on various MgAl/TiO<sub>2</sub> catalysts under UV irradiation ( $T_{\text{rxn}} = 200\text{ }^{\circ}\text{C}$ ) (150).

Catalyst	D%	C%	R%
MgAl/Ti <sub>27</sub> <sup>a</sup>	49.1	8.1	42.8
MgAl/Ti <sub>43</sub>	80.2	15.3	4.5
MgAl/Ti <sub>53</sub>	77.9	17.8	4.3

<sup>a</sup>The subscript value is the nominal atomic percent of Ti determined by  $\text{Ti}/(\text{Mg} + \text{Al} + \text{Ti})$ .

and some remained bound to the surface (determined as R%). These are presented in Table 27.

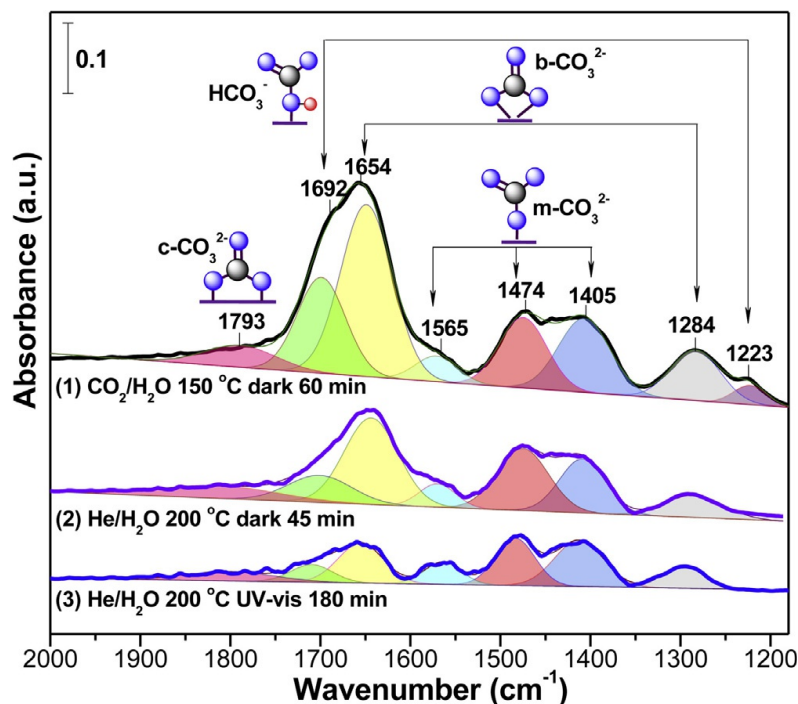
$$D\% = \frac{(\text{CO Desorbed})}{(\text{CO}_2 \text{ Adsorbed})} \times 100 \quad (8)$$

$$C\% = \frac{(\text{CO}_2 \text{ Produced})}{(\text{CO}_2 \text{ Adsorbed})} \times 100 \quad (9)$$

$$R\% = 100\% - D\% - C\% \quad (10)$$

In situ DRIFTS analysis (Fig. 58) provided some of the most elucidating information on CO<sub>2</sub>/TiO<sub>2</sub> surface interactions. When MgAl/Ti<sub>43</sub> was subjected to CO<sub>2</sub>/H<sub>2</sub>O (dark exposure at 150 °C), the adsorbed species were bidentate carbonate (b-CO<sub>3</sub><sup>2-</sup> at 1654 and 1284 cm<sup>-1</sup>), bicarbonate (CO<sub>3</sub><sup>2-</sup> at 1692 and 1223 cm<sup>-1</sup>), and carbonate (m-CO<sub>3</sub><sup>2-</sup> at 1565, 1474, and 1404 cm<sup>-1</sup>). A weak chelating bridge carbonate (c-CO<sub>3</sub><sup>2-</sup> at 1793 cm<sup>-1</sup>) was also found.





**Fig. 58** Adsorbed species of CO<sub>2</sub> and H<sub>2</sub>O on MgAl/Ti<sub>43</sub> as identified from in situ DRIFTS analysis (150).

Furthermore, Spectrum 2 (Fig. 58) (i.e., the desorption phase) showed that peak intensities of HCO<sub>3</sub><sup>−</sup> and b-CO<sub>3</sub><sup>2−</sup> decreased by 53%–58% and those of c-CO<sub>3</sub><sup>2−</sup> and m-CO<sub>3</sub><sup>2−</sup> changed only slightly (15%–17%). Under UV–Vis irradiation for 180 min, the residual HCO<sub>3</sub><sup>−</sup> and b-CO<sub>3</sub><sup>2−</sup> decreased by 60%–70%. There was also a 35%–45% decrease for the c-CO<sub>3</sub><sup>2−</sup> and m-CO<sub>3</sub><sup>2−</sup>, which were strongly chemisorbed and pointed toward CO<sub>2</sub> conversion. These results were explained by the authors as HCO<sub>3</sub><sup>−</sup> and b-CO<sub>3</sub><sup>2−</sup> easily and quickly desorbed at CO<sub>2</sub> and converted to CO via weaker base sites of the M<sup>n+</sup>–O<sup>2−</sup> rather than O<sup>2−</sup> sites. From the gas phase analysis, the authors concluded that:

1. The majority of desorbed CO<sub>2</sub> was due to thermal effect due to weakly bonded HCO<sub>3</sub><sup>−</sup> and b-CO<sub>3</sub><sup>2−</sup>
2. Photocatalytic conversion could initiate from either weakly bonded HCO<sub>3</sub><sup>−</sup>, b-CO<sub>3</sub><sup>2−</sup>, or strongly bonded c-CO<sub>3</sub><sup>2−</sup> and m-CO<sub>3</sub><sup>2−</sup>.

On the best material (MgAl/Ti<sub>43</sub>), there was a 15.3% conversion of CO<sub>2</sub> with only 4.3% residual CO<sub>2</sub> remaining on the surface at 200 °C reaction temperature. Considering that typical desorption temperatures are 400–500 °C, removal of converted CO<sub>2</sub> at a much lower temperature is an economic victory, especially a salable product is formed. Cyclic

adsorption/(desorption/conversion) experiments determined that conversion decreased slightly (15.3%–13.0%) after 5 cycles. The desorption remained nearly constant at  $\sim 80\%$  for each cycle (150).

The performance of photocatalytic  $\text{CO}_2$  reduction on  $\text{TiO}_2$ -type catalysts supported on monoliths was studied by Tahir *et al.* (151). Combinations of  $\text{TiO}_2$ ,  $\text{InO-TiO}_2$ ,  $\text{NiO-TiO}_2$ , and  $\text{NiO-InO-TiO}_2$  active materials were coated onto a cordierite ceramic monolith with square channels. Batch reactions ( $100^\circ\text{C}$ , UV irradiation,  $\text{CO}_2/\text{H}_2 = 1.0$ ) resulted in products ranging from CO to light hydrocarbons ( $\text{C}_1\text{--C}_3$  with mixtures of alkanes and alkenes) (Table 28). Depending on catalyst used, product yield and selectivity could be tailored for desired needs.  $\text{In}_2\text{O}_3/\text{TiO}_2$  catalysts promoted CO formation, and the addition of NiO strongly promoted CO formation. Efficient charge transfer, high surface areas, and improved adsorption/desorption processes were cited as reasons for the high activity levels. However, reduced charge recombination centers with excess  $\text{In}_2\text{O}_3$  loading may have attributed to lower photocatalytic activity (151).

Steady-state reactions revealed that the reverse water gas shift (RWGS) reaction was strongly favored for the  $\text{In}_2\text{O}_3/\text{TiO}_2$  and  $\text{NiO-In}_2\text{O}_3/\text{TiO}_2$

**Table 28** Product yield and selectivity for  $\text{CO}_2/\text{H}_2$  reactions on  $\text{TiO}_2$  and metal-doped  $\text{TiO}_2$  (151).

Catalyst	Yield of products ( $\mu\text{g/g}_{\text{cat}}$ )						Selectivity (%)	
	CO	$\text{CH}_4$	$\text{C}_2\text{H}_4$	$\text{C}_2\text{H}_6$	$\text{C}_3\text{H}_6$	$\text{C}_3\text{H}_8$	CO	$\text{CH}_4$
$\text{TiO}_2$	95	137	—	—	—	—	40.95	59.05
2% $\text{In}_2\text{O}_3/\text{TiO}_2$	1150	120	2.85	6.73	2.31	1.30	89.63	9.34
3.5% $\text{In}_2\text{O}_3/\text{TiO}_2$	1805	36	0.61	2.18	1.98	0.87	97.92	1.93
5% $\text{In}_2\text{O}_3/\text{TiO}_2$	1227	52	1.15	3.39	2.03	0.99	95.40	4.02
1% $\text{NiO}/\text{TiO}_2$	2250	45	0.41	0.47	0.78	0.34	97.55	2.40
2% $\text{NiO}/\text{TiO}_2$	7306	38	0.25	0.67	0.84	0.32	99.46	0.51
3% $\text{NiO}/\text{TiO}_2$	4516	46	0.66	0.94	1.83	0.60	98.76	1.14
0.5% $\text{NiO}$ -3.5% $\text{In}_2\text{O}_3/\text{TiO}_2$	4826	144	3.12	12.06	25.47	3.71	94.94	3.87
1% $\text{NiO}$ -3.5% $\text{In}_2\text{O}_3/\text{TiO}_2$	11,325	97	0.74	2.94	15.97	8.00	98.91	0.85
2% $\text{NiO}$ -3.5% $\text{In}_2\text{O}_3/\text{TiO}_2$	6100	37	0.34	1.71	38.03	5.19	98.67	0.60

**Table 29** Photocatalytic CO<sub>2</sub> reduction with H<sub>2</sub> using TiO<sub>2</sub> and metal-doped TiO<sub>2</sub> on monolith channels (151).

Catalyst	Conversion (%)			Yield rates (μmol/g <sub>cat</sub> h) <sup>a</sup>					Selectivity (%)	
	CO <sub>2</sub>	H <sub>2</sub>	CO	CH <sub>4</sub>	C <sub>2</sub> H <sub>4</sub>	C <sub>2</sub> H <sub>6</sub>	C <sub>3</sub> H <sub>6</sub>	C <sub>3</sub> H <sub>8</sub>	CO	CH <sub>4</sub>
TiO <sub>2</sub>	1.7	2.3	58	68	0.13	3.25	0.33	0.38	44.58	52.27
3.5% In <sub>2</sub> O <sub>3</sub> /TiO <sub>2</sub>	6.42	5.48	2028	31	0.48	1.94	0.19	0.18	98.36	1.50
1% NiO-3.5% In <sub>2</sub> O <sub>3</sub> /TiO <sub>2</sub>	10.20	16.40	12,029	34	0.33	1.95	2.36	1.01	99.67	0.28

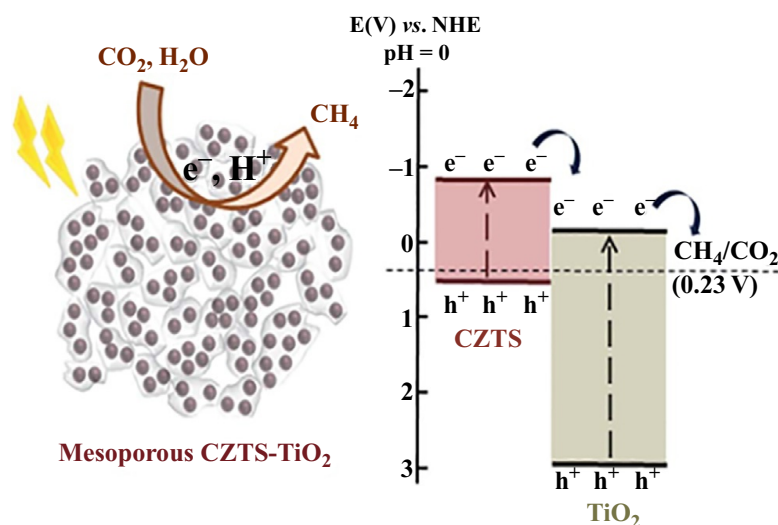
<sup>a</sup>Yield rates determined from 8 h irradiation basis, CO<sub>2</sub>/H<sub>2</sub>=1.5, T<sub>rxn</sub>=120 °C.

catalysts (Table 29). Selectivity toward CO was nearly 100%. Conversion of CO<sub>2</sub>, rarely reported for CO<sub>2</sub> photocatalytic conversions, were 6.42 and 10.20 on the In<sub>2</sub>O<sub>3</sub>/TiO<sub>2</sub> and NiO-In<sub>2</sub>O<sub>3</sub>/TiO<sub>2</sub>, respectively. Large surface areas (84–87 m<sup>2</sup>/g), increased mesoporosities, higher mobility of charges due to hindered recombinations of photo-generated charges, better light absorption, and efficient mass transfer were cited as reasons for the superior photocatalytic activity.

The authors also established a Quantum Efficiency (QE) for comparison of various types of catalyst/reactor systems (Eq. 11). The UV light energy input into the reactor was used to calculate the moles of photons. For their catalysts, they determined % QE to be 0.053, 1.04, and 0.48 for cell type batch reactor, microchannel monolith type batch reactor, and microchannel monolith type continuous reactor, respectively. The QE determination revealed that the monolithic reactors (both batch and continuous) had higher performances, which was attributed to the hindered charge/hole recombinations. QE was also higher when H<sub>2</sub> was used as the reductant rather than H<sub>2</sub>O (151)

$$\text{QE (\%)} = \frac{2 \times \text{moles of CO rate } \left(\frac{\text{mol}}{\text{s}}\right)}{\text{moles of photon flux } \left(\frac{\text{mol}}{\text{s}}\right)} \times 100 \quad (11)$$

In another study on hybrid TiO<sub>2</sub> photocatalyst, Kim *et al.* synthesized a Cu<sub>2</sub>ZnSnS<sub>4</sub>-TiO<sub>2</sub> (designated as CZTS-TiO<sub>2</sub>) photocatalyst (152). CZTS is a p-type semiconductor (bandgap=1.5 eV) that was originally developed as a photovoltaic material. Its use in this study was to create a p-n heterojunction with the n-type TiO<sub>2</sub> (Fig. 59). Activity tests were



**Fig. 59** Catalytic energy diagram for the photocatalytic conversion of  $\text{CO}_2/\text{H}_2\text{O}$  on  $\text{Cu}_2\text{ZnSnS}_4\text{-TiO}_2$  (152).

**Table 30** Turnover number (TON) and turnover frequency (TOF) for CZTS- $\text{TiO}_2$  catalysts (CT1, CT2, CT3, and CT4 represents 1.9, 3.8, 5.7, and 7.6 mg of CZTS in 0.1 mL  $\text{TiCl}_4$ , respectively) (152).

Catalyst	TON <sup>a</sup>	TOF <sup>b</sup>
CT1	0.31	0.31
CT2	0.37	0.37
CT3	0.76	0.76
CT4	1.48	1.48
CT4 (5 h)	1.7	0.34
CT4 (10h)	0.9	0.09

$$^a\text{TON} = \frac{\text{moles CH}_4 \text{ produced}}{\text{moles TiO}_2 \text{ Present on catalyst}} \quad (12).$$

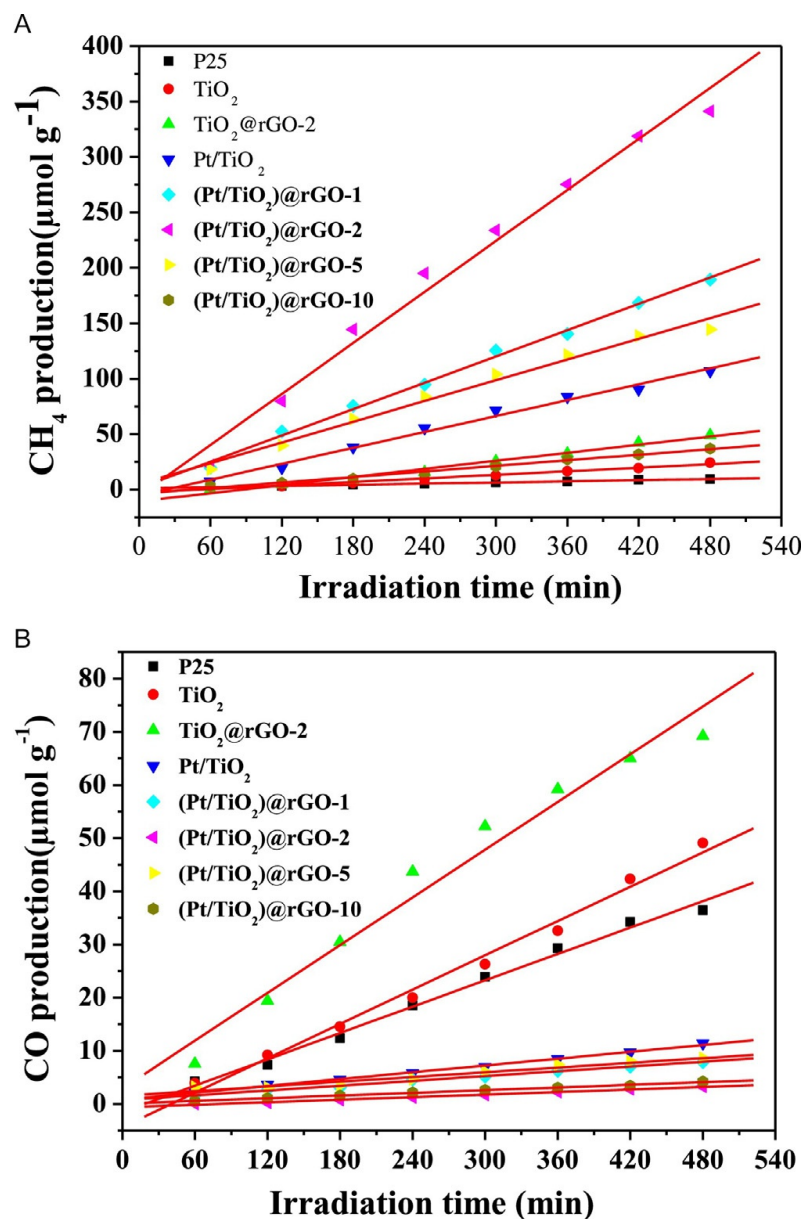
$$^b\text{TOF} = \frac{\text{TON}}{\text{Reaction time (hours)}} \quad (13).$$

conducted using a  $\text{CO}_2/\text{H}_2\text{O}$  mixture irradiated using a Xenon AM 1.5 filtered light source. Product analysis showed mainly methane after 1 h of illumination. Increased concentration of CZTS yielded higher methane production (up to 118.75 ppm/g<sub>cat</sub> h). Turnover numbers (TON) and Turnover Frequencies (TOF) are presented in Table 30. After 1 h of illumination, the CT4 catalyst had a 1.48 TON and 1.48 h<sup>-1</sup> TOF. The TON was 1.67 after 5 h and 0.90 after 10 h of continuous illumination.

As already pointed out, adsorption/desorption of reactant and product molecules play an important role in the overall catalytic process, especially when selecting support materials. In addition, highly efficient electron acceptors and transports are also necessary. Carbon-based supports, such as Graphene oxides and carbon nanotubes, are then considered as support materials since they have surface hydroxyl groups and extended  $\pi$  bond for improved adsorption and activation of CO<sub>2</sub>/H<sub>2</sub>O molecules.

Zhao *et al.* synthesized and tested Pt/TiO<sub>2</sub> core shells supported on reduced graphene oxide sheets ((Pt/TiO<sub>2</sub>)@rGO-*n*) using a gas-closed circulation reactor system (153). (“*n*” refers to the nominal weight percent of rGO to Pt/TiO<sub>2</sub>) Fig. 60 shows the production of CH<sub>4</sub> and CO during an 8 h irradiation time. Product yields and selectivities can be found in Table 31. Selectivity for CO was approximately (~58%) the same for P25, TiO<sub>2</sub>, and TiO<sub>2</sub>@rGO catalysts. However, addition of Pt to TiO<sub>2</sub>, and TiO<sub>2</sub>@rGO shifts the selectivity toward CH<sub>4</sub> (93%–95%). These results were attributed to platinum’s lower Fermi energy level, providing for enhanced trapping photo-generated electrons. There existed an improved efficiency for light harvesting due to an electronic coupling between  $\pi$  states of rGO and conduction band states of TiO<sub>2</sub>. This improved efficiency lead to a lowering of the bandgap from ~3.1 to ~2.5 eV for P25 and Pt/TiO<sub>2</sub>)@rGO-2, respectively.

The mechanism (Fig. 61), as described by the authors, consists of photogenerated electrons that form an enriched region on the reduced graphene oxide shell. Within this enriched region, CO<sub>2</sub> is reduced to CH<sub>4</sub>. The electron–holes contained within the TiO<sub>2</sub> reaction with H<sub>2</sub>O and O<sub>2</sub>, along with a H<sup>+</sup>, for the CO<sub>2</sub> reduction. The electron transfer that takes place is TiO<sub>2</sub> → Pt → rGO and could be a rate-limiting source. The adsorption of CO<sub>2</sub> is favorable to the abundant  $\pi$  electron cloud of the rGO. Therefore, the formation rate of CH<sub>4</sub> is closely linked to the thickness of rGO on the surface of the Pt/TiO<sub>2</sub>. If the rGO is too thick, light penetration to TiO<sub>2</sub> is negatively impacted. If it too thin, there is insufficient electron collection. A quantum efficiency (based on methane productions) was also determined (Table 31). The best efficiencies were 1.06 and 1.93, and 0.90% for (Pt/TiO<sub>2</sub>)@rGO-1, (Pt/TiO<sub>2</sub>)@rGO-2, (Pt/TiO<sub>2</sub>)@rGO-5, respectively. These results also point toward an optimized thickness of reduced graphene oxide. In fact, (Pt/TiO<sub>2</sub>)@rGO-10 had a QE=0.25, indicating a significant loss of incident light penetrating to the TiO<sub>2</sub> when rGO was 10 wt% (153).



**Fig. 60** Production of CH<sub>4</sub> (A) and CO (B) for CO<sub>2</sub>/H<sub>2</sub>O photocatalytic conversion over TiO<sub>2</sub>, Pt-TiO<sub>2</sub>, and Pt-TiO<sub>2</sub> on reduced graphene oxide support (153).

In another study toward the photocatalytic conversion of a CO<sub>2</sub>/H<sub>2</sub>O mixture, Piler *et al.* investigated synthesis parameters for TiO<sub>2</sub>/single walled carbon nanotube (SWCNT) nanocomposites (154). They used surfactants (sodium dodecyl sulfate (SDS) and sodium dodecyl benzenesulfonate (SDBS) to separate SWCNT bundles prior to adsorbing TiO<sub>2</sub> nanoparticles onto the SWCNT surfaces (Fig. 62). Their procedure utilized UV irradiation during the synthesis procedure to induce disturbances within the TiO<sub>2</sub> lattice structures. These disturbances, along with  $\pi$ - $\pi$  stacking interactions of

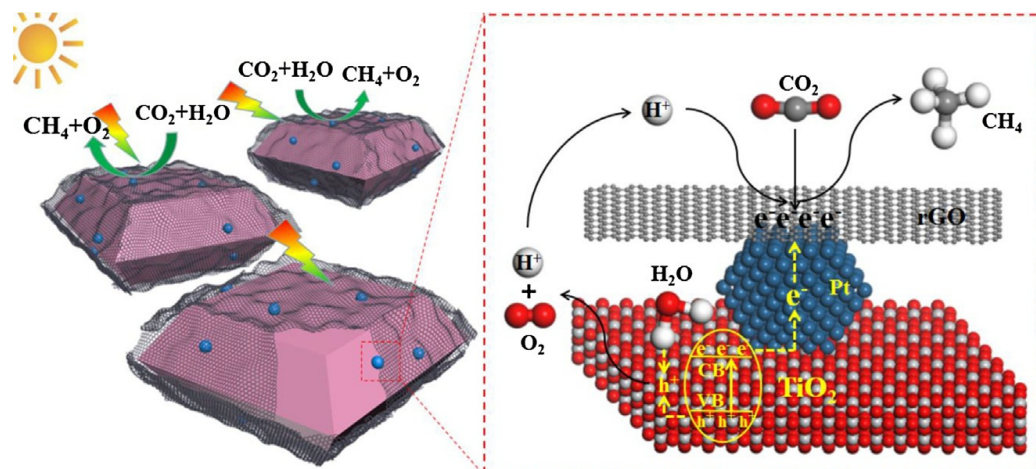


**Table 31** Production and production selectivity for CO<sub>2</sub>/H<sub>2</sub>O conversion on TiO<sub>2</sub>, Pt-TiO<sub>2</sub>, and Pt-TiO<sub>2</sub> on reduced graphene oxide support (153).

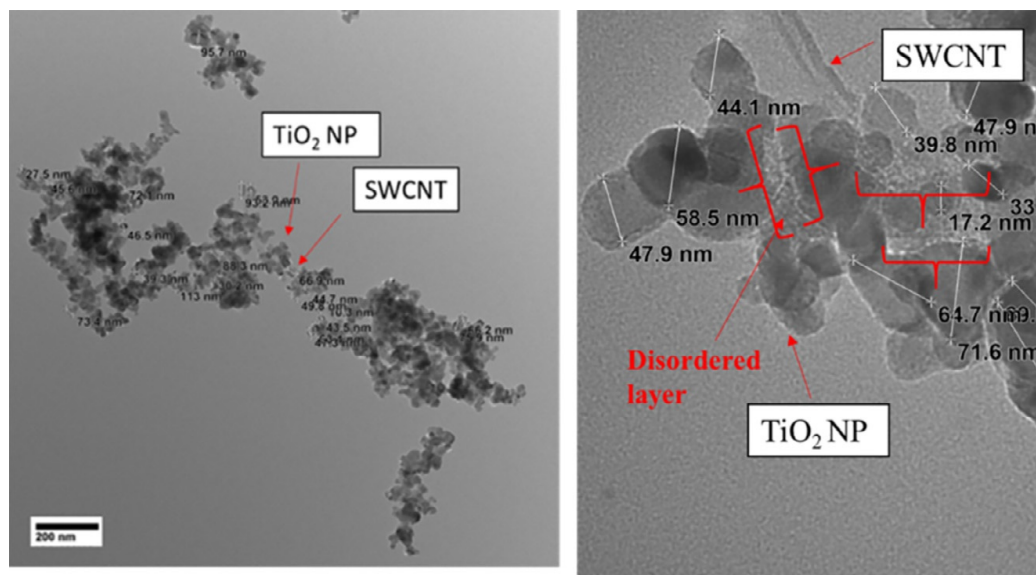
Catalyst	Rate of product formation ( $\mu\text{mol/g}_{\text{cat}} \text{ h}$ ) <sup>a</sup>				Selectivity (%)		
	CO	CH <sub>4</sub>	H <sub>2</sub>	O <sub>2</sub>	CO	CH <sub>4</sub>	QE <sub>CH<sub>4</sub></sub> (%) <sup>b</sup>
P25	1.8	1.3	3.8	—	58.1	41.9	0.06
TiO <sub>2</sub> -001/101	4.7	3.4	5.4	15.5	58.0	42.0	0.17
Pt/TiO <sub>2</sub>	1.3	13.3	72.7	67.3	7.0	93.0	0.65
TiO <sub>2</sub> @rGO-2	8.6	6.0	0.8	17.7	58.9	41.1	0.30
(Pt/TiO <sub>2</sub> )@rGO-1	0.8	23.2	21.1	61.8	3.3	96.7	1.06
(Pt/TiO <sub>2</sub> )@rGO-2	0.4	41.3	5.6	98.4	0.9	99.1	1.93
(Pt/TiO <sub>2</sub> )@rGO-5	1.0	19.8	13.7	54.9	4.8	95.2	0.90
(Pt/TiO <sub>2</sub> )@rGO-10	0.4	4.7	3.7	12.0	7.8	92.2	0.25

<sup>a</sup>Reaction conditions: 0.1 g photocatalyst, 0.1 MPa CO<sub>2</sub> pressure, 2 mL H<sub>2</sub>O, 320–780 nm light source, 8 h irradiation, T<sub>rxn</sub> = 4 °C

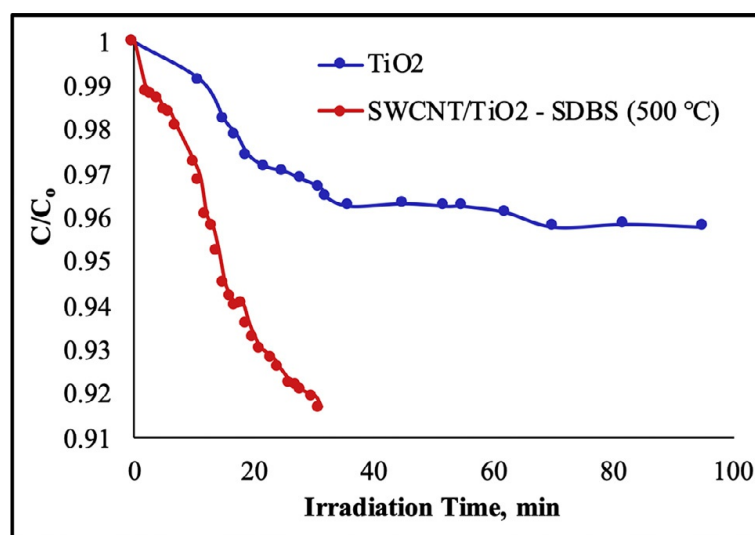
<sup>b</sup>QE<sub>CH<sub>4</sub></sub> (%) =  $\frac{8 \times (\text{number of produced CH}_4 \text{ molecules})}{(\text{number of incident photons})} \times 100$ .

**Fig. 61** Proposed reaction mechanism for CO<sub>2</sub>/H<sub>2</sub>O photocatalytic conversion over (Pt/TiO<sub>2</sub>)@rGO catalyst (153).

the SDBS benzene ring and the carbon nanotubes, lead to an intimate contact between the SWCNT and the TiO<sub>2</sub>. The samples were then heat treated at 200, 350, and 500 °C, producing photocatalysts with bandgap energies  $\sim 1.0$  to 2.75 eV, where the lowest bandgap energies occurred for the SDBS-treated samples that had been calcined at either 350 and



**Fig. 62** TEM images of nanocomposite materials containing TiO<sub>2</sub> nanoparticle (NP) on SWCNT (154).



**Fig. 63** Reaction results comparing TiO<sub>2</sub> and SWCNT/TiO<sub>2</sub> prepared using SDBS, UV irradiation, and calcined at 500 °C (<400 nm light source,  $T_{\text{rxn}} = 40$  °C) (154).

500 °C. Reaction results (Fig. 63) illustrate a markedly increased activity for the SWCNT/TiO<sub>2</sub> (that had been synthesized using SDBS and then calcined at 500 °C) compared to bare TiO<sub>2</sub> (154).

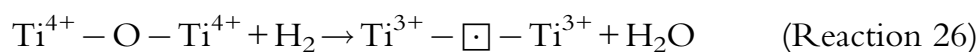


## 11. Oxygen vacancy recovery during photocatalytic reaction

There are pathways to regenerate oxygen vacancies during a photocatalytic reaction. Ye *et al.* studied bismuth oxychloride (BiOCl)

photocatalyst in converting N<sub>2</sub> to NH<sub>3</sub> and CO<sub>2</sub> to CH<sub>4</sub>. In the presence of UV irradiation, oxygen vacancies can be refreshed. The underlying mechanism is still under debate (155). However, it was mentioned by Wu *et al.* that hydroxyl groups, play a significant role in the evolution (or recovery process) of photoinduced oxygen vacancies in BiOCl during the reaction (156). Ye *et al.* stated that the oxygen vacancy concentration in BiOCl photocatalyst increased as UV irradiation time increased as well as a catalyst color change from white to black (155).

No research has been reported on the recovery process of oxygen vacancies during the reaction with TiO<sub>2</sub> as the photocatalyst. However, an assumption could be put forward that TiO<sub>2</sub> could follow a similar pathway in the recovering of oxygen vacancies as found in the case of BiOCl photocatalyst. Strunk *et al.* has suggested a pathway for formation of Ti<sup>3+</sup> and oxygen vacancies in the presence of hydrogen shown in Reaction (26) (48).



One possible theory is that the hydrogen generated during the photocatalytic reaction in the presence of water and CO<sub>2</sub> could help in partially reducing Ti<sup>4+</sup> to Ti<sup>3+</sup> while creating titanium defects that could be used in photoreducing CO<sub>2</sub> more efficiently. Another proposed theory is that injecting hydrogen into the reactor during the photocatalytic conversion of CO<sub>2</sub> using TiO<sub>2</sub> as the photocatalyst creates a constant recovery of defects.



## 12. Concluding remarks

As has been described in this review, TiO<sub>2</sub> has played and will continue to play a role in photocatalytic conversions, especially CO<sub>2</sub>, to more useful compounds. Since titanium is abundantly available, TiO<sub>2</sub> can be readily produced in either of its several crystallographic forms. Incorporating lattice defects into the crystal structure has shown to be the most effective method for increasing CO<sub>2</sub> adsorption onto the surface as well as establishing the appropriate Fermi energy for surface catalytic chemistries. Synthesizing the various types of defects has been the focus of much of the most recent research for photocatalytically-active TiO<sub>2</sub>. To be most effective as a photocatalyst, longer electron-hole separation times are needed, which can be accomplished by controlled construction of lattice defects, such as oxygen vacancies.

Fundamental understanding of the  $\text{TiO}_2$  surfaces has been driven through DFT and surface characterizations. Hybrid DFT models allow for specific spin state calculations as well as contributions from potential gradients as is expected for photocatalytic reactions. Calculations based on cell size, spin polarization, electron localization, and long range interactions were performed on numerous types of  $\text{TiO}_2$  surfaces. However, the more complex the calculation, the more computation time is needed. Investigations using noble metals (Au and Pt) revealed that Pt binds to the rutile (110) surface without oxygen vacancies much more strongly than Au, probably since Au forms 3-dimensional clusters. Therefore, Pt is easier to distribute across the Rutile surface. Both metals can be adsorbed beyond the surface layer and promote reactions via band gap energy states. It is further suspected that controlling the concentration of Pt leads to wavelength tuning. However,  $\text{H}_2$  bonds strongly to Pt, which could be a detriment to  $\text{CO}_2$  conversions that require a reductant where  $\text{H}_2$  could be fed as a core-actant or evolved through water splitting reactions. Mid-gap energy states were produced using  $\text{CuO}_x$  nanoclusters on  $\text{TiO}_2$  anatase and rutile, both computationally and experimentally. The modeling showed that Cu, independent of its oxidation state, bound strongly to the  $\text{TiO}_2$ . The experimental work corroborated the computational work that predicted a red shift in the band gap of this n-type and p-type heterojunction. This combination of computational/experimental illustrated the powerful confluence of these two worlds.

As developed throughout this work, advancement in  $\text{TiO}_2$  photocatalytic conversions arise from deep understanding of theory, synthesis, and material characterization. Investigating lattice defects using in situ DRIFTS, Electron Paramagnetic Resonance (EPR), 3D-AFM, AFM-STM, photo-electrochemical characterization, positron annihilation lifetime spectroscopy (PALS), and Atomic Force Microscopy (AFM) have led to identifying and quantitating surface and sub-surface oxygen vacancies, band gap energies, and Fermi energy levels. EPR, which has been well described by Che and Tench (157,158), has shown useful in identifying unpaired electrons trapped by an oxygen vacancy as well as in understanding  $\text{Ti}^{3+}$  defects, which are not readily detected using XPS. More recent studies suggest that surface bridging oxygen vacancies are primarily responsible for the band gap state in  $\text{TiO}_2$ , although some contribution arrives from other defects, possibly interstitial Ti or subsurface oxygen vacancies (159). Komaguchi *et al.* demonstrated that sub-band gap illumination promotes electron transfer from  $\text{O}_2^{2-}$  at an oxygen vacancy to an adjacent  $\text{Ti}^{4+}$ , creating a  $\text{Ti}^{3+}$  site (160).

Finally, this review explores the experimental work performed for synthesizing  $\text{TiO}_2$ -based photocatalysts with particular interest in  $\text{CO}_2$  conversion to useful products using light in the visible spectrum. Some of the most useful materials we discovered were carbon modified  $\text{TiO}_2$  where Pt could be doped onto the  $\text{TiO}_2$  and the carbon material activated as an electron acceptor and an electron transporter for highly efficient electron-hole recombinations. In reactions containing  $\text{CO}_2$  and  $\text{H}_2\text{O}$ , the selectivity of methane over carbon monoxide could be tuned through the addition of Pt. However, if the carbon material (reduced graphene oxides were used) were too thick, transmission of light was poor, hindering the reaction. A conversion of 10.2% was reported for a  $\text{NiO-In}_2\text{O}_3/\text{TiO}_2$  catalyst imbedded on a monolithic support. A  $\text{CO}_2$  conversion of 17.8% was reported for  $\text{TiO}_2$  supported onto a  $\text{MgAl}$  layered double hydroxide. An extensive review of  $\text{CO}_2$  photoreduction to useful fuels and chemicals on various cocatalysts can be found by Li *et al.* (161).



### 13. Future challenges

The conversion of large scale  $\text{CO}_2$  is a daunting endeavor. If we just focus on the large point sources that are emitted from natural gas or coal-fired electric power generators, chemical manufacturing facilities, and petroleum refineries, there are many scientific and technological challenges that must be reconciled. One of those challenges is development of economical conversion practices of  $\text{CO}_2$  into useful fuels and chemicals. Photocatalytic conversion is a much lower temperature alternative (i.e., potential cost savings) than dry reforming or tri-reforming processes. The current body of research has focused on the material synthesis of  $\text{TiO}_2$  photocatalysts.  $\text{TiO}_2$  is readily available and affordable, and its qualities of as being photo-active, make it a prime catalyst candidate. However, little attention has been given toward the robustness of  $\text{TiO}_2$  (undoped, doped, nanocomposite, etc.) under real reaction conditions. All of the industrial effluents mentioned above must be captured and cleaned of common impurities, including hydrogen sulfide, sulfur oxides, and nitrogen oxides, prior to being ready for the photocatalytic conversion.  $\text{H}_2\text{S}$  removal technologies have been reported by Agbroko *et al.* and Doan and Benson (162,163), while the use of molecular basket sorbents for the removal of  $\text{SO}_2$  and  $\text{NO}_2$  from flue gases have been reported by Wang *et al.* as well as for the removal of  $\text{H}_2\text{S}$  and  $\text{CO}_2$  by Ma *et al.* (164,165). These removal processes will be costly. If the photocatalyst can be designed to incur some level of

impurities, the overall cost of CO<sub>2</sub> conversion decreases precipitously. Therefore, additional computational and experimental work is necessary to mature the technology.

The other grand challenge for advancing photocatalytic CO<sub>2</sub> conversion is the development of the complete catalyst, including catalyst support, and the needed reactor system for efficient conversions under robust conditions. While some initial work on imbedding TiO<sub>2</sub> onto catalyst supports, this area is lacking in common chemical reaction engineering, such as optimum reaction temperature, space velocities, and heat and mass transport resistance minimizations. Lastly, the reactor design must be investigated. As illustrated throughout this work, operating within the visible region offers direct sunlight utilization. A solar reactor design would be another step toward economic viability.

## Acknowledgments

This research was funded in part by the Texas Air Research Center (Grant #: 415LUB0149A) and by the Center for Advances in Water and Air Quality (Grant #: P2015-A1-011). The authors would like to thank the Lamar University Materials Instrumentation Center for help with understanding of characterization tools and phenomenon. Dr. Tracy J. Benson acknowledges support from the Center for Midstream Management and Science at Lamar University.

## References

1. Cuellar-Franca, R. M.; Azapagic, A. J. *CO<sub>2</sub> Util.* **2015**, *9*, 82–102.
2. Meryem, S. S.; Nasreen, S.; Siddique, M.; Khan, R. *Rev. Chem. Eng.* **2017**, *34*, 1–17.
3. Sellì, D.; Fazio, G.; Valentin, C. D. *Catalysts* **2017**, *7*, 1–24.
4. Lin, Z.; Orlov, A.; Lambert, R. M.; Payne, M. C. *J. Phys. Chem.* **2005**, *109*, 20948–20952.
5. Hoye, R. L. Z.; Musselman, K. P.; MacManus-Driscoll, J. L. *APL Mater.* **2013**, *1*, 1–11.
6. Cai, J.; Wu, M.; Wang, Y.; Zhang, H.; Meng, M.; Tien, Y.; Li, X.; Zhang, J.; Zheng, L.; Gong, J. *Chem* **2017**, *2*, 877–892.
7. Chen, X.; Liu, L.; Yu, P. Y.; Mao, S. S. *Science* **2011**, *331*, 746–750.
8. Munnix, S.; Schmeits, M. *Phys. Rev. B* **1985**, *31*, 3369–3371.
9. Liu, L.; Zhao, H.; Andino, J. M.; Li, Y. *ACS Catal.* **2012**, *2*, 1817–1828.
10. Monai, M.; Montini, T.; Fornasiero, P. *Catalysts* **2017**, *7*, 2–19.
11. Anitha, V. C.; Banerjee, A. N.; Joo, S. W. *J. Mater. Sci.* **2015**, *50*, 7495–7536.
12. Tang, C.; Zhou, D.; Zhang, Q. *Mater. Lett.* **2012**, *79*, 42–44.
13. Xin, X.; Xu, T.; Wang, L.; Wang, C. *Sci. Rep.* **2016**, *6*, 1–8.
14. Haggerty, J. E. S.; Schelhas, L. T.; Kitchaev, D. A.; Mangum, J. S.; Garten, L. M.; Sun, W.; Stone, K. H.; Perkins, J. D.; Toney, M. F.; Ceder, G.; Gineley, D. S.; Gorman, B. P.; Tate, J. *Sci. Rep.* **2017**, *7*, 1–11.
15. Carp, O.; Huisman, C. L.; Reller, A. *Prog. Solid State Chem.* **2004**, *32*, 33–177.
16. Cromer, D. T.; Herrington, K. J. *Am. Chem. Soc.* **1955**, *77*, 4708–4709.
17. Baur, V. W. H. *Acta Cryst.* **1961**, *14*, 214–216.



18. Latroche, M.; Brohan, L.; Marchand, R.; Tournoux, M. *J. Solid State Chem.* **1989**, *81*, 78–82.
19. Hu, W.; Li, L.; Li, G.; Liu, Y.; Withers, R. L. *Sci. Rep.* **2014**, *4*, 1–9.
20. Paola, A. D.; Ballardita, M.; Palmisano, L. *Catalysts* **2013**, *3*, 36–73.
21. Li, H.; Guo, Y.; Robertson, J. J. *Phys. Chem. C* **2015**, *119*, 18160–18166.
22. Zhang, J.; Zhou, P.; Liu, J.; Yu, J. J. *Phys. Chem. Chem. Phys.* **2014**, *16*, 20382–20386.
23. Luttrell, T.; Halpegamage, S.; Tao, J.; Kramer, A.; Sutter, E.; Batzil, M. *Sci. Rep.* **2014**, *4*, 1–8.
24. Kar, P.; Zheng, S.; Zhang, Y.; Vahidzadeh, E. *Appl. Catal. B.* **2019**, *243*, 522–536.
25. Park, S.; Baek, S.; Kim, D.; Lee, S. *Mater. Lett.* **2018**, *232*, 146–149.
26. Roy, N.; Park, Y.; Sohn, Y.; Pradhan, D. *Semicond. Sci. Technol.* **2015**, *30*, 1–8.
27. Arienzo, M. D.; Carbajo, J.; Bahamonde, A.; Crippa, M.; Polizzi, S.; Scotti, R.; Wahba, L.; Morazzoni, F. J. *Am. Chem. Soc.* **2011**, *133*, 17652–17661.
28. Yu, J.; Low, J.; Xiao, W.; Zhou, P.; Jaroniec, M. J. *Am. Chem. Soc.* **2014**, *136*, 8839–8842.
29. Tong, H.; Zhou, Y.; Zhang, G.; Li, P.; Zhu, R.; He, Y. *Appl. Surf. Sci.* **2018**, *444*, 267–275.
30. Li, X.; Dong, G.; Li, S.; Lu, G.; Bi, Y. *J. Am. Soc.* **2016**, *138*, 2917–2920.
31. Zhang, Y.; Wang, X.; Dong, P.; Huang, Z.; Nie, X.; Zhang, X. *Green Chem.* **2018**, *9*, 2084–2090.
32. Huygh, S.; Bogaerts, A.; Neyts, E. C. *J. Phys. Chem. C* **2016**, *120*, 21659–21669.
33. Ji, Y.; Luo, Y. *J. Am. Chem. Soc.* **2016**, *138*, 15896–15902.
34. Lee, J.; Sorescu, D. C.; Deng, X. *J. Am. Chem. Soc.* **2011**, *133*, 10066–10069.
35. Petrik, N. G.; Kimmel, G. A. *J. Phys. Chem. C* **2015**, *119*, 23059–23067.
36. Ou, G.; Xu, Y.; Wen, B.; Lin, R.; Ge, B.; Tang, Y.; Liang, Y.; Yang, C.; Huang, K.; Zu, D.; Yu, R.; Chen, W.; Li, J.; Wu, H.; Liu, L.; Li, Y. *Nature Comm.* **2018**, *9*, 1–9.
37. Pan, X.; Yang, M.; Fu, X.; Zhang, N.; Xu, Y. *Nanoscale* **2013**, *5*, 3601–3614.
38. Naldoni, A.; Altomare, M.; Zoppellaro, G.; Liu, N.; Kment, S.; Zbroil, R.; Schmuki, P. *ACS Catal.* **2019**, *9*, 345–364.
39. Xu, Y.; Wu, S.; Wan, P.; Sun, J.; Hood, Z. D. *RSC Adv.* **2017**, *7*, 32461–32467.
40. Nowotny, J. *Oxide Semiconductors for Solar Energy Conversion: Titanium Dioxide*; CRC Press: UK, 2017.
41. Liu, L.; Jiang, Y.; Zhao, H.; Chen, J.; Cheng, J.; Yang, K.; Li, Y. *ACS Catal.* **2016**, *6*, 1097–1108.
42. Kofstad, P.; Nonstoichiometry, P. *Diffusion, and Electrical Conductivity in Binary Metal Oxides*; Wiley-Interscience: New York, 1972.
43. Padhila, A. C. M.; Raebiger, H.; Rocha, A. R.; Dalpian, G. M. *Sci. Rep.* **2016**, *6*, 1–7.
44. Li, J.; Lazzari, R.; Chenot, S.; Jupille, J. *Phys. Rev. B* **2018**, *97*.
45. Xiong, L.; Li, J.; Yang, B.; Yu, Y. *J. Nanopart.* **2012**, *1*–13.
46. Bak, T.; Chu, D.; Francis, A. R.; Li, W.; Nowotny, J. *Catal. Today* **2014**, *224*, 200–208.
47. Nowotny, J.; Alim, M. A.; Bak, T.; Idris, M. A.; Ionescu, M.; Prince, K.; Sahdan, M. Z.; Sopian, K.; Teridi, M. A. M.; Sigmund, W. *Chem. Soc. Rev.* **2015**, *44*, 8424–8442.
48. Strunk, J.; Vining, W. C.; Bell, A. T. *J. Phys. Chem. C* **2010**, *114*, 16937–16945.
49. Voepel, P.; Weiss, M.; Smarsly, B. M.; Marschall, R. *J. Photochem. Photobiol. A* **2018**, *366*, 34–40.
50. Setvin, M.; Wagner, M.; Schmid, M.; Parkinson, G. S.; Diebold, U. *Chem. Soc. Rev.* **2017**, *46*, 1772–1784.
51. Yang, L.; Wu, T.; Zhang, R.; Zhou, H.; Xia, L.; Shi, X.; Zheng, H.; Zhang, Y.; Sun, X. *Nanoscale* **2019**, *11*, 1555–1562.
52. Saravanan, R.; Manoj, D.; Qin, J.; Naushad, M. *Process Saf. Environ. Prot.* **2018**, *120*, 339–347.

53. Xing, M.; Zhou, Y.; Dong, C.; Cai, L.; Zheng, L.; Shen, B.; Pan, L.; Dong, C.; Chai, Y.; Zhang, J.; Yin, Y. *Nano Lett.* **2018**, *18*, 3384–3390.
54. Liu, B.; Cheng, K.; Nie, S.; Zhao, X.; Yu, H.; Yu, J.; Fujishima, A.; Nakata, K. *J. Phys. Chem. C* **2017**, *121*, 19836–19848.
55. Arif, A. F.; Balgis, R.; Ogi, T.; Iskander, F.; Kinoshita, A.; Nakamura, K.; Okuvama, K. *Sci. Rep.* **2017**, *7*, 1–9.
56. Wallace, S. K.; McKenna, K. P. *Adv. Mater. Interfaces* **2014**, *1*, 1–5.
57. Baykara, M. Z.; Monig, H.; Schwendemann, T. C.; Unverdi, O.; Altman, E. I.; Schwarz, U. D. *Appl. Phys. Lett.* **2016**, 108.
58. Mezheny, S.; Maksymovych, P.; Thompson, T. L.; Diwald, O.; Stahl, D.; Walck, S. D. *Chem. Phys. Lett.* **2003**, *369*, 152–158.
59. Yang, S.; Tang, W.; Ishikawa, Y.; Feng, Q. *Mater. Res. Bull.* **2011**, *46*, 531–537.
60. Naldoni, A.; Allieta, M.; Santangelo, S.; Marelli, M.; Fabbri, F.; Cappelli, S.; Bianchi, C. L.; Psaro, R.; Santo, V. D. *J. Am. Chem. Soc.* **2012**, *134*, 7600–7603.
61. Zhu, G.; Lin, T.; Lu, X.; Zhao, W.; Yang, C.; Wang, Z.; Yin, H.; Liu, Z.; Huang, F.; Lin, J. *J. Mater. Chem.* **2013**, *1*, 9650–9653.
62. Berkó, A.; Biró, T.; Kecskés, T.; Solymosi, F. *Vacuum* **2001**, *61*, 317.
63. Payne, D. T.; Zhang, Y.; Pang, C. L.; Fielding, H. H.; Thornton, G. *Top. Catal.* **2017**, *60*, 392–400.
64. Kong, M.; Li, Y.; Chen, X.; Tian, T.; Fang, P.; Zheng, F.; Zhao, X. *J. Am. Chem. Soc.* **2011**, *133*, 16414–16417.
65. Liu, H.; Yang, W.; Ma, Y.; Cao, Y.; Yao, J. *New J. Chem.* **2002**, *26*, 975–977.
66. Pan, H.; Gu, B.; Zhang, Z. *J. Chem. Theory Comput.* **2009**, *5*, 3074–3078.
67. Wendt, S.; Sprunger, P. T.; Lira, E.; Madsen, G. K. H.; Li, Z.; Hasen, J.; Matthiesen, J. *Science* **2008**, *320*, 1755–1759.
68. Schneider, J.; Nikitin, K.; Dillert, R.; Bahnemann, D. W. *Faraday Discuss.* **2017**, *197*, 505–516.
69. Wu, X.; Huang, Z.; Liu, Y.; Fang, M. *Int. J. Photoenergy* **2011**, 1–7.
70. Bremond, E.; Ciofini, I.; Carlos, J.; Adamo, C. *Acc. Chem. Res.* **2016**, *49*, 1503–1513.
71. Sekiye, T.; Kurita, S. *Nano Micromater.* **2008**, 121–141.
72. Stetsovych, O.; Todorovic, M.; Shimizu, T. K.; Moreno, C.; Ryan, J. W.; Leon, C. P.; Sagisaka, K.; Palomares, E.; Matolin, V.; Fujita, D.; Perez, R.; Custance, O. *Nature Comm.* **2015**, *6*, 1–9.
73. Martinez, U.; Vilhelmsen, L. B.; Kirstoffersen, H. H. *Phys. Rev. B. Cond. Matt.* **2011**, *84*, 205434.
74. Wen, H. F.; Miyazaki, M.; Zhang, Q.; Adachi, Y.; Li, Y. J.; Sugawara, Y. *Phys. Chem. Chem. Phys.* **2018**, *20*, 28331–28337.
75. Jiang, X.; Zhang, Y.; Jiang, J.; Rong, Y.; Wang, Y.; Wu, Y.; Pan, C. *J. Phys. Chem. C.* **2012**, *116*, 22619–22624.
76. Chen, Y.; Fong, D. D.; Herbert, F. W.; Rault, H.; Rueff, J.; Tsvetkov, N.; Yildiz, B. *Chem Mater.* **2018**, *30*, 3359–3371.
77. Selli, D.; Fazio, G.; Valentin, C. D. *Catalysts* **2017**, *7*, 357.
78. Ha, M. A.; Alexandrova, A. N. *J. Chem. Theory Comput.* **2016**, 2889–2895.
79. Boonchun, A.; Reunchan, P.; Umezawa, N. *Phys. Chem. Chem. Phys.* **2016**, *18*, 30040–30046.
80. Araujo-Lopez, E.; Varilla, L. A.; Seriani, N.; Montoya, J. A. *Surf. Sci.* **2016**, *653*, 187–196.
81. Cheng, H.; Selloni, A. *Phys. Rev. B* **2009**, *79*, 092101–092104.
82. Portillo-Vélez, N. S.; Olvera-Neria, O.; Hernández-Pérez, I.; Rubio-Ponce, A. *Surf. Sci.* **2013**, *616*, 115–119.
83. Murugesan; et al. *J. Phys. Chem. C* **2010**, *114*, 10598–10605.
84. Li, W. K.; Chu, L. N.; Gong, X. Q.; Lu, G. *Surf. Sci.* **2011**, *605*, 1369–1380.

85. Mete, E.; Gulseren, O.; Ellialtioglu, S. *Eur. Phys. J. B* **2012**, 85, 204–211.
86. Lamiel-Garcia, O.; Tosoni, S.; Illas, F. *J. Phys. Chem. C* **2014**, 118, 13667–13673.
87. Atanelov, J.; Gruber, C.; Mohn, P. *Comput. Mater. Sci.* **2015**, 98, 42–50.
88. Panta, R.; Ruangpornvisuti, V. *Int. J. Hydrogen Energy* **2019**, 44, 32101–32111.
89. Zhang, W.; Xiao, X.; Zeng, X.; Li, Y.; Zheng, L.; Wan, C. *J. Alloys Compd.* **2016**, 685, 774–783.
90. Sharma, P. K.; Cortes, M. A. L. R. M.; Hamilton, J. W. J.; Han, Y. *Catal. Today* **2019**, 321–322, 9–17.
91. Jiang, Z.; Wan, W.; Wei, W.; Chen, K.; Li, H.; Wng, P. K.; Xie, J. *Appl. Catal B* **2017**, 204, 283–295.
92. Wang, X.; Rui, Z.; Zeng, Y.; Ji, H.; Du, Z.; Rao, Q. *Catal. Today* **2017**, 297, 151–158.
93. Zeng, Q.; Chen, W.; Zhang, Y.; Dai, W.; Guo, X. *J. Nat. Gas. Chem.* **2010**, 19, 300–306.
94. Kobayashi, H.; Higashimoto, S. *Appl. Catal. B Environ.* **2015**, 170–171, 135–143.
95. Tang, M.; Zhang, Z.; Ge, Q. *Catal. Today* **2016**, 274, 103–108.
96. Panta, R.; Ruangpornvisuti, V. *Int. J. Hydrog. Energy* **2017**, 42, 19106–19113.
97. Chizallet, C.; Digne, M.; Arrouvel, C.; Raybaud, P.; Delbecq, F.; Costentin, G.; Che, M.; Sautet, P.; Toulhoat, H. *Top. Catal.* **2009**, 52, 1005–1016.
98. Tumuluri, U.; Howe, J. D.; Mounfield, W. P.; Li, M.; Chi, M.; Hood, Z. D.; Walton, K. S.; Sholl, D. S.; Dai, S.; Wu, Z. *ACS Sust. Chem. Eng.* **2017**, 5, 9295–9306.
99. Zhong, J. B.; Li, J. Z.; Feng, F. M.; Huang, S. T.; Zeng, J. *Mater. Lett.* **2013**, 100, 195.
100. Oseghe, E. O.; Maddila, S.; Ndungu, P. G.; Jannalagadda, S. B. *Appl. Catal. B Environ.* **2015**, 176–177, 288–297.
101. Wang, T.; Li, W.; Xu, D.; Wu, X.; Cao, L.; Meng, J. *Appl. Surf. Sci.* **2017**, 426, 325–332.
102. Han, L.; Su, B.; Liu, G.; Ma, Z.; An, X. *Mol. Catal.* **2018**, 456, 96.
103. Jedsukontorn, T.; Ueno, T.; Saito, N.; Hunsom, M. *J. Alloys Compd.* **2018**, 757, 188.
104. Xin, X.; Xu, T.; Yin, J.; Wang, L.; Wang, C. *Appl. Catal. B Environ* **2015**, 176–177, 354.
105. Zhou, W.; Li, W.; Want, J. Q.; Qu, Y.; Yang, U.; Xie, Y.; Zhang, K.; Wang, L.; Fu, H.; Zhao, D. *J. Am. Chem. Soc.* **2014**, 136, 9280.
106. Saputera, W. H.; Mul, G.; Hamdy, M. S. *Catal. Today* **2015**, 246, 60.
107. Hamdy, M. S.; Berg, O.; Mul, G. *J. Mol. Struct.* **2020**, 1200, 127113.
108. Rengifo-Herrera, J. A.; Pierzchala, K.; Sienkiewicz, A.; Forro, L.; Kiki, J.; Moser, J. E.; Pulgarin, C. *J. Phys. Chem. C* **2010**, 114, 2717.
109. Chen, X.; Lou, Y.; Samia, A. C.; Burda, C.; Gole, J. L. *Adv. Funct. Mater.* **2005**, 15, 41.
110. Wang, J.; Zhang, P.; Zhu, J.; Li, H. *Appl. Catal. B Environ.* **2013**, 134–135, 198.
111. Lakhera, S. K.; Neppolian, B. *Int. J. Hydrog. Energy* **2020**, 45, 7627.
112. Sugha, N.; Mahalakshmi, M.; Monika, S.; Neppolian, B. *Int. J. Hydrog. Energy* **2020**, 45, 7552.
113. Hitam, C. N. C.; Jalil, A. A.; Triwahyono, S.; Ahmad, A.; Jaafar, N. F.; Salamun, N.; Fatah, N. A. A.; Teh, L. P.; Khusnum, N. F.; Ghazali, Z. *RSC Adv.* **2016**, 6, 76259.
114. Liu, L.; Gao, F.; Zhao, H.; Li, Y. *Appl. Catal. B Environ.* **2013**, 134–135, 349.
115. Raguram, T.; Rajni, K. S. *Appl. Phys. A: Mater. Sci. Process.* **2019**, 125, 288.
116. Huang, K. C.; Chien, S. H. *Appl. Catal. B Environ.* **2013**, 140–141, 283.
117. Chang, S.; Lee, C. *Appl. Catal. B Environ.* **2013**, 132–133, 219.
118. Chen, Y.; Li, W.; Wang, J.; Gan, Y.; Liu, L.; Ju, M. *Appl. Catal. B Environ.* **2016**, 191, 94.
119. Vittadini, A.; Casarin, M.; Selloni, A. *J. Phys. Chem. C.* **2009**, 113, 18973–18977.
120. Yang, D.; Liu, H.; Zheng, Z.; Yuan, Y.; Zhao, J.; Waclawik, E. R.; Ke, X.; Zhu, H. *J. Am. Chem. Soc.* **2009**, 131, 17885–17893.

121. Li, W.; Liu, C.; Zhou, Y.; Bai, Y.; Feng, X.; Yang, Z.; Lu, L.; Lu, X.; Chan, K. *J. Phys. Chem. C* **2008**, *112*, 20539–20545.
122. Liu, B.; Khare, A.; Aydil, E. S. *ACS Appl. Mater. Interfaces* **2011**, *3*, 4444–4450.
123. Wang, Z.; Wang, Y.; Zhang, W.; Wang, Z.; Ma, Y.; Zhou, X. *J. Phys. Chem. C* **2019**, *123*, 1779–17789.
124. Zha, R.; Nadimicherla, R.; Guo, X. *J. Mater. Chem. A* **2015**, *12*, 6565–6574.
125. Divya, K. S.; Xavier, M. M.; Vandana, P. V.; Reethu, V. N.; Mathew, S. *New J. Chem.* **2017**, *41*, 6445–6454.
126. Prasannalakshmi, P.; Shanmugam, N. *Mater. Sci. Semicond. Process.* **2017**, *61*, 114–124.
127. Wu, K.; Dong, X.; Zhu, J.; Wu, P.; Liu, C.; Wang, Y.; Wu, J.; Hou, J.; Liu, Z. *J. Mater. Sci.* **2018**, *53*, 11595–11606.
128. Xi, G.; Ouyang, S.; Ye, J. *Chem. Pub. Soc.* **2011**, *17*, 9057–9061.
129. Mazabuel-Collazos, A.; Gomez, C. D.; Paez, J. E. R. *Mater. Chem. Phys.* **2019**, *222*, 230–245.
130. Chen, S.; Zhao, W.; Liu, W.; Zhang, S. *App. Surf. Sci.* **2008**, *255*, 2478–2484.
131. Deng, W.; Pan, F.; Batchelor, B.; Jung, B.; Zhang, P.; Abdel-Wahab, A.; Zhou, H.; Li, Y. *Environ. Sci. Water Res.* **2019**, *5*, 769–781.
132. Wang, X.; Yang, W.; Li, F.; Zhao, J.; Liu, R.; Liu, S.; Li, B. *J. Hazard Mater.* **2015**, *292*, 126–136.
133. Li, H.; Xiao, R.; Li, Z.; Zhan, Y.; Bian, H.; Nie, B.; Chen, Z.; Lu, J. *Energy Technol.* **2014**, *2*, 526–530.
134. Liu, L.; Zhao, C.; Zhao, H.; Pitts, D.; Li, Y. *Chem. Commun.* **2013**, *49*, 3664–3666.
135. Lopez, T.; Hernandez, J.; Gomez, R. *Langmuir* **1999**, *15*, 5689–5693.
136. Izumi, Y. *Coord. Chem. Rev.* **2013**, *257*, 171–186.
137. Zhao, H.; Pan, F.; Li, Y. *J. Materiomics* **2017**, *3*, 17–32.
138. Xiong, Z.; Li, Y.; Dong, L.; Zhao, Y.; Zhang, J. *J. Photochem. Photobiol. C* **2018**, *36*, 24–47.
139. Yang, M. Q.; Xu, Y. *J. Nanoscale Horiz.* **2016**, *1*, 185–200.
140. Liu, L.; Zhao, H.; Li, Y. *J. Phys. Chem. C* **2012**, *116*, 7904.
141. Li, R.; Li, R. *Adv. Catal.* **2017**, *60*, 1–57.
142. Lin, L. Y.; Kavadiya, S.; He, X.; Wang, W. N.; Karakocak, B. B.; Lin, Y. C.; Berezin, M.; Biswas, P. *Chem. Eng. J.* **2020**, *389*, 123450.
143. Tasbihi, M.; Fresno, F.; Simon, U.; Villar-Garcia, I. J.; Perez-Dieste, V.; Escudero, C.; O'Shea, V. L. P. *Appl. Catal. B Environ.* **2018**, *68*.
144. Olivo, A.; Trevisan, V.; Ghedini, E.; Pinna, F.; Bianchi, C. L.; Naldoni, A.; Cruciani, G. *J. CO<sub>2</sub> Util.* **2015**, *12*, 86.
145. Zhao, H.; Xu, J.; Liu, L.; Rao, G.; Zhao, C.; Li, Y. *J. CO<sub>2</sub> Util.* **2016**, *15*, 15.
146. Ahmed, N.; Shibata, Y.; Taniguchi, T.; Izumi, Y. *J. Catal.* **2011**, *279*, 123.
147. Yong, Z.; Rodriguez, A. E. *Energy Convers.* **2002**, *43*, 1865.
148. Yong, Z.; Mata, V.; Rodriguez, A. E. *Ind. Eng. Chem. Res.* **2001**, *40*, 204.
149. Ram, M. K.; Xu, Z. P.; Lu, G. Q.; Diniz, J. C. *Ind. Eng. Chem. Res.* **2006**, *45*, 7504.
150. Liu, L.; Zhao, C.; Xu, J.; Li, Y. *Appl. Catal. B* **2015**, *179*, 489–499.
151. Tahir, M.; Amin, N. A. S. *Chem. Eng. J.* **2016**, *285*, 635.
152. Kim, K.; Razaq; Socar, S.; Park, Y.; Grimes, C. A. *RSC Adv.* **2016**, *6*, 38964–38971.
153. Zhao, Y.; Wei, Y.; Wu, X.; Zheng, H.; Zhao, Z.; Liu, J.; Li, J. *Appl. Catal. B Environ.* **2018**, *226*, 360.
154. Piler, K.; Watters, J.; Benson, T. J. *Mater. Lett.* **2020**, *278*, 128410–128413.
155. Ye, L.; Zan, L.; Tian, L.; Peng, T.; Zhang, J. *Chem Commun.* **2011**, *47*, 6951–6953.
156. Wu, S.; Xiong, J.; Sun, J.; Hood, Z. D.; Zeng, W.; Yang, Z.; Gu, L.; Zhang, X.; Yang, S. *ACCS Appl. Mater. Interfaces* **2017**, *9*, 16620–16626.
157. Che, M.; Tench, A. J. *Adv. Catal.* **1982**, *31*, 77–133.
158. Che, M.; Tench, A. J. *Adv. Catal.* **1983**, *32*, 1–148.

159. Yim, C. M.; Pang, C. L. *Phys. Rev. Lett.* **2010**, *104*, 036806.
160. Komaguchi, K.; Maruoka, T.; Nakano, H.; Imae, I.; Ooyama, Y.; Harima, Y. *J. Phys. Chem. C* **2010**, *114*, 1240–1245.
161. Li, X.; Yu, J.; Jaroniec, M.; Chen, X. *Chem. Rev.* **2019**, *119*, 3962–4179.
162. Agbroko, O. W.; Piler, K.; Benson, T. J. *Chem. Bio. Energy Rev.* **2017**, *6*, 339–359.
163. Doan, L.; Benson, T. J. *J. Chem. Eng. Data* **2020**, *65*, 2325–2331.
164. Wang, X. X.; Ma, X. L.; Zhao, S.; Song, C. S. *Energy Environ. Sci.* **2009**, *2*, 878–882.
165. Ma, X. L.; Wang, X. X.; Song, C. S. *JACS* **2009**, *131*, 5777–5783.

## About the authors



**Tracy J. Benson** received his Ph.D. in Chemical Engineering from Mississippi State University in the area of catalytic conversions of lipid feedstocks to green fuels. In 2009, he joined Lamar University as an assistant professor, where he currently holds the rank of associate professor as well as the Associate Director of Research for the Center for Midstream Management and Science. He is also the recipient of the Dr. Jack Gill Faculty Research Fellowship. His research interests include Carbon Capture Utilization and Storage (CCUS) technologies, including the photocatalytic conversion of waste carbon dioxide to useful fuels and chemicals. His research interests also include the minimization of industrial wastes, including unwanted byproducts and wasted energies, by developing alternate chemical transformation pathways using novel catalysts combined with process development.



**Karishma Piler** obtained her B.Sc. in Chemical Engineering from Vellore Institute of Technology, Vellore in India and received her M.Sc. in Chemical Engineering from The University of Manchester, UK. She received her Ph.D. degree in Chemical Engineering from Lamar University, Beaumont, Texas, USA, in 2019 under the supervision of Prof. Tracy Benson. Her primary research interests include photocatalysis and waste carbon utilization. Her work has been on synthesizing novel catalysts based on titanium dioxide and its nanocomposites with



and without surfactants in heterogeneous catalytic applications, principally for efficient and economic photocatalytic conversion of carbon dioxide to useful products through band gap manipulations.



**Cristian Bahrim** has received his B.Sc./M. Sc. degrees from University of Bucharest in 1991, and Ph.D. degree from University of Paris-Orsay in 1997, under the supervision of Prof. Francoise Masnou-Seeuws. Between 1998 and 2001, he was postdoc at Kansas State University, in the Theoretical Atomic Physics Group. He joined the Department of Chemistry and Physics at Lamar University in 2001. Beginning with March 2005, he holds a joint-appointment with the Phillip M. Drayer Department of Electrical Engineering. In fall 2013, he was Interim Chair of the newly created Department of Physics. In 2015 he became full professor. In 2018–2019 he was the President of the Texas Section of the American Association of Physics Teachers (AAPT), after several years of holding various officer positions in this organization. He is an active member of the American Association of Physics (APS) and mentor of the Society of Physics Students (SPS) at Lamar University, for which he was selected finalist in 2019, for the best SPS Mentor of the Year award.

As teacher at Lamar, he led graduate and undergraduate students to outstanding academic success, including several Beck fellows, Goldwater, and McNair scholars, for which he received the 2015 Faculty Mentor Award. Also, he received the 2019 Faculty Mentor Award in Physics & Astronomy from The National C.U.R. (Council of Undergraduate Research), in Washington DC. He chaired and organized various regional, national, and international conferences including the 2016 and 2020 Spring Meetings of the Texas Sections of APS, AAPT and SPS Zone 13 hosted at Lamar University. He was for 2 years (2017 and 2018) visiting professor at Shanghai International Studies University. He is now the Active Director of the Office of Undergraduate Research.

His research interest is in the areas of atomic physics, quantum mechanics, optics, lasers, and light–matter interaction. He published more than 100 peer-reviewed articles, book chapters, and conference proceedings papers.





**Sylvestre Twagirayezu** received his B.S. from La Roche University in 2004, his M.S. in Chemistry from Case Western Reserve University in 2006, and his Ph.D. in Physical Chemistry from the University of Akron in 2011. Prior to Lamar University, he was a visiting Assistant Professor at the University of Akron (2011–2012), Postdoctoral Research Fellow at Canadian Light source Inc. Far-infrared Beamline (2012–2014), and Research Associate at Brookhaven National Laboratory (2014–2016). He serves as Secretary-treasurer

for Sabine-Neches Local American Chemical Society (ACS) Chapter, and Site Coordinator for the ACS Project SEED Program. His research program mainly focuses on the vibrational dynamics and molecular spectroscopy of badly-behaved molecules, and the development of highly sensitive techniques for remote sensing, environmental protection, and petroleum processing applications.